

With compliments!

June '91

Atle Nordgaard

Performance Prediction of Solar Thermal Systems
and the Use of Monolithic Silica Aerogel
to Improve Collector Efficiency

Atle Nordgaard

March 1991

Doktor Ingeniøravhandling
Institutt for Varme- Ventilasjons- og Sanitertechnik
Norges Tekniske Høgskole

Preface

The work presented here is part of the fulfillment of the Doktor Ingeniør degree at the Norwegian Institute of Technology (NTH), which was carried out during the period from December 1987 to June 1991 at the Division of Heating and Ventilating at NTH and SINTEF Applied Thermodynamics.

I would like to thank my advisor, Professor Eystein Rødahl for his valuable advice and assistance throughout this work.

Other members of the scientific staff at the Division and Terje Jacobsen in particular, have given invaluable support. Thanks also goes to the Solar Energy Laboratory (SEL), University of Wisconsin-Madison, USA, and Professor William A. Beckman and Professor John A. Duffie in particular for giving me the opportunity of staying one year as a visiting scholar at SEL.

I am also indebted to the Royal Norwegian Council for Scientific and Industrial Research for the scholarships which enabled this thesis and my stay at SEL to become a reality.

Special thanks goes to Frijof Salvesen.

Thanks Mom and Dad for your support, guidance, and encouragement in all of my work.

To my wife Aud Wenche, in appreciation for the patience, understanding, and love you have given me.

Abstract

This thesis is devoted to a study of active solar thermal systems, and focuses on analysis and design tools. The main part of this work is concerned with development of algorithms for modeling flat-plate collectors that use monolithic silica aerogel (MSA) as part of the cover glazing. This study of MSA collectors also includes evaluation of the performance of the collector component, and simulation studies of solar systems with and without the use of MSA collectors. The other parts of the thesis involves evaluation of analysis and design tools concerning the solar performance prediction. Accuracy and ease-of-use has been assessed.

MSA is an absorbing and scattering material in the solar part of the spectrum (0.3 - 3.0 μm). It is shown that isotropic scattering may be assumed, as long as the cover thickness is less than 50 mm. Analysis of scattering is usually mathematically very complex and requires a great deal of computational effort. However, a relatively fast and simple method for isotropic scattering within an absorbing and scattering medium has been proposed (\hat{F} -method).

A new method, which allows the inclusion of scattering layers, based on the embedding technique [Edwards (1977)], was developed and used to calculate the transmittance-absorptance product. All of the solar radiation that is absorbed by a cover system is not lost, since this absorbed energy tends to increase the cover temperatures and consequently reduce the losses from the absorber plate. In order to maintain the simplicity of the Hottel-Whillier collector equation, an effective transmittance-absorptance product was evaluated. The procedure described by Duffie and Beckman (1980) was applied for this purpose.

The incidence angle modifier approach used in conventional flat-plate collectors was found to be valid for MSA collectors. Furthermore, effective incidence angles of isotropic diffuse solar radiation have been evaluated.

MSA has a very low thermal conductivity (0.008 W/m²K evacuated to 0.1 bar). However, the material is partially transparent in the infrared between 3 and 5 μm . Due to large spectral variations in this region, the radiative transport will not be a local phenomenon anymore, and direct radiative communication between the boundaries may occur. Consequently, the radiative transport strongly varies with MSA thickness and the emissivities of the boundaries. In this case, the coupling between the radiation field and the heat flux caused by conduction has to be considered. To obtain an exact solution for the combined conduction-radiation energy transfer in an absorbing-emitting (and scattering medium), the general energy equation must be solved. The \hat{F} -concept was modified to be applicable for the infrared heat transfer. The temperature distribution within the collector was found by expressing the conduction terms by finite-differences, and solving the simultaneous nonlinear equations by Newton-Raphson. The inclusion of property variations (MSA has the characteristic of a non-gray medium) did add some complexity to the functional form of the equations. The total exchange factors had to be solved on a monochromatic basis, and the integrals within the radiation terms had to be evaluated in each iteration. Once the temperature distribution is known, the heat transfer across the collector from the absorber to the surroundings can be easily calculated by means of an energy balance on one of the boundary surfaces.

The difference in predicted instantaneous collector efficiency for three different collector designs was observed: (1) one cover with selective absorber plate; (2) evacuated flat-plate collector; (3) MSA collector. It was clearly seen that considerable improvements of the efficiency could be obtained by using MSA collectors for medium and high temperature applications.

The results of a simulation study of a solar heating system and a combined solar heating and cooling system are presented. In particular, the predicted performance obtained using conventional solar collectors is compared with the predicted performance using MSA collectors.

Topics on the performance prediction of solar thermal collectors are discussed. Storage tank stratification is found to have only a small effect on the collector performance, but significantly increases the solar system performance. Simulated system performance with TRNSYS [Klein et al. (1988)] is compared with the performance predicted by design methods, and recommendations are given.

Furthermore, hourly solar radiation models were evaluated. On an overall basis, the isotropic sky model showed the poorest performance and is not recommended for estimating the hourly radiation on a tilted surface. Any of the anisotropic models should yield acceptable performance for estimating radiation on a tilted surface. The tilted surface models showed little sensitivity to the input of horizontal diffuse radiation.

Table of Contents

PREFACE	
ABSTRACT	
TABLE OF CONTENTS	
1 INTRODUCTION	1
2 A REVIEW OF SOLAR THERMAL SYSTEMS	2
2.1 Active Solar Thermal Systems	3
2.2 Solar System Analysis	4
2.2.1 Solar Collector Model	6
2.2.2 Storage Tank Modelling	10
2.2.3 Thermal Design Methods	11
2.2.4 Simulation Methods	17
2.3 Solar Radiation	18
2.3.1 Determination of Horizontal Diffuse Radiation	19
2.3.2 Total Radiation on Tilted Surfaces	24
2.4 Transparent Insulation Materials	31
2.4.1 Introduction	31
2.4.2 Classification of Transparent Insulation Materials	32
2.4.3 Available Materials and Real Cover Systems	33
3 SOLAR SYSTEM PERFORMANCE PREDICTION	37
3.1 Introduction	37
3.2 Solar System Performance Equations	38
3.2.1 Model Development	38
3.2.2 Numerical Solution of the System Performance Equation	42
3.2.3 Convergence and Accuracy of the Simulation Method	44

3.3	Transient Solar Collector Response and its Effects on the Long-Term Average Performance	48
3.4	Hourly versus Instantaneous Radiation Values and the Effects on the Long-Term Average Performance	52
3.5	Thermal Design Methods versus Detailed Simulations	56
3.6	Storage Tank Stratification	60
4 SOLAR RADIATION MODELS		
4.1	Introduction	64
4.2	Determination of Global Horizontal Radiation	65
4.2.1	Global Horizontal Radiation Models	66
4.2.2	Model Performance	67
4.3	Horizontal Diffuse Radiation	69
4.3.1	Model Performance	69
4.4	Sky Diffuse Radiation	70
4.4.1	Model Performance	71
4.5	Closing Remarks	76
5 MODELLING OF FLAT-PLATE COLLECTORS BASED ON MONOLITHIC SILICA AEROGEL (MSA)		
5.1	Introduction	78
5.2	Attenuation of Solar Radiation in MSA	79
5.2.1	Optical Transmission Studies in MSA	80
5.2.2	Radiative Transfer in an Absorbing-Scattering Medium	85
5.2.3	Spectral Dependence of Transmittance	90
5.2.4	Transmittance for Diffuse Radiation	95
5.3	Infrared Heat Transfer in MSA	98
5.3.1	Infrared Properties of MSA	98
5.3.2	Combined Conduction and Radiation in an Absorbing-Emitting and Scattering Medium by the \bar{F} -Technique	102
5.3.3	Combined Conduction and Radiation in an Absorbing-Emitting and Scattering Medium by the \bar{F} -Technique	111
5.4	Transmittance-Absorptance Product for MSA Collectors	112
5.4.1	A New Method for Calculating the Solar Absorption by Each Element in an Absorber-Coverglass Array	118
5.4.2	Incidence Angle Modifier for MSA Collectors	120
5.5	Useful Energy Gain from MSA Collectors	120
5.5.1	Collector Overall Heat Loss Coefficient	128
5.5.2	Collector Heat Removal Factor and Mean Plate Temperature	130
5.5.3	Effective Transmittance-Absorptance Product	130
5.5.4	MSA Collector Performance	132

5.6	Comparison with Other Collector Designs	133
5.6.1	Collector Efficiencies	133
5.6.2	Annual Performance	134

6 SYSTEM SIMULATION - CASE STUDIES		
6.1	Introduction	136
6.2	A Heating System Simulation Study	136
6.2.1	System Description	136
6.2.2	System Simulation	138
6.3	A Simulation Study of Solar Air Conditioning	142
6.3.1	System Description	143
6.3.2	System simulation	144

7 FUTURE RESEARCH SUGGESTIONS	148
--------------------------------------	-----

REFERENCES	150
-------------------	-----

NOMENCLATURE	158
---------------------	-----

APPENDIX A	162
-------------------	-----

CHAPTER 1

Introduction

Today, solar technologies remain promising alternatives for providing thermal energy for a variety of end-uses. The principle barrier to the wider use of solar heat technologies continues to be unfavorable economics in comparison to conventional technologies. However, current research efforts focusing on durable, reliable, and cost effective products (materials, components, and systems) hold the promise for substantially improving the competitive posture of solar heat technologies and make it an effective and viable resource. Transparent insulation materials (TIM) belong to the group of new materials and show enormous potential for significantly improving the performance of solar collectors and passive heating systems in buildings. At present honeycomb and aerogel materials are the two major types of TIMs that receive attention. Besides technology development the breakthrough for solar energy is dependent upon reliable methods (tools) to insure the optimal design and integration of solar energy systems in buildings.

This thesis is devoted to a study of active solar thermal systems, and focuses on analysis and design tools. The main part of this work is concerned with development of algorithms for modeling flat-plate collectors that use monolithic silica aerogel (MSA) as part of the cover glazing. This study of MSA collectors also includes evaluation of the performance of the collector component, and simulation studies of solar systems with and without the use of MSA collectors. The other parts of the thesis involves evaluation of analysis and design tools algorithms concerning the solar performance prediction. Accuracy and ease-of-use has been assessed.

CHAPTER 2

A Review of Solar Thermal Systems

The World Commission on Environment and Development (1987) states that the rapid increasing world population together with the limited amount of fossil fuels and the already significant environmental pollution (CO₂ greenhouse effect, acid rain, and ozone layer depletion) will give solar energy an increasing importance in the future. It is this background that makes the study of solar energy worthwhile.

Serious studies of the sun and its potential began in the seventeenth century, when Galileo and Lavoisier utilized the sun in their research. In the early twentieth century solar energy was used to power water distillation plants in Chile and irrigation pumps in Egypt. By the 1920s and 1930s practical use was being made of the sun's energy in California, USA for solar service-hot-water heaters. In the period from 1945 to 1965 solar developments also took place in countries outside the USA [Kreider et al. (1989)].

There are two main categories of solar thermal systems [ASHRAE Handbook (1987)]: active and passive. Passive systems are those systems which collect or use solar energy without direct recourse of any conventional energy source, such as electricity, to aid in the collection. Active systems require electric pumps or fans to collect solar energy. Furthermore, they can be classified by the means of their use, as domestic or industrial, and stand alone or solar supplemented. Finally, they may be divided by collector type into liquid or air systems, and by the type of storage as seasonal or daily systems.

2.1 Active Solar Thermal Systems

The two possible configurations of solar thermal systems with daily storage are classified as closed-loop or open-loop systems. A closed-loop system has been defined as a circuit in which the performance of the solar collector is directly dependent on the storage temperature. Figure 2.1.1 gives a schematic of a closed-loop system. These systems have been widely used to date and at present they are normally used when the temperature drop in the load is low, for example in space heating applications.

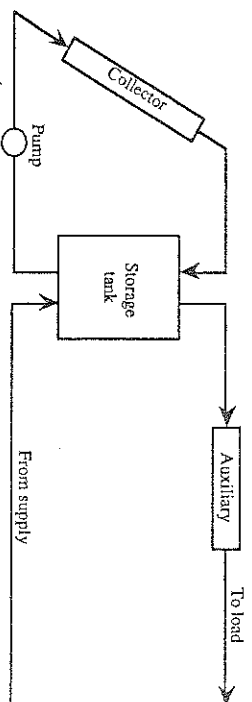


Figure 2.1.1 Schematic of a closed loop solar thermal system.

Figure 2.1.2 illustrates one of several possible configurations of open-loop systems in which the collector performance is independent of the storage temperature. Open-loop systems are normally used when the temperature drop in the load is high, for instance industrial process heat applications.

There are many applications of active solar thermal systems throughout the world. In this work the following applications will be considered:

- (1) Solar water and space heating
- (2) Solar air-conditioning

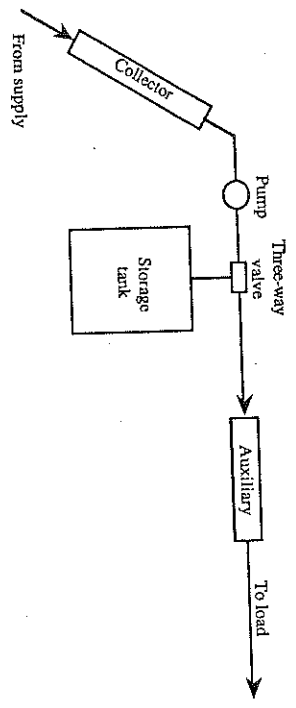


Figure 2.1.2 Schematic of an open-loop solar thermal system.

2.2 Solar System Analysis

The solar performance predictions can be divided into two parts, (1) the predictions of the input into the solar process, the solar radiation, and (2) the solution of equations governing the thermal system.

Figure 2.2.1 shows the solar radiation causing a solar process to produce an output. The solar process may be the response of a solar thermal system, the reaction of a photovoltaic cell or chemical reactions in a plant caused by solar radiation. Examples of output are electric power, heat or plant growth.



Figure 2.2.1 Schematic for the solar performance prediction.

The quality of the prediction of the output depends on how accurately both the solar radiation and the solar process are known. For a solar thermal system that generally consists of a solar collector, an energy storage and the load, the performance response is quite complex. However, the availability of micro-computers, greatly simplifies the problem of modeling the performance of a system when the components are coupled together, since in a computer simulation it is easy to keep track of all the changing variables involved.

The situation is very different for the solar radiation, which is subject to great uncertainty. A simulation will provide results for the period over which weather data are provided. Sufficient data (e.g., many years) must be provided in order for the simulation to give an estimate of the long-term average performance of the system. There are two problems with the use of simulations as a design tool. First, the hour-by-hour simulation of a system over many years involves significant computational effort. However, it is common to use a single design year ("Typical Meteorological Year") rather than years of long-term weather records as input to simulations. The accuracy of this approach depends on the non-linearity of the system, and how well the weather data for the design year matches the long-term average statistics. Secondly, hourly records of meteorological variables for extended periods of time do not exist for many locations

2.2.1 Solar Collector Model

Steady-State Collector Performance

Relevant studies of solar thermal collectors began by Hottel and Woertz (1942), Whillier (1953), and Hottel and Whillier (1958), who analyzed the performance of flat-plate collectors. The resulting theory of flat-plate collectors is well presented by Duffie and Beckman (1980) and allows the steady state performance of a standard flat-plate thermal collector to be expressed by

$$\dot{Q}_a = A_c Fr [S - U_L (T_i - T_a)]^n \quad (2.2.1)$$

where \dot{Q}_a = the actual useful collector energy gain [W]

A_c = the collector area [m²]

Fr = the collector heat removal factor

S = the absorbed solar radiation [$S = (\tau\alpha)I_r$] [W/m²]

$(\tau\alpha)$ = the transmittance-absorptance product

I_r = the hourly radiation on the collector surface [W/m²]

U_L = the collector overall heat loss coefficient [W/m²°C]

T_i = the fluid inlet temperature [°C]

T_a = the ambient air temperature [°C]

The + sign indicates a controller preventing the energy gain from the collector to be less than zero. The heat removal factor relates the actual useful collector energy gain to the useful energy gain if the whole absorber plate was at the fluid inlet temperature. Equation 2.2.1, also called the Hottel-Whillier collector equation shows that the useful collector gain is determined by the the difference between the absorbed solar radiation and the heat loss from the collector.

Solar hot water systems that are exposed to sub zero temperatures usually have a heat exchanger in the collector loop. Duffie and Beckman (1980) showed that the combination of collector and heat exchanger performs exactly like a collector with a reduced value of

Fr . Hence, the modified collector heat removal factor Fr' accounts for the presence of the heat exchanger and is given by

$$Fr' = \frac{Fr}{1 + \frac{A_c Fr U_L}{(\dot{m} C_{p,k})} \left[\frac{(\dot{m} C_{p,k})}{\epsilon (\dot{m} C_{p,min})} - 1 \right]} \quad (2.2.2)$$

where $(\dot{m} C_{p,k})$ is the fluid capacitance rate on the collector side of the heat exchanger, $(\dot{m} C_{p,min})$ is the smaller of the fluid capacitance rates on the two sides of the heat exchanger, and ϵ is the heat exchanger effectiveness.

Pipe heat losses on the collector side can be significant. Beckman (1978) elegantly incorporated the pipe heat loss in the collector performance factors U_L and $(\tau\alpha)$, where the collector and pipe system can be equivalently treated as a collector of reduced performance. The modified values of $(\tau\alpha)$ and U_L are defined as follows

$$(\tau\alpha)' = (\tau\alpha) \left[\frac{1}{1 + \frac{U_d A_o}{(\dot{m} C_{p,k})}} \right] \quad (2.2.3)$$

$$U_L' = U_L \left[\frac{1 - \frac{U_d A_i}{(\dot{m} C_{p,k})} + \frac{U_d (A_i + A_o)}{A_c Fr U_L}}{1 + \frac{U_d A_o}{(\dot{m} C_{p,k})}} \right] \quad (2.2.4)$$

where U_d is the loss coefficient from the duct and A_i and A_o are the areas for heat loss of the inlet and outlet ducts.

Transient Collector Performance

During rapid radiation changes, the Hottel-Whillier collector equation tends to overestimate the amount of solar energy collected due to the thermal inertia of the collector. Heat capacity effects of solar collectors have been studied by Klein et al (1974)

and Wijesundera (1978). Duffie and Beckman (1980) divide the effects of thermal heat capacity on collector performance into two parts. One part is due to the heating of the collector from its early morning low temperature to its final operating temperature in the afternoon. The second part is due to intermittent changes during the day whenever the driving forces such as solar radiation and wind change rapidly. If collector heat capacity effects are significant, the second part should be the most important.

Duffie and Beckman (1980) presented a model for a flat-plate collector that starts from the equations for the collector absorber plate and the collector cover. The subscripts c and p represent cover and plate. Using the assumption that the ratio $(T_c - T_a)/(T_p - T_a)$ remains constant at its steady-state value, the differential equations are reduced to the following differential equation for the plate temperature

$$(mC)_p \frac{dT_p}{dt} = A_c [S - U_L(T_p - T_a)] \quad (2.2.5)$$

where $(mC)_c$ is the effective heat capacity which reduces the heat capacity of the cover, $(mC)_o$ to an equivalent heat capacity referred to the absorber plate temperature. The effective heat capacity of a collector with n covers is given by

$$(mC)_e = (mC)_p + \sum_{i=1}^n \frac{U_{L_i}}{U_{L_{i+1}}} (mC)_{i+1} \quad (2.2.6)$$

where $U_{L_{i+1}}$ is the loss coefficient from the i th cover to the ambient air, and $(mC)_p$ is the heat capacity of the absorber plate. Wijesundera (1978) showed that Equation 2.2.6 describes the changing plate temperature with an error of less than 10% for a single glass collector and less than 15% in error for two and three cover collectors. This accuracy is fully sufficient for most studies of collector heat capacity effects [Duffie and Beckman (1980)].

From the solution of Equation 2.2.6 Duffie and Beckman (1980) found that the collector time constant, τ , is (see Section 3.3 for definition of τ)

$$\tau = \frac{(mC)_e}{A_c U_L} \quad (2.2.7)$$

Equation 2.2.6 is strictly speaking only valid for solar collectors with no flow rate. In practice much of the collector heat capacity effects due to intermittent sunshine happen at flow conditions. Jimenez-Fernandez (1985) derived a model for the solar collector response that includes the effect of the flow rate. The model for the mean fluid temperature, T_{fm} , response is

$$(mC)_k \frac{dT_{fm}}{dt} = F' A_c [S - U_L(T_{fm} - T_a)] - m c_p (T_o - T_i) \quad (2.2.8)$$

Assuming: $m c_p (T_o - T_i) = (m C_p) (T_{fm} - T_i)$ [Jimenez-Fernandez (1985)], where $(m C_p)$ is the effective flow rate that allows the collector output to be described in terms of the mean fluid temperature, the solution of the differential Equation 2.2.8 for a step radiation change is

$$T_{fm}(t) = [T_{fm}(0) - T_{fm}^s] c \left[\frac{-F' A_c U_L t}{1 - \frac{F' R}{F'}} (m C)_k \right] + T_{fm}^s \quad (2.2.9)$$

where $T_{fm}(0)$ is the initial mean fluid temperature and T_{fm}^s is the final steady state temperature. By the above assumption the temperature difference $(T_{fm} - T_i)$ is proportional to $(T_o - T_i)$. Thus, the time constant for the collector output response from Equation 2.2.9 is

$$\tau = \frac{1 - \frac{F' R}{F'}}{F'} \frac{(mC)_k}{A_c U_L} \quad (2.2.10)$$

Since F and Fr can be close to 1 [Duffie and Beckman (1980)], it is seen that there is a large difference between the time constants of Equations 2.2.7 and 2.2.10, corresponding to a collector at no flow and under flow conditions, respectively. Since Equation 2.2.7 for collectors with zero flow is used in the textbook by Duffie and Beckman (1980), the time constants commonly found in the literature are generally specified too high. A typical time constant for a liquid flat-plate collector with a flow rate of 0.02 kg/s m^2 is 1 minute [Jimenez-Fernandez (1985)].

2.2.2 Storage Tank Modelling

Gordon and Zarmi (1985) pointed out the destruction of the quality of heat occurring in well mixed storage tanks and proposed the design of single pass systems. Both, variable volume and highly stratified fixed volume systems operating at low collector flow rates ("micro-flow") can have a significantly greater thermal performance than high flow rate conventional systems (as much as 25% [Jesch and Brown (1984)]).

Duffie and Beckman (1980) offer a numerical node model for the complex problem of the simulation of a stratified liquid storage tank. An analytical model for the effect of storage tank stratification appeared by Phillips and Dave (1982). They proposed the increase in the performance of a liquid-based solar system due to stratification to be accounted by a stratification coefficient in the basic governing equation; the storage is correspondingly modelled as fully mixed.

More recently a newer concept in tank models, the "plug flow" models, has been used. The use of large numbers of nodes and the use of the plug flow models result in better representation of well stratified tanks. These models and their use are given by Velcamp (1980), Wuestling et al. (1985), and the TRNSYS Manual [Klein et al. (1988)].

2.2.3 Thermal Design Methods

Thermal design methods give estimates of long-term solar system performance, but they do not provide information on process dynamics. Design methods for solar thermal systems can be divided into four general categories, according to the assumptions on which they are based and the ways in which the calculations are done:

- (1) Utilizability methods
- (2) Correlation methods
- (3) Analytical methods
- (4) Short-cut simulation methods

Utilizability Methods

The first category applies to systems in which the collector operating temperature is known or can be estimated and for which critical radiation levels can be established. The hourly utilizability method [Whillier (1953) and Hottel and Whillier (1958)] yields the long-term average collector performance for a collector operated at constant fluid inlet to ambient temperature difference and requires one calculation per month for every hour of the day. The utilizability method considers the effect of radiation fluctuations and allows the average hourly collector performance to be expressed in terms of a monthly average value of hourly radiation, \bar{I}_r .

$$\bar{Q}_a = A_c Fr (\tau\alpha) \bar{I}_r \phi \quad (2.2.11)$$

where, ϕ , the hourly utilizability is defined as

$$\phi = \frac{1}{N} \sum_{j=1}^N \frac{(I_{r,j} - I_{r,c})^+}{\bar{I}_r} \quad (2.2.12)$$

where N is the days in month, ϕ is the fraction of energy of the incident solar radiation that a solar collector, operating at threshold, $I_{r,c}$ can at most convert into useful energy. The utilizability method was generalized by Liu and Jordan (1963) with the cumulative frequency distribution of hourly (daily) insolation values. The procedure for calculating ϕ is illustrated in Figure 2.2.2 (a), where a cumulative frequency distribution curve $I_r(F)$ for measured radiation incident on a vertical surface for the hour pair 11-12 and 12-13 is plotted. Figure 2.2.2 (b) shows the corresponding utilizability curve, which is obtained by integrating $\phi =$ [dashed area] of Figure 2.2.2 (a) for different values of $X_c = I_{r,c} / I_r$. Also shown is a curve for the case that all hours of the month are identical (no fluctuations). This elegantly illustrates the effect of radiation fluctuations on the collector performance.

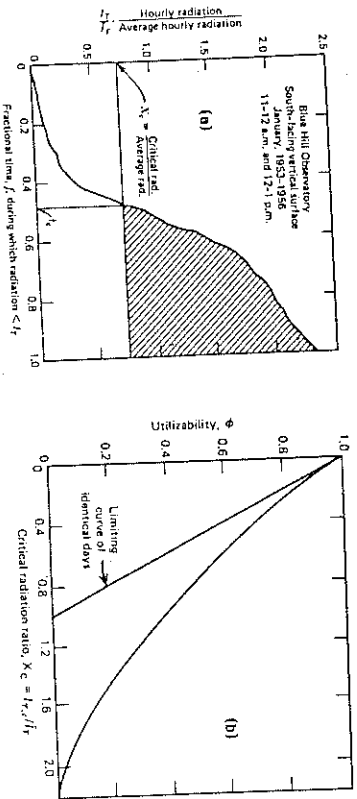


Figure 2.2.2 Utilizability: (a) Cumulative distribution curve for hourly radiation on a south facing vertical surface in Blue Hill, MA, USA; (b) Utilizability curve derived by numerically integrating Figure 2.2.2 (a). Adopted from Duffie and Beckman (1980).

Klein (1978) and Collares-Pereira and Rabl (1979) independently extended the hourly utilizability method to daily utilizability to reduce the computation effort, where the latter included concentrating collectors.

The limitation of the utilizability method is that it applies only for collectors being operated at a constant inlet to ambient temperature difference. Also, the discussion on the collector performance makes clear that the utilizability method yields the collector performance under the assumption that the collector has a zero time constant. In other words, for the utilizability method, it is implicitly assumed that collector heat capacity effects can be neglected.

Correlation Methods

The second category of design methods includes those that are correlations of the results of a large number of detailed simulations. A widely used correlation method that yields the system performance for the special case that the minimum load delivery temperature is 20°C is the F-chart method of Klein et al. (1977). The F-charts have been developed for three standard system configurations, liquid and air systems for space (and hot water) heating, and systems for service of hot water only.

Detailed simulations of these systems have been used to develop correlations between dimensionless variables and f , the monthly fraction of loads carried by solar energy. The two dimensionless groups are

$$X = \frac{A_c \bar{F}_R U_L (T_{in} - \bar{T}_m) \Delta t}{L} \quad (2.2.13)$$

$$Y = \frac{A_c \bar{F}_R (\bar{T}_c) \bar{H}_R N}{L} \quad (2.2.14)$$

- where A_c = the collector area [m^2]
 F_R = the collector-heat exchanger efficiency factor
 U_L = the collector overall heat loss coefficient [$W/m^2 \cdot ^\circ C$]
 Δt = the number of seconds in the month
 \bar{T}_a = the monthly average ambient temperature [$^\circ C$]
 T_{ref} = an empirically derived reference temperature ($100^\circ C$)
 L = the monthly total heating load for space heating and hot water [J]
 \bar{H}_T = the monthly average daily radiation incident on the collector surface [J/m^2]
 N = the number of days in the month
 $(\bar{\tau \alpha})$ = the monthly average transmittance-absorptance product

The first group describes the ratio of total absorbed energy on the collector absorber plate to total load; the second group represents the ratio of reference collector heat loss to total load. The result for a liquid-based system is

$$f = 1.029Y - 0.065X - 0.245Y^2 + 0.018X^2 + 0.0215Y^3 \quad (2.2.15)$$

for $0 < Y < 3$ and $0 < X < 18$.

Klein, Beckman and Duffie (1979) combined the daily utilizability with the f -chart concept to allow minimum load supply temperatures other than $20^\circ C$. The resulting $\bar{\phi}$ -chart method assumes a fully mixed storage tank and requires the load to be in closed loop, where the load is supplied above one minimum temperature T_{min} (the return temperature from the load is always at or above T_{min}). The auxiliary is in parallel to the storage tank and "takes over" once the supply temperature drops below T_{min} . Braun, Klein and Pearson (1983) extended the $\bar{\phi}$ -chart method to include open loop systems by characterizing the load by two temperatures, the supply temperature and the tank return/make up temperature. The auxiliary is in series with the load and adds heat once the supply temperature drops below a set value. The $\bar{\phi}$ -chart method is probably the best design method available although it is not as easy to use as the f -chart method. The disadvantage of both correlation methods, f -chart and $\bar{\phi}$ -chart, is the indirectness to the actual physics involved in the performance prediction. They appear for the user like a recipe.

Analytical Methods

An analytical method to predict the long-term performance of solar thermal systems with well mixed storage was introduced by Gordon and Zarmi (1985). Another method for air systems was developed by Ajona and Gordon (1987). The method by Gordon and Zarmi is based on the utilizability method, where an effective radiation ratio, \bar{X}_{eff} , is calculated with a constant radiation model, $\bar{H} = \bar{I}_{day}$, which enables the analytical solution of the system differential equation. Analytical approaches are particularly suitable for solar system optimization, but have the disadvantage that they apply only for simplified solar system configurations, and are system operation specific.

Short-Cut Simulation Methods

The fourth category of design methods is based on short-cut simulations. In these methods, simulations are done using representative days of meteorological data derived from statistical data and the results are related to long term performance. The methods presented are the TMD method by Feuermann et al. (1985) and the MIRA method by Reddy et al. (1987).

The TMD method substitutes the distribution of the average radiation over the day with the mirror image of two cumulative frequency distributions, corresponding to the average daily clearness index of the average day. However, the claim that this ensures the correct frequency of occurrence of radiation values on the collector is questionable. The typical meteorological day constructed in this manner puts all the high radiation values (clear sky values) into the center of the day, hence implying that noon hours have a higher frequency of clear sky radiation than hours during morning or afternoon. This is unrealistic, and the correct frequency of occurrence of radiation values should be satisfied during all hours of the day.

The MIRA method considers the "correct" frequency distribution for all hours of the day by successive hourly utilizability evaluations for the collector performance. The hourly utilizability is evaluated for every hour of the day, where the average hourly radiation is given by the average distribution of radiation over the day. The MIRA method has two subtle faults. The utilizability concept was originally devised to save the user the integration for the collector performance over the radiation fluctuation. However, when a numerical solution of the system performance equation is performed anyhow, the integration for the collector performance is trivial. This way, the collector performance calculation with the utilizability method only complicates matters, i.e., the simulation is not as direct as it could be. More fundamental is the problem that the utilizability, ϕ , yields only the quantity of heat not the quality. This means for simulations wanting to consider storage tank stratification that the information on the fluctuating collector outlet temperature is lost.

Both typical meteorological day methods neglect the (weak) correlation between successive radiation values, i.e., the effect of the order of occurrence of the daily insolation values, but satisfy the cumulative frequency distribution. Fixing the daily average radiation to monthly average for every day of the month, also neglects the fluctuations of the average. This leads to performance over-predictions for solar fractions exceeding 80% [Reddy (1987)] since the uniform distribution of average radiation over the month does not account for energy dumping. However, the typical meteorological day simulation method is very attractive through its simplicity and directness to the problem of long-term performance prediction of solar energy systems and should receive attention.

2.2.4 Simulation Methods

Simulations are the most powerful tool for analysis and design of solar thermal systems. The essential point of the simulation method is the numerical solution of the system performance equation, which represents a heat balance on the storage tank. The governing energy balance equation for a liquid-based solar system with fully mixed tank is derived in Chapter 3. This first order differential equation cannot in general be solved analytically due to the complicated dependence of the instantaneous radiation on time and the presence of a controller switching the collector pump on only when there is some energy gain.

However, with a numerical solution, the controller is most easily considered. The most widely used computer simulation program is TRNSYS [Klein et al. (1988)]. It is important to realize that every computer simulation program can only be as accurate as the solar radiation fed into the simulation. An advantage of the conventional simulation method is that it can handle any type of system configuration and that it predicts the performance under the condition that collector, storage and other system components are coupled together. The disadvantage of the conventional simulation method is that it requires long-term detailed meteorological data, which may not be available for the location under consideration.

The generation of synthetic radiation sequences equivalent to actual solar radiation offers the use of the simulation method without the need for long-term detailed meteorological data. The synthetic radiation generation can be divided into two parts. Firstly, for each month of the year a daily radiation sequence satisfying the frequency distribution of daily radiation values and the correlation between successive days is generated. The procedure of Graham et al. (1988) is recommended for this purpose. Secondly, the correlation of Collares-Pereira and Rabl (1979) may be used to each daily radiation value in the

sequence to generate the desired instantaneous (hourly) solar radiation. A good comparison between correlation methods and the simulation approach is given by Klein (1987).

2.3 Solar Radiation

The sun emits an electromagnetic radiation spectrum into space approximately equal to that of a black body at 6000 K. The term short-wave solar radiation denotes radiation of wavelength between 0.3 to 3.0 μm , which contains more than 98% of energy of the sun's radiation spectrum. This research deals with broadband solar radiation models, i.e. the models are not spectrally dependent. The broadband assumptions greatly simplifies solar radiation models by eliminating the need to integrate over all wavelengths.

But what makes the prediction of the terrestrial solar radiation so difficult? The solar radiation in space outside the earth's atmosphere (extraterrestrial radiation) is practically constant and varies by only 7% through the slightly elliptic orbit of the earth around the sun. With n the day number, the extraterrestrial radiation normal to the sun's beam, G_{on} can be expressed as [Duffie and Beckman (1980)]

$$G_{on} = G_{sc} \left(1 + \cos \frac{2\pi n}{365} \right) \quad (2.3.1)$$

The average normal incident radiation (often called the solar constant), G_{sc} , corresponding to the average sun-earth distance that would be received without the presence of an atmosphere on the earth's surface is $\approx 1367 \text{ W/m}^2$ [Iqbal (1983)]. However, in the presence of the atmosphere the terrestrial radiation is highly variable. When solar radiation enters the earth's atmosphere as beam radiation, it is attenuated. The attenuation of the incident energy is due to two phenomena, (1) atmospheric scattering by air

molecules, water vapor, and dust, and (2) atmospheric absorption by ozone in the ultraviolet and water vapor in bands in the infrared.

In the current state of solar radiation research on the availability of terrestrial radiation, the attenuation and fluctuation of solar radiation is considered on the basis of hourly radiation values. It is questionable, if the fluctuation of integrated hourly radiation values is representative of instantaneous or short-time integrated radiation. However, the analysis performed in Section 3.4 shows that the effect of using hourly rather than instantaneous radiation values on the long-term system performance can be ignored.

Since solar radiation is the driving force for solar energy systems, accurate radiation values are essential for meaningful simulation results. Incorrect or unrealistic solar radiation data can abrogate proposed solar system designs which result from the simulations. Actual measurements of hourly solar radiation data would be desirable for input but are probably not available for the location and collector orientation under consideration. Accordingly, these data have to be predicted from alternative observations relating more or less explicitly to horizontal surfaces.

If hourly global horizontal radiation data for the site under consideration is available, two problems exist: first, determining the fraction of the global radiation which is diffuse (or beam); second, estimating the total radiation on a tilted surface of any orientation.

2.3.1 Determination of Horizontal Diffuse Radiation

By measuring (or estimating) the global radiation on a horizontal surface, I , and calculating the diffuse radiation, I_d , the beam radiation component, I_b , can be calculated by

$$I_b = 1 - I_d$$

$$(2.3.2)$$

Fundamentally there are two methods for estimating the diffuse (or beam) radiation on a horizontal surface: empirical correlations or solving the radiative transfer equation. The two methods differ greatly in computational effort and information required to evaluate the diffuse (or beam) radiation. In this work, only empirical correlations will be considered because of their computational simplicity which is very important in simulation studies of solar energy systems.

Early work by Liu and Jordan (1960) showed a relationship between daily diffuse and daily total radiation on a horizontal surface. Other authors have developed diffuse fraction correlations specifically for hourly intervals. Erbs et al. (1980) and Ongill and Hollands (1977) have developed diffuse fraction correlations as a function of k_t . Stauter and Klein [Duffie and Beckman (1980)] used a clearness index, k_c , where a "clear sky" radiation, I_0 , replaced extraterrestrial radiation in the definition of k_t .

The models based on k_t (referred to as Liu- and Jordan-type models) are convenient because the only required input is hourly global horizontal radiation. The main drawback with using Liu and Jordan type models is the high standard error associated with estimating the hourly diffuse fraction. Figure 2.3.1 illustrates the problem of predicting the hourly diffuse fraction as a function of k_t . It is obvious that the hourly diffuse fraction is not a function of k_t alone.

Iqbal (1980) and Skartveit and Ojseth (1987) suggested that the second most important variable after k_t is the solar altitude, α . Reindl (1988) showed that the four best predictors to correlate the diffuse fraction were k_t , $\sin \alpha$, ambient temperature, T_a , and relative humidity, ϕ .

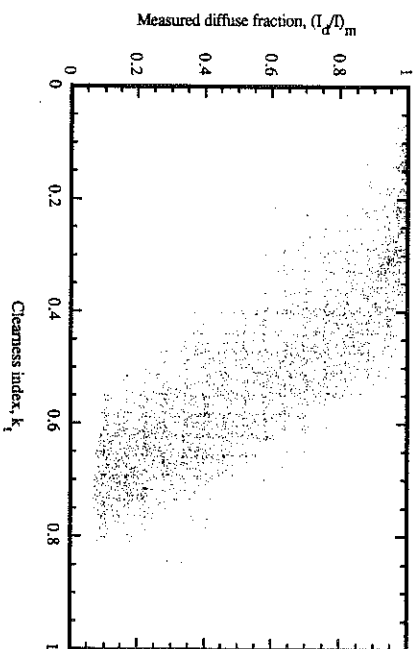


Figure 2.3.1 Diffuse fraction versus clearness index for Oslo, Norway.

The Liu and Jordan model (1960) is based on 10 years of data (1947-1956) from Blue Hill-Massachusetts, USA (42°N). The correlation is given by:

$$I_d/I = 1.0045 + 0.04349k_t - 3.5227k_t^2 + 2.6313k_t^3 \quad k_t \leq 0.75 \quad (2.3.3)$$

$$I_d/I = 0.166 \quad k_t > 0.75 \quad (2.3.4)$$

Although this correlation is a daily rather than an hourly model it has been applied to hourly data by many authors.

Erbs et al. (1980) used a database composed of four U.S. locations to develop an hourly diffuse fraction correlation as a function of the clearness index. Erbs chose to use a three piece curve to fit the diffuse fraction.

$$I_d/I = 1.0 - 0.09k_t \quad k_t \leq 0.22 \quad (2.3.5)$$

$$I_d/I = 0.9511 - 0.1604k_1 + 4.388k_1^2 - 16.638k_1^3 + 12.336k_1^4 \quad (2.3.6)$$

$$0.22 < k_1 \leq 0.8$$

$$I_d/I = 0.165 \quad k_1 \leq 0.8 \quad (2.3.7)$$

Skartveit and Oieath (1987) used fourteen years of data (1965-1979) from Bergen, Norway (60.4 °N) to develop an hourly diffuse fraction correlation as a function of the clearness index and the solar altitude angle. The fourteen years of data yielded 44,687 valid hourly periods to create the three piece curve fit of I_d/I .

$$I_d/I = 1.0 \quad k_1 \leq 0.2 \quad (2.3.8)$$

$$I_d/I = f(k_1) = 1 - (1-d_1) \cdot (0.27K^{0.5} + 0.73K^2) \quad 0.2 < k_1 \leq 1.09k_1 \quad (2.3.9)$$

$$I_d/I = 1 - 1.09k_1(1 - f(1.09k_1))/k_1 \quad k_1 \geq 1.09 \quad (2.3.10)$$

where

$$K = 0.5 \cdot \left[1 + \sin \left(\frac{k_1 - 0.2}{k_1 - 0.2} - 0.5 \right) \right]$$

$$k_1 = 0.87 - 0.56e^{-0.06\alpha}$$

$$d_1 = 0.15 + 0.43 \cdot e^{-0.06\alpha}$$

This correlation is plotted versus the clearness index for fixed solar altitude angles together with the Liu and Jordan, and the Erbs correlation in Figure 2.3.2. The solar altitude effects are clearly seen at high values of k_1 (clear skies). For clear sky condition, the diffuse fraction increases for decreasing solar altitude angles due to the longer path length required for radiation to travel.

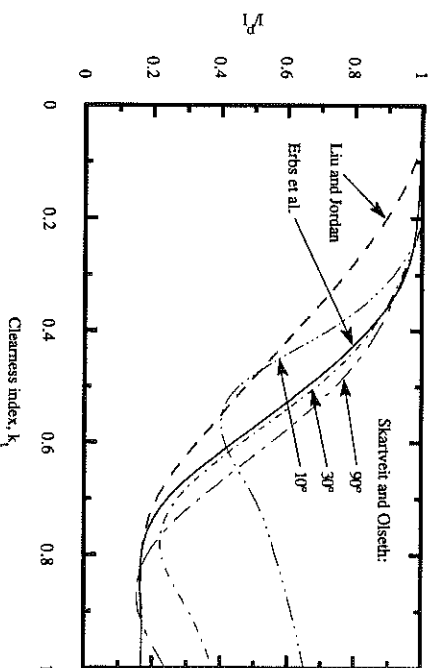


Figure 2.3.2 Diffuse fraction correlations: Liu and Jordan, Erbs, and Skartveit and Oieath.

Recently Reindl et al. (1988) used a database composed of five locations (Albany-New York, USA; Cape Canaveral-Florida, USA; Hamburg, West Germany; Valentia, Italy; and Copenhagen, Denmark) to develop an hourly diffuse fraction correlation.

$$I_d/I = 1.00 - 0.232k_1 + 0.0239\sin\alpha - 0.000682T_a + 0.0195\phi \quad k_1 \leq 0.3 \quad (2.3.11)$$

$$I_d/I = 1.329 - 1.716k_1 + 0.267\sin\alpha - 0.00357T_a + 0.106\phi \quad 0.3 < k_1 < 0.78 \quad (2.3.12)$$

$$I_d/I = 0.426k_1 - 0.256\sin\alpha + 0.00349T_a + 0.0734\phi \quad k_1 \geq 0.78 \quad (2.3.13)$$

This correlation is the result of an extensive study; we stepwise regression was used to reduce a large set of potential predictor variables down to four significant predictors, and is to the authors knowledge the most detailed diffuse fraction correlation there exist.

2.3.2 Total Radiation on Tilted Surfaces

Predicting the total radiation on a tilted surface requires knowing the diffuse and beam radiation on a horizontal surface. If diffuse (or beam) radiation measurements are not available, the methods described in Section 2.3.1 must be used to estimate the hourly diffuse radiation. In this section, methods for projecting the horizontal radiation components onto a tilted surface are presented.

The total radiation on a tilted surface, I_T , is made up of three components: beam radiation, I_{bT} , diffuse solar radiation, I_{dT} , and solar radiation diffusely reflected from the ground, I_{gT} .

$$I_T = I_{bT} + I_{dT} + I_{gT} \quad (2.3.14)$$

The decomposition of the total radiation incident on the tilted surface into the above three components is illustrated in Figure 2.3.3. The methods for estimating each radiation component on a tilted surface are described below.

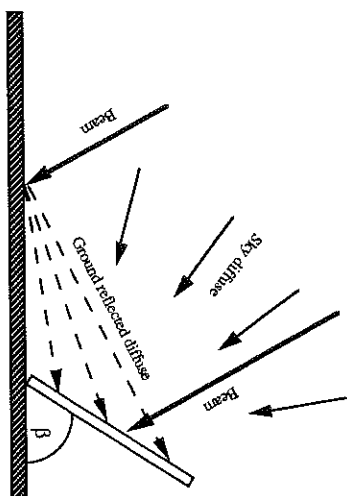


Figure 2.3.3 Incidence of beam, sky diffuse, and ground-reflected radiation on an inclined surface.

Beam Radiation

Duffie and Beckman (1980) define the geometric factor, R_b , as the ratio of hourly (or instantaneous) beam radiation on a tilted surface to the hourly beam radiation on a horizontal surface. The ratio I_{bT}/I_b is given by

$$R_b = I_{bT}/I_b = \cos \theta / \cos \theta_2 \quad (2.3.15)$$

Thus, the beam radiation on a tilted surface is

$$I_{bT} = I_b R_b \quad (2.3.16)$$

When values of either θ or θ_2 exceed 90° , the beam radiation on the inclined surface will be zero. If θ is greater than 90° , the sun is behind the collecting surface, while the sun is below the horizon when θ_2 is greater than 90° .

Ground Reflected Radiation

A common method for calculating the ground reflected radiation incident on a tilted surface is to assume the foreground in the collector field of view is a diffuse reflector and that the horizon is unobstructed. Other authors have proposed anisotropic ground reflectance models [Skarveit and Olseth (1986) and Gardner and Nadeau (1988)] but the lack of experimental data has hindered their validation. Therefore, the ground reflected radiation is assumed to be isotropic and is obtained by [Duffie and Beckman (1980)],

$$I_{gT} = I \rho_g \left(\frac{1 - \cos \beta}{2} \right) \quad (2.3.17)$$

where ρ_g is the ground reflectance.

Sky Diffuse Radiation

Diffuse sky radiation is difficult to model since its angular distribution is generally unknown and time dependent. Based on measurements of the diffuse radiation across the principle plane [Kondratyev (1969); Temps and Coulson (1977); McArthur and Hay (1981)] several authors [Kuchler (1979); Perez et al. (1987); and Reinl et al. (1988)] introduce three subcomponents to approximate the anisotropic behavior of diffuse radiation: circumsolar, horizon brightening, and isotropic diffuse radiation. Circumsolar radiation is predominantly forward scattered radiation resulting from aerosols in the atmosphere. Horizon brightening is the increase in diffuse radiation near the horizon due to an increase in scattering of the incident radiation as it passes through the longer pathlength of atmosphere near the horizon and by multiple internal reflections within the earth's atmosphere. Isotropic is the remaining portion of diffuse radiation assumed to be uniformly distributed over the sky dome.

Figure 2.3.4 shows contour maps of intensity distribution under clear skies (a), under partly cloudy skies (b), and under overcast skies (c). High circumsolar radiation and horizon brightening are apparent in Figure 2.3.4 (a). In Figure 2.3.4 (b) the circumsolar radiation is still clear but the horizon brightening is less pronounced. It is apparent from Figure 2.3.4 (c) that in the case of an overcast sky, the radiation is not completely isotropic over the sky dome. It is seen to have a maximum at about a zenith angle of 0° , significantly in contrast to the isotropic sky assumption. Skartveit and Olesen (1986) used similar results reported by Robinson (1966) to model this anisotropy under overcast skies.

Four existing tilted surface models are presented: isotropic [Hottel and Woertz (1942)], Hay and Davies (1980), Skartveit and Olesen (1986), and Perez (1987). A new model based on the work by Olesen and Skartveit (1986), and Klucher (1979) is developed and presented in Chapter 4. In all of these models, the direction of beam radiation is

accounted for by the use of R_b and isotropic ground-reflected radiation is assumed; the differences are in the treatment of diffuse sky radiation.

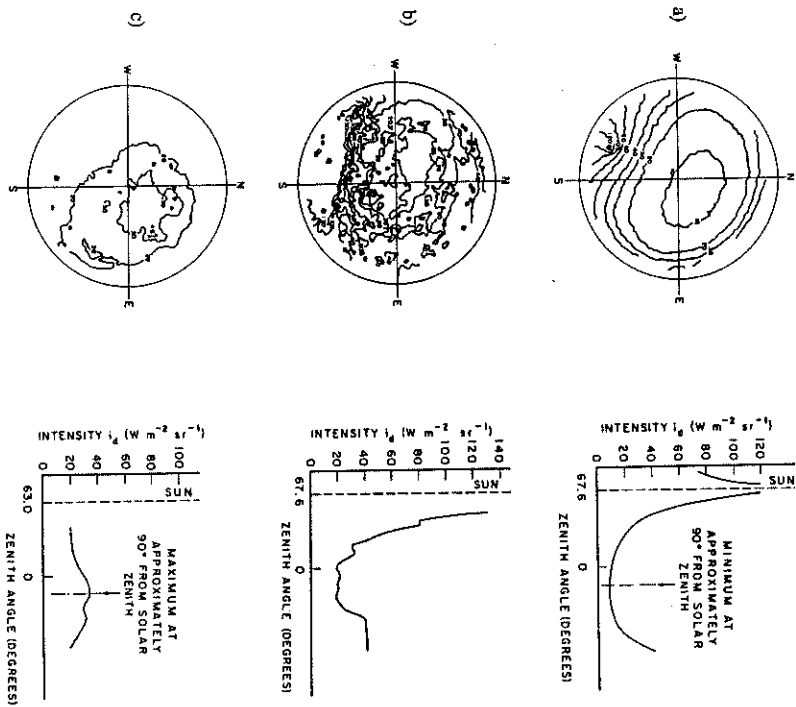


Figure 2.3.4 Angular variation of the sky diffuse intensity under (a) clear skies; (b) partly cloudy skies; (c) overcast skies. Adapted from McArthur and Hay (1981).

The isotropic model assumes that the diffuse radiation is uniformly distributed over the entire sky dome. A surface tilted at a slope β from the horizontal has a view factor to the sky given by $\cos^2(\beta/2) = (1 + \cos \beta)/2$. The diffuse radiation on a tilted surface is therefore given by

$$I_{dT} = I_d \left[\frac{1 + \cos \beta}{2} \right] \quad (2.3.18)$$

The isotropic model is the simplest of the tilted surface models as no anisotropic effects is included.

Hay and Davies (1980) developed a model which divides the diffuse radiation on a horizontal surface into a circumsolar component, ($\tau_b I_d$), and an isotropically distributed component, $(1 - \tau_b) I_d$. Here, τ_b is the atmospheric transmittance to the beam radiation component (also called the anisotropy index) which is the ratio between the hourly direct normal beam radiation, I_{bn} , and the hourly extraterrestrial radiation at normal incidence, I_{ae} . Since the circumsolar diffuse radiation originates from a region in the neighborhood around the sun, it is projected onto the tilted surface in the same fashion as beam radiation. The complete Hay and Davies model is given by the following relationship

$$I_{dT} = I_d \left[\tau_b R_b + (1 - \tau_b) \left(\frac{1 + \cos \beta}{2} \right) \right] \quad (2.3.19)$$

Under clear skies, τ_b will be high and the circumsolar component is weighted more heavily than the isotropic component. Under cloudy skies, τ_b goes to zero and the diffuse sky radiation is treated as isotropic.

Skartveit and Olsbeth (1986) proposed an anisotropic model to estimate the diffuse sky radiation on a tilted surface which accounts for anisotropy effects both at overcast and cloudless weather. This model is the result of modifications made to Hay and Davies

model. In his study of solar radiation Robinson (1966) reported that the diffuse radiation on a tilted surface at overcast is proportional to $\cos^3(\beta/2)$, significantly in contrast to the $\cos^2(\beta/2)$ -proportionality occurring under the isotropic sky radiation assumption. To model this anisotropic behavior Skartveit and Olsbeth (1986) assumed that at overcast a fraction $Z_e = 30\%$ of the diffuse radiation on a horizontal surface is due to diffuse radiation from zenith, and the remaining 70% is treated as isotropic diffuse. This zenith brightening declines rapidly with reduced cloudiness, and vanishes at about 75-50% [Robinson (1966)], corresponding to a τ_b equal to 0.15 [Skartveit (1976)]. Skartveit and Olsbeth modified version of the Hay model for the diffuse sky radiation on a tilted surface is given by

$$I_{dT} = I_d \left[\tau_b R_b + Z_e \cos \beta + (1 - \tau_b - Z_e) \left(\frac{1 + \cos \beta}{2} \right) \right] \quad (2.3.20)$$

where

$$Z_e = 0.3 - 2\tau_b$$

For τ_b larger than 0.15 Skartveit and Olsbeth model reduces to the Hay model.

The Perez et al. model (1987) accounts for circumsolar, horizon brightening, and isotropic diffuse radiation by empirically derived "reduced brightness coefficients". The reduced brightness coefficients, F_1 , F_2 are functions of the sky clearness, e , and sky brightness, A , parameters.

$$e = \frac{\left[\frac{(I_d + I_{bn})}{I_d} + 1.041 \theta_z^3 \right]}{1 + 1.041 \theta_z^3} \quad (2.3.21)$$

$$A = \frac{I_d}{I_0} \quad (2.3.22)$$

The sky clearness and sky brightness parameters are used to calculate the reduced brightness coefficients from the following relationships and Table 2.3.1.

$$F_1 = F_{11}(\epsilon) + F_{12}(\epsilon) \Delta + F_{13}(\epsilon) \theta_2 \quad (2.3.23)$$

$$F_2 = F_{21}(\epsilon) + F_{22}(\epsilon) \Delta + F_{23}(\epsilon) \theta_2 \quad (2.3.24)$$

Table 2.3.1 Intermediate brightness coefficients.

ϵ bin	Upper limit	F_{11}	F_{12}	F_{13}	F_{21}	F_{22}	F_{23}
1	1.056	-0.011	0.748	-0.080	-0.048	0.073	-0.024
2	1.253	-0.038	1.115	-0.109	-0.023	0.106	-0.037
3	1.586	0.166	0.909	-0.179	0.062	-0.021	-0.050
4	2.134	0.419	0.646	-0.262	0.140	-0.167	-0.042
5	3.230	0.710	0.025	-0.290	0.243	-0.511	-0.004
6	5.980	0.857	-0.370	-0.279	0.267	-0.792	0.076
7	10.08	0.734	-0.073	-0.228	0.231	-1.180	0.199
8	-	0.421	-0.661	0.097	0.119	-2.125	0.446

The magnitude of the reduced brightness coefficients weight the respective circumsolar, horizon brightening, and isotropic diffuse radiation components. The angular location of the circumsolar region is determined by the ratio a/c .

$$a = \frac{\max[0, \cos \theta]}{\max[\cos \theta_1, \cos \theta_2]} \quad (2.3.25)$$

The tilted surface sky diffuse radiation can then be estimated by the following

$$I_{\text{sr}} = \left[0.5(1 - F_1)(1 + \cos \beta) + F_1 a + F_2 \sin \beta \right] \quad (2.3.26)$$

2.4 Transparent Insulation Materials

2.4.1 Introduction

In nearly all cases solar energy components need two basic elements: the thermal absorber and some transparent cover that reduces the heat losses from the absorber to the environment. Many efforts in the past have been undertaken in order to improve absorbers. Selective coatings have been developed in order to reduce IR-radiation losses from the absorber without losing its ability to absorb solar radiation.

Another approach is the use of transparent covers, which restrain heat transport more efficiently than conventional collector glazings. Convection suppressing devices such as specularly reflecting honeycomb structures should fill the space between absorber and cover to suppress the onset fluid motion [Hollands (1965), Edwards (1969), Meyer et al. (1978), and others], Symons et al. (1983), Hoogendoorn (1985), and Karlsson (1988) studied thin film structures as honeycombs and slats, and Teflon films with minimal thickness. These devices guarantee low transmission losses in the solar spectrum. They can easily be combined with selective coatings, because reemission from the plastic films, coupled to the absorber temperature by air conduction or even contact, is kept small.

By applying IR-absorbing materials the IR-radiation losses may be reduced appreciably without the need for selective coatings, and convection may be suppressed when dimensions are properly chosen [Platzer (1987)]. For the so called aerogel, even air conduction can be reduced due to the microporous structure [Fricke (1986) and Svendsen (1989)]. Up to now this has only been possible in evacuated tubes.

The most important characteristic of insulating materials is the total heat transfer coefficient, h_{tot} , defined as the heat flux through a material divided by the area and the

temperature difference between the boundary surfaces. The reason for applying the total heat transfer coefficient as the characterizing parameter rather than the heat conduction coefficient, $h_{\text{total}} (=k/L)$, based on the thermal conductivity, k , and the material thickness, L , is that for materials with low IR-radiation damping and significant gas convection, the heat conduction coefficient is not a material constant. The heat conduction coefficient depends on the material thickness. An opaque insulating material such as mineral wool with a thickness of 0.10 m has a total heat transfer coefficient of $0.35 \text{ W/m}^2\text{C}$ for a mean temperature of 40°C .

Transparent insulation materials has the solar transmittance as the second characterizing parameter. Combining the heat transfer coefficient and the solar transmittance into one "quality factor" is not possible, because the significance of each characteristic depends upon the application.

Thermal radiation, conduction and convection are strongly coupled heat transfer mechanisms in TIMs, and this interaction makes the calculations rather complicated. However, neglecting the interaction between the different heat transfer modes would lead to significant errors, and should be avoided.

2.4.2 Classification of Transparent Insulation Materials

Transparent insulation materials (TIMs) may be divided into low-emissive and strongly absorbing covers or they could be grouped according to the transmission characteristics of the cover. A better way seems to be the approach presented by Platzer (1987). He based the classification on the geometrical structure of the TIM. This is very reasonable because every geometry needs its own theory concerning solar transmission and infrared heat transfer.

The four different TIM groups are illustrated in Figure 2.4.1. The first type is the so called absorber-parallel cover, consisting of one or more films or panes of glass with equal or different optical properties. The second group, represented by honeycomb structures or slats are termed absorber vertical TIMs. A combination of type one and type two are termed cavity structures. This group is represented by transparent foam with irregular shaped air filled bubbles or multilayer plastic plates with regular shaped quadratic air ducts in between. The fourth type is typified by quasi-homogeneous materials with low thermal conductivity, and may be absorbing and/or scattering in the solar part of the spectrum. Silica aerogel and glass fiber materials belong to this group.

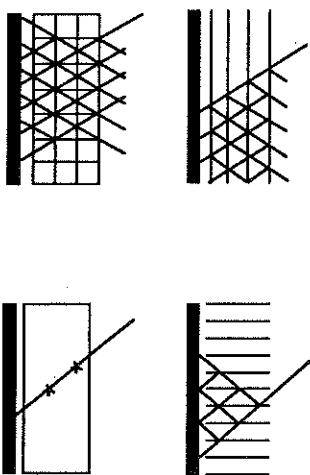


Figure 2.4.1 Classification of transparent insulation materials: (a) absorber-parallel covers, (b) absorber vertical covers, (c) cavity structures, (d) quasi-homogeneous materials. Adapted from Platzer (1987).

2.4.3 Available Materials and Real Cover Systems

In recent years a large number of different TIMs and systems have been investigated on a laboratory scale, but only a few systems are commercially available. In the following some of these systems will be described in more detailed.

Absorber-Parallel and Cavity Structures

For flat-plate collectors in the low and medium temperature range a high $(\tau\alpha)$ -product is very important, whereas a low U_L value is less critical. For these applications, transparent cover systems were developed using a selective coated absorber in most cases and a highly transparent insulation material to suppress convection. Swedish companies have installed large area collector fields with different Teflon films (single, double, and V-corrugated) in the gap between the absorber and the cover glass. The characteristic data of these systems are shown in Table 2.4.1.

Table 2.4.1 Characteristic data of absorber-parallel and cavity structures used in a flat-plate collector operated at an over temperature of 55°C.

Name	Reference	1-Teflon Abs.- parallel	2-Teflon Abs.- parallel	V.c:Teflon Cavity	Isotflex Cavity
$\tau_{diff}(0)$	0.91	0.88	0.84	0.90	0.66
τ_{diff}	0.85	0.82	0.75	0.83	0.42
U_L [W/m ² °C]	3.7	2.8	2.5	2.65	3.2
Thickness [μm]		12.5	2•12.5	25.0*	

* The height is 22 mm and the corrugation angle is 25°.

From an economic point of view, field tests with large area collector systems in Sweden indicate that for district heating systems with seasonal storage, the absorber-parallel single Teflon film will be the best one at the time being [Karlsson, 1988].

Absorber-Vertical Structure

For systems working at higher temperatures, a low heat loss coefficient becomes very important. Of course a high $(\tau\alpha)$ -product is also beneficial. For such applications IR-

opaque honeycomb and capillary structures have been developed. These materials suppress the convection and IR-radiation very effectively [Wirtner (1983)]. A selective coating will be excessive at low temperatures, and they will only improve the efficiency at higher temperatures. The suppression of IR-radiation is a much stronger limitation than the prevention of convection. The optimization process will therefore be a question of how large the aspect ratio and how thick the films have to be chosen in order to obtain good damping of the IR-radiation without increasing the absorption and scattering of the incoming solar radiation to an unacceptable high level. In most of these systems convection in the structure will no longer be a problem.

Two types of materials are commercially available in large quantities: a square honeycomb material made from polycarbonate and capillary materials made from different materials with varying diameter of the capillaries. For both types the typical thickness of the plastic films are 20 - 50 μm. Typical characteristic data are given for some of these materials in Table 2.4.2. The data are measured with black absorbers ($\epsilon = 0.9$) on both sides and without an additional cover glass which has to be added in the application.

Table 2.4.2 Characteristic data of honeycomb and capillary structures. The measurements were performed at a temperature of 10 °C and a temperature difference of 10 °C between the boundaries.

Name	Honeycomb	Honeycomb	Capillaries	Capillaries
Material	Polycarbonate	Polycarbonate	Polycarbonate	PMMA
τ_{diff}	0.85	0.78	0.73	0.80
U_L [W/m ² °C]	2.0	1.07	0.98	0.91
Thickn. [cm]	5	10	10	10

Homogeneous Materials (Aerogel)

The utilization of these highly transparent and well insulating materials in window and cover systems started about ten years ago. At present time two different types of aerogels are available on a small scale for research and development. Tiles of monolithic silica aerogel (MSA) can be produced by drying a gel consisting of a very fine structure or network of silicon dioxide and methanol. The drying has to be carried out with the methanol in a super critical state in order to avoid the influence of the surface tension that would otherwise destroy the gel structure. At present tiles of 60 cm x 60 cm are produced, but it is expected to be possible to fabricate tiles with larger dimensions and at production prizes of about 20 US\$/m² for 2 cm thick tiles [Syvendsen (1989)]. The other type is granules of variable diameter (typical 1 - 10 mm), which are filled into the air gap in a doubled glazed window or a flat-plate collector. Table 2.4.3 shows the characteristic data of a double glazed window with different aerogel fillings.

Table 2.4.3 Characteristic data of aerogel samples between double glazing. The measurements were performed at a temperature of 10 °C and a temperature difference of 10 °C between the boundaries.

Name	MSA	Granules	Granules
Diameter [mm]		6 - 8	< 2
κ_{diff}	0.57	0.43	0.22
U_L [W/m ² °C]	0.95	1.15	0.98

In this work a flat plate collector based on evacuated monolithic silica aerogel will be theoretically investigated (see Chapter 5).

CHAPTER 3

Solar System Performance Prediction

3.1 Introduction

The design of solar thermal systems requires the determination of the long-term system performance. The system performance is measured in terms of the solar fraction, f , the fraction of the load that is met by solar energy alone. Once a performance prediction method is available for a certain system configuration, design variables like the collector area and storage size can be optimized with respect to the economic merits.

The value of a solar system is ultimately assessed in economic terms, and an optimization of a solar system comes down to the optimization of the economic viability. The optimization starts with the best choice of the type of solar system and eventually involves the optimum sizing of the solar system components.

The thermal performance of a solar system, as given by the solar fraction, describes the performance for a given set of design parameters. A solar system optimization repeatedly uses the thermal performance prediction to arrive at a system design that optimizes the economic benefits. The optimization depends very much on the "local economic climate" and the time span of the term of the economic analysis.

Economic analysis of solar systems are well presented by Duffie and Beckman (1980) and Reddy (1987). Such analysis require the prediction of the solar system performance, the annual solar fraction. The most versatile performance prediction method that can handle various solar system configurations (e.g., the arrangement of the auxiliary heater in line or

in parallel with the load) is the simulation method. The simulation method provides the solar system performance under the condition that the system components are coupled together since it can keep track of all the changing variables involved. The versatility extends to the consideration of different load patterns.

The simulation method not only provides the long-term system performance, but also useful information on other aspects of the solar system operation. For example, the range of expected storage tank temperatures and the need for energy relief valves to control boiling. The most important aspect of the simulation method is that it gives the user a physical insight into the dynamic behavior of the solar system. However, it should be mentioned that not all systems can easily be simulated and that design methods are of great practical importance.

3.2 Solar System Performance Equations

3.2.1 Model Development

Before the solar system performance can be calculated, an appropriate system model has to be developed. A system model is a collection of the component equations, which are to be solved subject to the forcing functions (meteorological data and load), using time as the independent variable. In general, the resulting set of simultaneous equations cannot be solved analytically, but a numerical solution is straightforward.

The system model depends on the type of solar system under consideration and the required accuracy of the model. The possibilities for choice of the system model are endless. For example, the forced or thermosiphon collector fluid circulation, or the control strategy for collector and load are factors in the determination of the model.

System models can become quite complex when the accuracy requirements are high. For example, the modeling of collector heat capacity effects or storage tank stratification can be quite involved.

However, often a basic model is sufficient to get started. The procedure of setting up a model is illustrated below for the simple case of a forced circulation liquid solar thermal system with fully mixed storage tank.

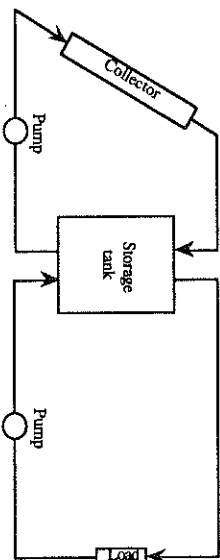


Figure 3.2.1 Schematic for the derivation of the performance equation for a liquid solar thermal system.

The solar system shown in Figure 3.2.1 can be considered as a closed system since there is no mass flow across the system boundary. Hence, the first law of thermodynamics for closed systems is applicable.

$$\frac{dU}{dt} = \frac{dW}{dt} + \frac{dQ}{dt} \quad (3.2.1)$$

where U = the internal energy of the system as characterized by the temperature [W/m^2]

W = the mechanical work transferred to the system [W/m^2]

Q = the heat that flows across the system boundary [W/m^2]

The electrical pump work can usually be neglected in a well designed system so that the only energy transport across the boundary is the heat flux. The electrical pump work on

the collector side is in the order of 30 kJ/m²hr, which is small compared to the collector output of order 1800kJ/m²hr. Therefore, the work term is negligible and Equation 3.2.1 becomes

$$\frac{dU_s}{dt} = \dot{Q}_a - \dot{Q}_s - \dot{Q}_l \quad (3.2.2)$$

Using the Hottel-Whillier collector equation for \dot{Q}_c with $T_f = T_s$ and expressing the storage tank heat loss as $\dot{Q}_s = (UA)_s (T_s - T_a)$, the following system differential equation is obtained.

$$(m C_p)_s \frac{dT_s}{dt} = A_c F_r [(\alpha \rho)_c G_r - U_L (T_s - T_a)] - (UA)_s (T_s - T_a) - \dot{Q}_l \quad (3.2.3)$$

where m = the mass of medium in the storage tank [kg]

C_p = the specific heat of medium in the storage tank [J/kg°C]

T_s = the uniform storage tank temperature [°C]

t = the time [s]

A_c = the collector area [m²]

F_r = the collector heat removal factor

$(\alpha \rho)_c$ = the effective transmittance-absorbance product

G_r = the instantaneous radiation on the collector surface [W/m²]

U_L = the overall collector heat loss coefficient [W/m²°C]

T_a = the ambient temperature [°C]

$(UA)_s$ = the storage tank loss coefficient-area product [W/m²°C]

T_a' = the temperature of the ambient air around the storage tank [°C]

\dot{Q}_l = the instantaneous heat load [W]

By means of Equation 2.2.2 to 2.2.4 the simple form of Equation 3.2.3 can be retained, even when a collector heat exchanger and pipe heat losses are considered. However, it should be said that Equation 3.2.3 may not be applicable for "micro-flow thermosiphon" systems since in this case the flow rate is not constant and factors like F_r may not be assumed constant. Equation 3.2.3 is only intended as an example.

The load may in general be a very irregular function of time. However, when the load pattern is known, it can be considered with the simulation method. An idealized case, is the case of constant load. Loads that are not too irregular may be approximated by a constant load. Solar systems usually have auxiliary heaters to ensure economical and reliable load supply. For thermosiphon type domestic water heaters the auxiliary heating coil is normally placed into the tank. For industrial type systems with approximately constant load the two load supply configuration shown in Figure 3.2.2 are common.

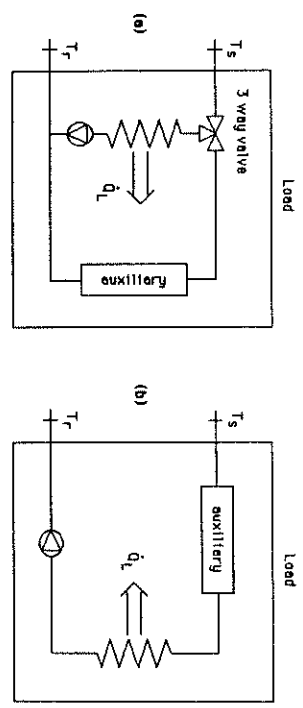


Figure 3.2.2 Two load supply configurations: (a) Auxiliary in parallel with the load; (b) Auxiliary in series with the load.

The load supply configuration shown in Figure 3.2.2 (a) has the advantage of simple control while the load supply configuration shown in Figure 3.2.2 (b) uses the tank as a preheater and requires less auxiliary power for large load temperature differentials. Mathematically the load configuration shown in Figure 3.2.2 can be expressed as

$$\text{Case (a): } \dot{Q}_l = \begin{cases} L \\ 0 \end{cases} \quad \text{for } \begin{cases} T_s \geq T_{min} \\ T_s < T_{min} \end{cases} \quad (3.2.4)$$

$$\text{Case (b): } \dot{Q}_L = \begin{cases} L & T_s \geq T_{\min} \\ L \frac{T_s - T_L}{T_{\min} - T_L} & T_s < T_{\min} \end{cases} \quad \text{for} \quad \begin{cases} T_s \geq T_{\min} \\ T_s < T_{\min} \end{cases} \quad (3.2.5)$$

where L denotes a constant load, T_L the load return temperature, and T_{\min} the minimum load supply temperature. This completes the example for the formulation of the model equations.

3.2.2 Numerical Solution of the System Performance Equation

Once the equation (set of equations) describing the model has been obtained, a numerical solution can be performed. The hot water solar system, as described by Equation 3.2.3, is used to illustrate the numerical solution of the performance governing system differential equation.

The first requirement for the numerical solution of Equation 3.2.3 is knowledge of the initial value of the storage tank temperature (e.g., at the beginning of the day). However, this requires prior knowledge of the solution and an estimate of the initial storage tank temperature is the best that can be done (e.g., $T_s(0) = T_{\min}$). Dependent on the property that the differential equation to be solved is stable, a numerical solution will then converge to the true solution. Since this property is essential for meaningful results, Section 3.2.3 deals with the convergence and accuracy of the simulation.

Section 3.2.3 shows that Equation 3.2.3 is stable. Using the fact that time constants of a solar thermal system with storage are very much larger than the step size used to solve Equation 3.2.3 numerically, the increase of the storage tank temperature is almost linear when it is considered that the driving radiation is assumed constant over the step size interval. Hence, a simple numerical solution method is sufficient. The simplest numerical

solution method for Equation 3.2.3 is the Euler method. The method is illustrated in Figure 3.2.3.

Using Figure 3.2.3, the storage tank temperature at time t_2 can be predicted from the storage tank temperature at time t_1 and the slope dT_s/dt at time t_1 by

$$T_s(t_2) = T_s(t_1) + \Delta t \left(\frac{dT_s}{dt} \right)_{t_1} \quad (3.2.6)$$

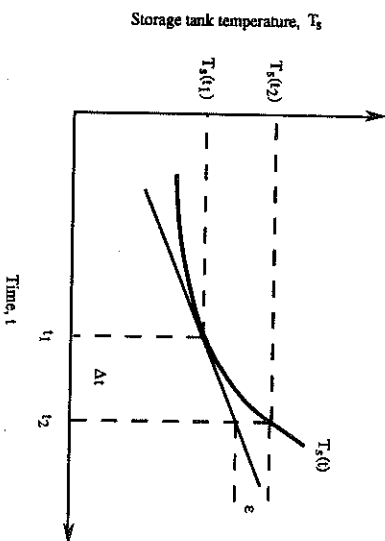


Figure 3.2.3 The Euler method for the numerical solution of a first order differential equation.

Although the accuracy of the simple Euler method is sufficient in many cases, for large step sizes, Δt , the truncation error, e , may become significant. A more accurate method that can handle larger time step is the Euler predictor-corrector method. Using the notation $T_s' = dT_s/dt$, the Euler predictor-corrector method is

$$T_s(t_2) = T_s(t_1) + \Delta V_2 [T_s'(t_1) + T_s'(t_2)] \quad (3.2.7)$$

where the slope $T_s'(t_2)$ is calculated from a (first) estimate of the storage tank temperature $T_s(t_2)$ using Equation 3.2.6.

3.2.3 Convergence and Accuracy of the Simulation Method

Convergence

Before any numerical solution of the system equations can be attempted, the stability of the differential equations has to be assured. To discuss the notion of stability consider a solar thermal system for the case of constant storage tank temperature T_s , i.e., consider the hypothetical case that the useful energy from the collector equals the load and the tank heat loss for some time. For the numerical solution of the differential equation a starting value T_s^* , generally different from the actual initial value (equilibrium value) $T_s(0)$, is guessed. Then three cases, as shown in Figure 3.2.4, have to be distinguished.

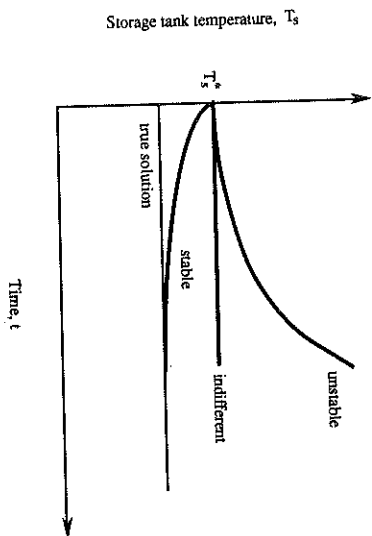


Figure 3.2.4 The stability of the system differential equation.

Figure 3.2.3 shows that a stable differential equation will approach the true solution, even if an erroneous starting value was supplied. The stability is not only important to cope with erroneous starting values (irrelevant for long-term simulations), but also to accommodate round off errors and truncation errors occurring during the solution.

It is claimed that Equation 3.2.3 is stable everywhere.

Proof: Consider first the above case of constant T_s for the true temperature profile and a numerical solution for this profile with starting value $T_s^* > T_s(0)$. Both, the true and the numerical solution are subject to the same radiation $Gr(t)$. Now, for the numerical solution the heat loss from the collector and storage tank will be greater than for the true solution since the heat loss depends on $(T_s^* - T_a)$ and $T_s^* > T_s$ by assumption. But this shows that the slope dT_s/dt of the numerical solution is negative since $\dot{Q}_c^* < \dot{Q}_a$ and \dot{Q}_a was already necessary to cover the lower heat loss of the true system. Since $dT_s/dt = 0$ for the true solution, it is shown that for $T_s^* > T_s$ the true solution is approached and that the system differential equation is stable. A similar argument holds for non constant T_s and for $T_s^* < T_s$.

Hence, the heat loss terms for the collector and storage tank provide the system differential equation's stability. A great heat loss coefficient for collector and storage tank give great stability, i.e. the numerical solution is insensitive to the starting value.

Accuracy

The solar fraction predicted with a simulation method will be subject to an error. It is desirable not only to keep the error small, but also to estimate it. The total error is compounded by a number of errors. These are:

- (1) Errors in the input data (e.g., the meteorological data).

- (2) Errors in the model, the mathematical equations describing the model are only an approximation of the actual physical problem (e.g., the assumption of a fully mixed storage tank).
- (3) Errors in the numerical solution of the problem (e.g., the determination of the storage tank profile). The errors in the numeric solution are:
 - Round off errors incurred by rounding a number on a computer in both storing numbers and performing operations
 - Truncation errors - incurred by using a finite approximation for an essentially infinite process (e.g., using only the first two terms of a Taylor series to predict the storage tank temperature).
- (4) Errors in the evaluation of the solution (e.g., the counting of the relative number of the storage tank temperature data points above T_{min} to obtain the solar fraction).

Errors in the input data: The simulation user cannot completely protect himself against erroneous input data. For example, the uncertainty of hourly average values may be in the order of 5 to 10%. The uncertainty of ground reflectance values may be in the order of several hundred percent, but its effect on the final simulation result may be negligible.

Errors in the model: The errors in the model may be significant, but difficult to assess. For example, the assumption of a fully mixed storage tank, i.e., the neglect of storage tank stratification, typically leads to an under estimation of the predicted performance by 10%.

Errors in the numerical solution: Provided that the numerical solution of the simulation is converging to the true solution and simulation has been given enough time to approach the true solution, round off and truncation errors will always let the numerical solution slightly deviate from the true solution.

Round off errors - the computer representation of a floating point number is

$$n = \pm (a_1 a_2 \dots a_k) 2^q = \pm \left(\frac{a_1 + a_2}{2} + \dots + \frac{a_k}{2^k} \right) 2^q \quad (3.2.8)$$

where the a_i 's are either 0 or 1 with $a_1 = 1$. The number q is the exponent and the number $a_1 a_2 \dots a_k$ is the mantissa of k bits, where k is the precision of the computer.

For an IBM PS/2 80 computer (and most other computers) a real number is stored in 32 bits and the representation is as shown in Figure 3.2.5 (a). Whenever a number in a computer is stored or operated on, a small round off error occurs, as suggested by Figure 3.2.5 (b), due to the finite resolution of the mantissa.

Theoretical relative error bounds for the operations of storing, adding and multiplying numbers can be derived [Frolythe (1977)]. However, it is very difficult to foresee all the number operations for a computer simulation and error bounds sometimes grossly overestimate the actual error. An elegant way of estimating the round off error accurately is to let the simulation run with single and double precision and compare the results. The double precision result can be taken as accurate since its mantissa is represented by 55 bits instead of 23 bits which increases the accuracy by 222. In other words, the double precision result has about 10^9 times smaller round of errors since every extra bit in the mantissa doubles the accuracy! This way, the computer works out its own round off error.

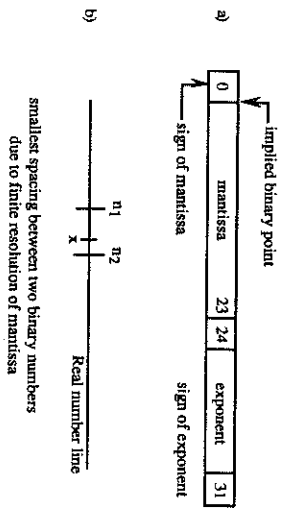


Figure 3.2.5 Computer numbers: (a) number representation; (b) finite resolution.

3.3 Transient Solar Collector Response and its Effect on the Long-Term Average Performance

Solar thermal collectors have a variety of time constants ranging from 10 s to 10 min [Jimenez-Fernandez (1985)]. On the other hand, the time span for a rapid radiation change is in the order of just a few seconds. Hence, for solar thermal collectors, the instantaneous heat output during a rapid radiation change will not correspond to the output calculated with the Hottel-Whillier collector equation, which assumes a zero collector time constant (steady-state). In this section, the effects of the transient response of a solar thermal collector on the long-term average performance are investigated.

The collector time constant, τ , is defined as the time taken for a temperature change of the absorber plate to reach 63.2% ($1 - e^{-1}$) of its steady-state value when the collector is subjected to a step in the solar radiation level. The collector time constant is illustrated in Figure 3.3.1 for a sudden radiation increase.

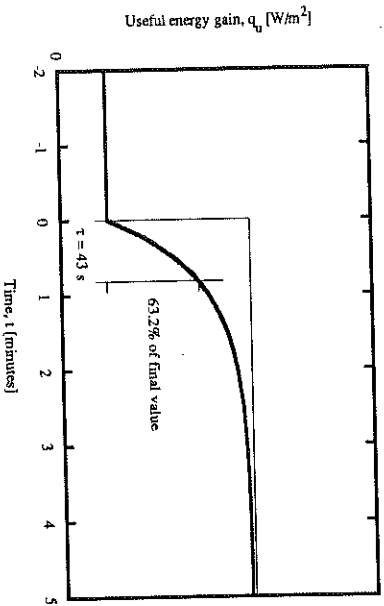


Figure 3.3.1 The definition of the collector time constant.

Saehcke (1987) showed that rapid instantaneous radiation fluctuations are well approximated by step radiation changes. Figure 3.3.2 shows the response of a collector with zero heat capacitance (zero time constant) and a collector with heat capacity resulting in a time constant of 1 minute.

Figure 3.3.2 demonstrates that during the collector heat up period, starting at $t = 0$, the useful energy of the collector with heat capacity is smaller than the useful energy from the collector with zero heat capacity. However, during the cool down period, starting at $t = 10$ minutes, the collector with heat capacity yields a larger useful energy than the one with zero heat capacity.

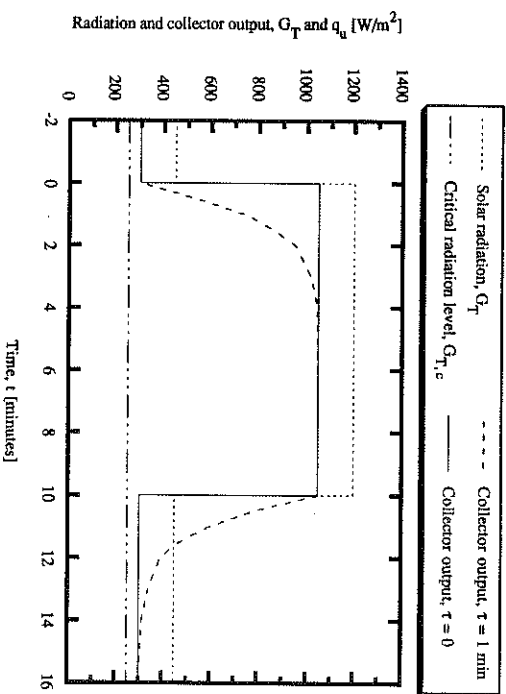
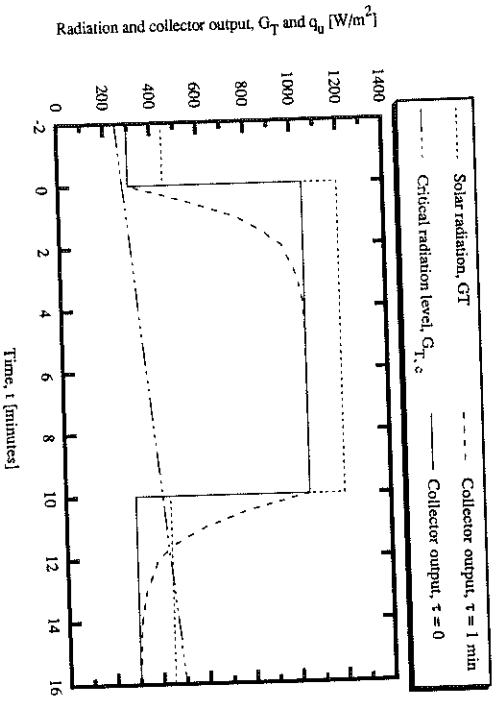


Figure 3.3.2 The collector response for $t = 0$ and $t = 1$ minute for a 10 minutes cloud spacing.

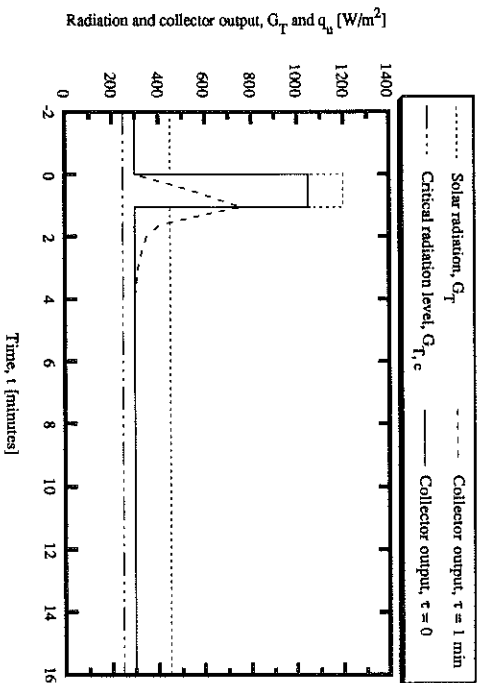
Equation 2.3.5 shows that both the heating and the cooling curve of Figure 3.3.2 are symmetric, so the heat up and cool down periods are equal. In this case the useful energy is not affected by the collector heat capacity.

What was discussed above for a step change is similar for other radiation changes. In average a day must have as many up's and down's in the insulation to go back zero after sunset. This means that for any up there is a corresponding (symmetric) down in the insolation (looking at long periods of time, e.g., a month). Hence for the case studied in Figure 3.3.2, the long-term useful collector output is not affected by heat capacity effects.

However, for a changing critical radiation level or extremely rapid radiation changes heat capacity effects will have a performance reducing effect. This is illustrated with a step radiation change response in Figure 3.3.3.



a)



b)

Figure 3.3.3 Collector performance reduction due to heat capacity effects: (a) Changing critical radiation level; (b) Rapid changing radiation.

From Figure 3.3.3 it is clearly seen that the loss and gain due to heat capacity effects do not equal, so that the collector with non-zero heat capacitance will have a lower output than the collector with zero heat capacity. The case illustrated in Figure 3.3.3 (b) is expected to be more important than the case in Figure 3.3.3 (a).

It has been shown that, even though heat capacity effects may let the actual collector performance deviate from the Hottel-Whillier collector equation, there is a strong tendency of the positive and negative heat capacity effects to cancel. In view of the above case study, the findings of Klein et. al (1974) seem to be essentially correct, i.e., the effects of intermittent radiation should have a small effect on the long-term collector performance. Thus the use of the Hottel-Whillier collector equation is justified and the resulting errors

are said to be minimal. However, that they are always negligible is doubtful. A recent study by Soltau (1987) indicates that for the case of uncovered swimming pool collectors the collector performance is reduced by about 3% due to heat capacity effects.

Heat capacity effects can also affect the collector performance in combination with the control strategy. For a forced collector fluid circulation, heat capacity effects occur under both zero flow and flow conditions. However, useful energy losses due to the control strategy that are partly due to heat capacity effects should be separated from other pure heat capacity effects.

The effect of heat capacity could be studied in general, if more were known about the statistical behavior of instantaneous solar radiation. Areas of interest are the frequency of instantaneous fluctuation changes and the rate of changes.

3.4 Hourly versus Instantaneous Radiation Values and the Effect on the Long-Term Collector Performance

For solar systems without storage short-term fluctuations of the insolation values within an hour have generally no effect on the long-term performance, provided that the load is constant and collector heat capacity effects can be neglected. For solar thermal systems that use the internal energy of large masses of fluids as storage, the radiation fluctuations within an hour have a small effect on the average performance. However, it cannot be shown in general that short-term fluctuations of the insolation values within an hour have a negligible effect on the solar system performance since this depends on the efficiency of the storage.

To illustrate the effect of the radiation fluctuations within an hour, the performance of a solar thermal system of configuration shown in Figure 3.4.1 is investigated over a period of one hour.

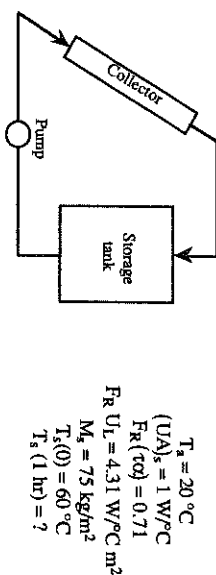


Figure 3.4.1 A basic solar thermal system consisting of a collector and a storage tank.

The solar system in Figure 3.4.1 shall have zero load ($L = 0$) for the hour under consideration. Then, system performance is governed by the differential equation

$$(m c_p)_s \frac{dT_s}{dt} = A_c Fr [(r\alpha)_s G_T(t) - U_L (T_s - T_a)] - (U A)_s (T_s - T_a) - L \quad (3.4.1)$$

which can be rearranged to give

$$\frac{dT_s}{dt} + \frac{A_c Fr U_L + (U A)_s}{(m c_p)_s} T_s = \frac{A_c Fr [(r\alpha)_s G_T(t) - U_L T_a] - (U A)_s T_a - L}{(m c_p)_s} \quad (3.4.2)$$

Using Equation 3.4.2, the solar system performance can be expressed in terms of the storage tank temperature. Figure 3.4.2 (a) to (h) show eight different hourly radiation profiles with the same average radiation. When the solar system shown in Figure 3.4.1 is exposed to the piece-wise constant solar radiation intervals as shown in Figure 3.4.2 (a) to (h), Equation 3.4.2 has the following simple solution

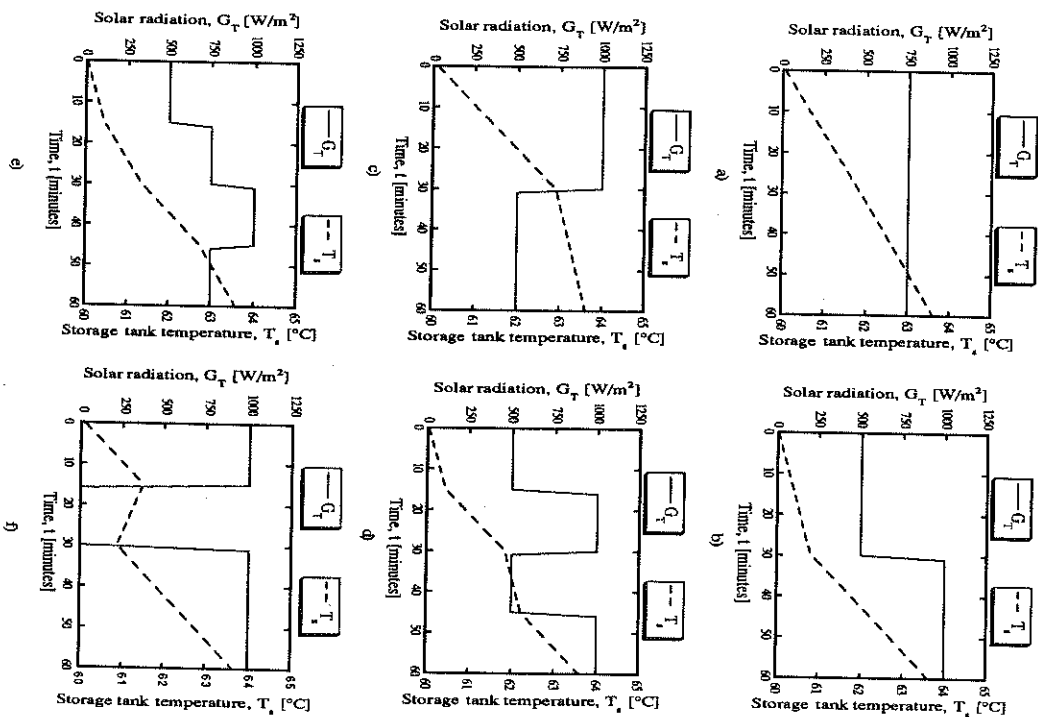
$$T_s(t) = [T_s(0) - T_s^*] e^{-t/\tau} + T_s^* \quad (3.4.3)$$

where $T_s^* = \{A_c Fr \{[\tau\alpha_k Gr(0) + U_L T_a] + (UA)_k T_s - L/M A_c Fr U_L + (UA)_k\}$ is the tank stagnation temperature and $\tau = (m c_p h) / (A_c Fr U_L + (UA)_k)$ is the time constant of the system. Equation 3.4.3 can now be successively evaluated for every time interval of constant radiation, where $T_s(0)$ is the initial storage tank temperature at the beginning of each interval.

The corresponding storage tank temperature profiles are also included in Figure 3.4.2. The storage tank temperature differential between the beginning and end of the hour is taken as a measure of the average hourly system performance. The performance difference between the cases considered in Figure 3.4.2 is at most 2.2% of the tank temperature increase within the hourly interval.

The above examples are indicative for many other types of systems. In particular, it is indicative for systems with constant load since Equation 3.4.3 shows that a load essentially only effects the temperature rise, but not the difference between the cases studied.

The conclusion from this subsection is that solar systems can be highly insensitive to the short-term fluctuations of the radiation values within an hour as long as the average value for the hour is held constant, especially when the long-term performance is sought. Hence, the order of and the fluctuating radiation values within an hourly time interval is generally not important and the actual radiation may be replaced by an average hourly radiation profile.



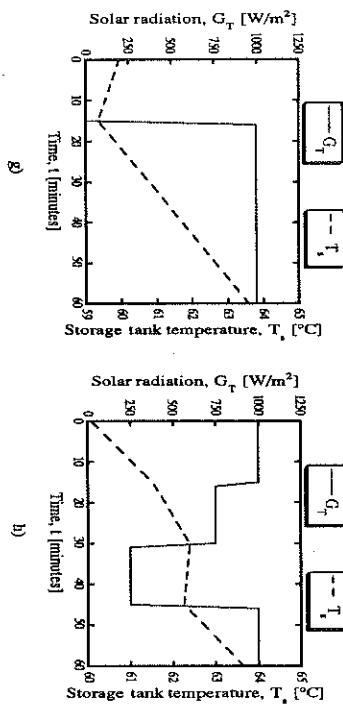


Figure 3.4.2 Eight hourly radiation profiles, and the storage tank temperature response to the radiation profiles.

3.5 Thermal Design Methods Versus Detailed Simulations

In an effort to determine the range and magnitude of accuracy of the f-chart, ϕ -f-chart, and TMD vis-a-vis detailed simulation results a large number of TRNSYS simulations of the system shown in Figure 3.5.1 were compared with the above mentioned design methods for a variety of different loads, collector types, and storage sizes. The standard deviation (SD), which is a measure of the dispersion of the data from the mean value, was calculated and used to quantify the deviation between the predictions.

Table 3.5.1 gives the upper and lower bounds on the system parameters employed. The storage tank was assumed to be fully mixed. Auxiliary tank losses were set to zero for these comparisons. The meteorological data used in the analysis were typical years (TMY) in Madison, USA and Oslo, Norway.

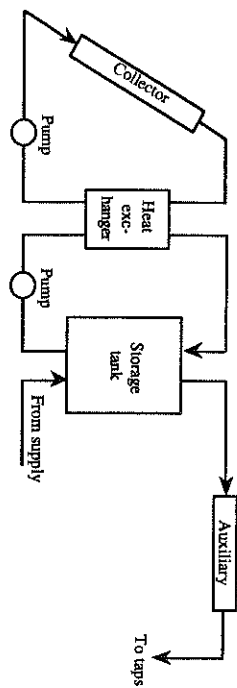


Figure 3.5.1 Schematic of a hot water system.

Table 3.5.1 Range of parameters for TRNSYS and design methods comparisons.

Parameter	Lower bound	Upper bound
Collector:		
A_c [m ²]	5	100
F_r (raz)	0.7	0.85
$F_r U_L$ [W/P/C m ²]	3.0	8.0
Slope	= latitude	= latitude
Storage:		
M_g/A_c [kg/m ²]	50	150
T_{em} [°C]	20	20
Load:		
L [liters/day m ²]	20	500
T_{set} [°C]	30	80

Excellent agreement was found between TRNSYS and the TMD method for the range of parameters given in Table 3.5.1. The total standard deviation for a comparison of monthly solar fractions was equal to 0.014, while the standard deviation for annual results was 0.007. The maximum difference between annual results was 0.02. Very good

agreement was also found between TRNSYS and the ϕ -f-chart method. In this case the total standard deviation for a comparison of monthly solar fractions was equal to 0.034, while the standard deviation for annual results was 0.021. The maximum difference between annual results was 0.06. In contrast, comparisons between the f-chart method with the same simulation results yield monthly and annual standard deviations of 0.055 and 0.045. The maximum difference between annual results was 0.15. Figures 3.5.2, 3.5.3, and 3.5.4 give the annual comparisons between the design methods and TRNSYS.

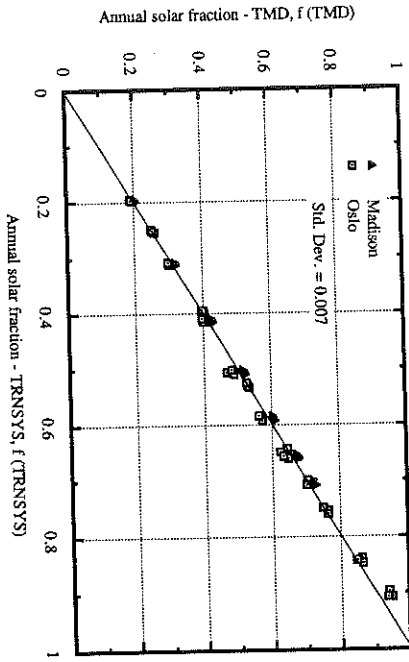


Figure 3.5.2 TMD and TRNSYS comparisons.

These results are not meant to imply that f-chart is not an accurate tool for predicting the performance of water heating systems. The accuracy of this method suffers when applied outside the range of parameters for which it was developed. The ϕ -f-chart and the TMD method, on the other hand, are accurate over a much wider range of system parameters. These methods, however, are more complicated to apply than the f-chart method. When applicable, the f-chart method can still be used to predict the performance of domestic hot water systems.

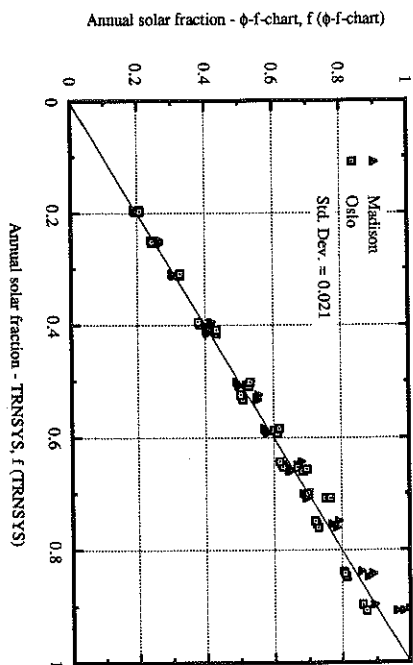


Figure 3.5.3 ϕ -f-chart and TRNSYS comparisons.

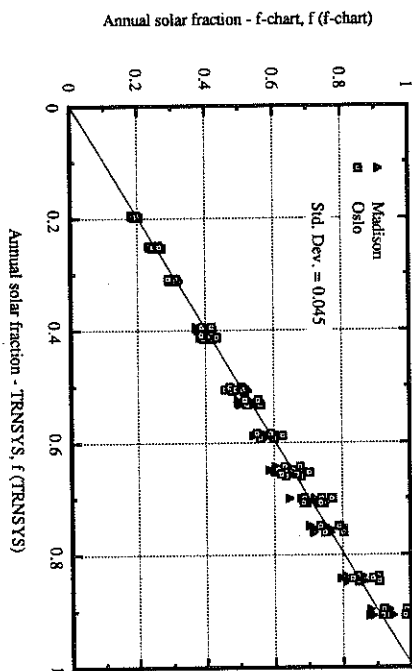


Figure 3.5.4 f-chart and TRNSYS comparisons.

3.6 Storage Tank Stratification

Storage tank stratification, as opposed to a fully mixed storage tank, increases the performance of a solar thermal system. Generally this is explained with a lower collector inlet temperature, resulting in an increased collector output [Reddy (1987)]. However, it will be shown that the increase in the collector performance due to lower collector inlet temperature is only small and cannot be used to explain increases of 10% of the solar fraction due to stratification. In this section it will be shown that the performance increase is mainly due to the load withdrawal from the top of the tank, where the top of the tank is above the average tank temperature.

The storage tank stratification in a DHW system (Figure 3.5.1) is studied numerically. The 3 node storage tank model of Duffie and Beckman (1980) was used to calculate the temperature response within the storage tank. In this context, the numerical stability criteria of Howell et al. (1982) should be mentioned. The maximum step size for the tank node model is

$$\Delta t \leq M_s / (\dot{m} N) \quad (3.6.1)$$

where M_s is the fluid storage mass, \dot{m} the greater flow rate of \dot{m}_c and \dot{m}_h , and N the number of nodes. The criteria ensures that the node temperature is always increasing towards the top of the tank. The chosen time step for the 3 node tank model used in the simulation was 10 minutes, which is well below the maximum step size of 20 minutes calculated from Equation 3.6.1.

Figure 3.6.1 shows a radiation profile for a clear day. Figure 3.6.2 shows the simulated storage tank response of the solar system illustrated in Figure 3.5.1 to the daily radiation profile shown in Figure 3.6.1. In Figure 3.6.2 the effective minimum load supply temperature is represented by a horizontal line (the load controller hysteresis prevents that

T_{on} and T_{off} are equal). It is clearly seen why storage tank stratification "stretches" the load supply duration. The intercept of the storage tank temperature with the T_{min} line determines the load supply duration (solar fraction). If the load is drawn from the top of the tank, the load can be supplied longer, than if, the load would be drawn from the middle of the tank. The (hypothetical) load withdrawal point at the middle of the tank that corresponds to the average tank temperature is the implicitly assumed load withdrawal point when a fully mixed storage model is used.

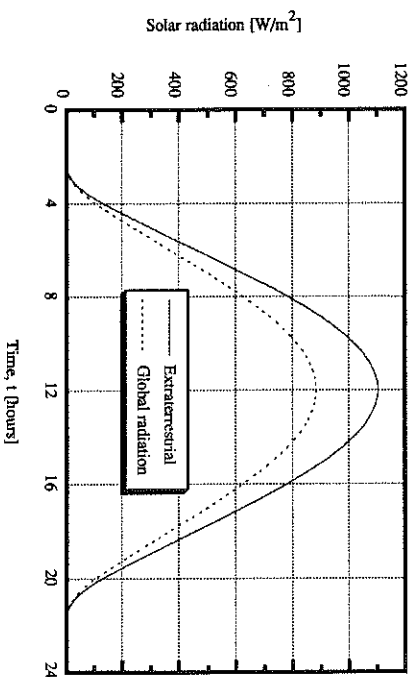


Figure 3.6.1 Hourly radiation profile for a clear day in June (Oslo, 59.9°N). The solid line shows extraterrestrial radiation.

The modeling of storage tank stratification is a very complex problem. The storage tank temperature stratification that can develop in a closed loop system is limited to the maximum temperature difference in either collector or load loop. For the solar system under consideration the maximum temperature difference was about 6°C. However, the

storage tank stratification reached only about 4°C (see Figure 3.6.2). Numerous mechanisms work against the driving collector/load loop temperature difference to destratify the storage tank. They are: mixing of the fluid, conduction within the fluid, tank wall conduction and tank to ambient temperature heat loss. The magnitude of these mechanisms is very much dependent upon the shape of the tank.

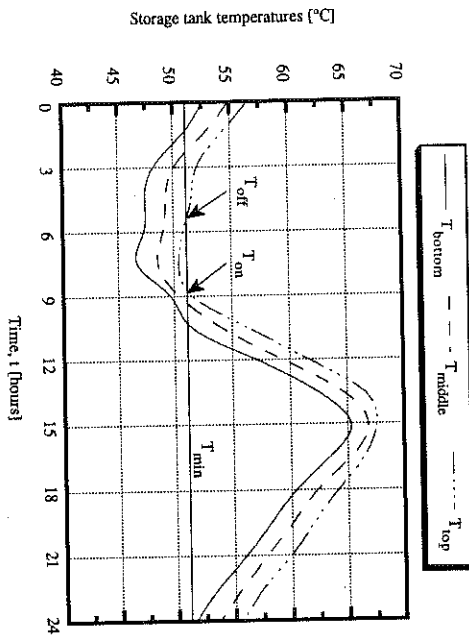


Figure 3.6.2 The variation of the storage tank temperature for the day of Figure 3.6.1.

Although the presented investigation on storage tank stratification is specific to the solar system in Figure 3.5.1, the above results suggest that the performance increasing effect of storage tank stratification on the collector output is small. This is because the effect of the load withdrawal from the top of the tank almost completely already accounts for the increase in solar fraction due to storage tank stratification. In fact, using Equation 2.2.1 with $T_1 = 60^\circ\text{C}$ for the fully mixed tank and $T_1 = 58^\circ\text{C}$ for the stratified tank shows that the collector efficiency changes by only 1% ($\Delta T \rho \lambda = 2^\circ\text{C}$, Figure 3.6.2). In this context,

one may question how a tank can deliver more energy if the collector does not add more energy to the tank. This can be understood from the fact that the load supplied by the system not only depends on the quantity added to the tank, but also depends on the quality of the heat delivered to the load, which is destroyed through mixing. Thus, less mixing (increased stratification) generally increases the load delivery time.

CHAPTER 4

Solar Radiation Models

4.1 Introduction

A crucial input required in the simulation of solar energy systems is hourly radiation incident on the collecting surface. Since solar radiation is the driving force for solar energy systems, accurate hourly radiation values are essential for meaningful simulation results. Incorrect or unrealistic solar radiation data can abrogate proposed solar system designs which result from the simulations. Actual measurements of hourly solar radiation data would be desirable for input but are probably not available for the location and collector orientation under consideration. Accordingly, these data have to be predicted from alternative observations relating more or less explicitly to horizontal surfaces. The objective of this chapter is therefore to evaluate different solar radiation models, and to come up with recommendations for what is the best procedure for determining hourly radiation on a surface of any orientation.

If hourly global horizontal radiation data for the site under consideration is available, two problems exist: first, determining the fraction of the global which is diffuse (or beam); second, estimating the total radiation on a tilted surface of any orientation. Methods for solving these two problems will be evaluated in this chapter. In addition a widely used cloud cover model will also be evaluated.

Comparison of an individual calculated data against a measured or another calculated value is not a sufficient test of accuracy of a predictive model. Rather, it is necessary to analyze

a large body of data. For solar radiation models, the most proper statistical tests are based on calculation of mean bias error (MBE), and root mean square error (RMSE) [Iqbal (1983)]. The problem here is determining what are low values of MBE and RMSE. This problem is resolved by normalizing the MBE and RMSE statistics

$$NMBE = \frac{1}{N} \sum_{i=1}^N (y_i - x_i) / \bar{y} \quad (4.1.1)$$

$$NRMSE = \sqrt{\frac{1}{N} \sum_{i=1}^N (y_i - x_i)^2} / \bar{y} \quad (4.1.2)$$

where y_i is the i th value of the data which are the basis of the comparison (measured or predicted), x_i is the i th predicted value, and \bar{y} is the mean value averaged over N observations.

The NMBE is a measure of a model's long term prediction. The NRMSE indicates the width of the error distribution around the mean and depends on the length of time over which the radiation is integrated, and provides a measure of a model's short term prediction. A solar radiation model with good performance will have a low NRMSE and near zero NMBE.

4.2 Determination of Global Horizontal Radiation

Internationally, hourly global horizontal radiation on a horizontal surface is one of the most widely available measurements in addition to ambient temperature, dew point etc. Lacking measured radiation data for the site under consideration, it is possible to apply empirical correlations to estimate radiation from hours of sunshine or cloudiness.

4.2.1 Global Horizontal Radiation Models

In this work cloudiness models will be studied. The global radiation on a horizontal surface for these models are given by the expression

$$I = I_c \text{ CCF} \quad (4.2.1)$$

where I_c is the clear sky horizontal radiation, and CCF is called the cloud cover factor

SERI (1984) used a 4-year data set from 18 US-stations to evaluate cloud cover models, including the ASHRAE model of Kimura and Stephenson (1969), the MAC model of Davies and Hay (1980), the Cotton (1979) opaque cloud cover regression model, and several modified forms of these cloud cover models. The researchers at SERI found that a modified form of the ASHRAE model, SERI (Bird) model-II [SERI (1984)], gave the most accurate results. The SERI (Bird) model-II uses the Bird clear-sky model [Bird and Hulstrom (1981)], and ASHRAE's cloud cover factor [Kimura and Stephenson (1969)] which is defined by the following equation

$$\text{CCF} = P + S \text{ OPQ} + R \text{ OPQ}^2 \quad (4.2.2)$$

where OPQ is the opaque cloud cover in tenths (0-1). It should be noted that the original values of P, S, and R given by Kimura and Stephenson (1969) have been revised for a much broader data base [SERI (1984)]. The revised monthly values of P, S, and R are given in Table 4.2.1

Table 4.2.1 Coefficients for the SERI (Bird) model-II cloud model for each month.

	Jan	Feb	Mar	Apr	May	Jun	Jul	Aug	Sep	Oct	Nov	Dec
P	1.05	1.05	1.02	1.0	1.0	1.0	1.0	1.0	1.0	1.02	1.04	1.04
S	0.06	0.09	0.12	0.19	0.26	0.33	0.32	0.31	0.30	0.21	0.12	0.03
R	0.82	0.83	0.84	0.91	0.99	1.06	1.07	1.07	1.08	0.99	0.91	0.82

4.2.2 Model Performance

ASHRAE cloud cover factor along with a version of Parmlee clear-sky model [Kimura and Stephenson (1969)] are widely used by the engineering and architectural communities in Norway [Kolsaker et al. (1990), and Harsen and Børresen (1985)]. It is therefore of great importance to assess the variation in predicted global horizontal radiation for the Norwegian climate between the ASHRAE-Parmlee model and the SERI (Bird) model-II. The performance of the ASHRAE-Parmlee model with the new and old values of P, Q, and S along with the SERI (Bird) model-II obtained from comparing measured data at Oslo, Norway (59.9°N) and Bergen, Norway (60.3°N) for 1 year is indicated in Figures 4.2.1 and 4.2.2.

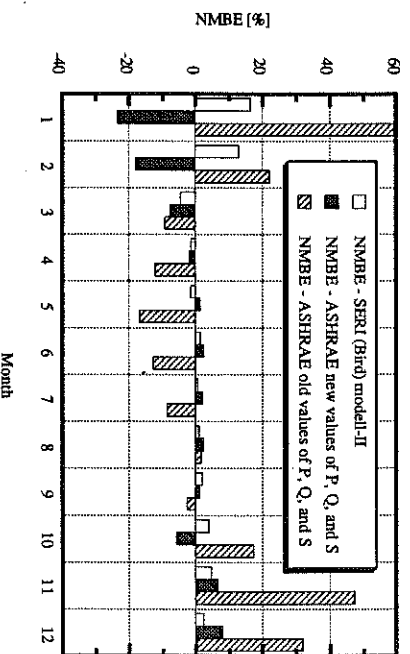


Figure 4.2.1 % NMBE versus month for the SERI (Bird) model-II, and the old and new ASHRAE-Parmlee model.

It is apparent that the values of P, Q, and S in Equation 4.2.2 have a significant influence on the estimated global radiation. This study showed that estimates based on the old values of P, Q, and S gave unrealistically high values of the hourly global radiation in the summer months for both Oslo and Bergen. The new P, Q, and S values should therefore be preferred over the old values.

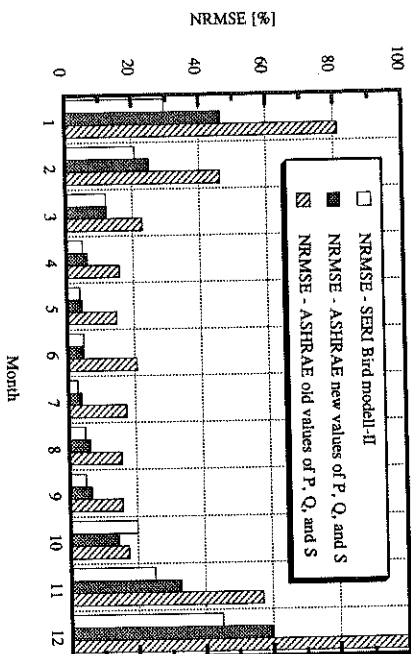


Figure 4.2.2 % NRMSE versus month for the SERI (Bird) model-II, and the old and new ASHRAE-Parmiee model.

The influence of clear-sky radiation models on the predicted global radiation is much less than the values of P, Q, and S in Equation 4.2.2. However, the Bird clear-sky model should be preferred over the ASHRAE-Parmiee procedure. Even though the SERI (Bird) model-II is considered to represent the state-of-the-art on this subject, it is highly recommended only to use the model in the absence of data on measured horizontal global radiation. This is due to the fact that the cloud cover data are based on visual estimates, and therefore less reliable.

4.3 Horizontal Diffuse Radiation

Diffuse fraction correlations were presented in Section 2.3.1. An obvious question at this point is, which of the diffuse fraction correlations should be used? In an effort to provide a simple comparison between the different correlations in which seasonal and location effects can be assessed, RMSE values based on I_d/I are calculated. The inputs to the analyses were measured hourly values of global horizontal radiation, ambient temperature, and relative humidity at three locations: Oslo, Norway (59.9°N), Hamburg, Germany (53.6°N) and Cape Canaveral-Florida, USA (28°N).

4.3.1 Model Performance

The yearly RMSE values in Figure 4.3.1 suggest some location effects. On an overall basis the correlations perform better at Oslo and Hamburg than at Cape Canaveral. This is most likely a coincidence, and may change from year to year.

Generally Reindl et al. correlation shows the best performance, while Lie and Jordan model exhibits the poorest performance. It is clearly seen that Skarveti and Olseth model is very location dependent. The model performs very well at Oslo and Hamburg, but the RMSE value increases a lot more than the other models at Cape Canaveral. This is natural considering that the correlation is based on data from only one location. Also, RMSE values are higher in the fall and winter months than on an annual basis. The influence of diffuse radiation on the predicted total radiation on tilted surfaces is investigated in Section 4.4.1.

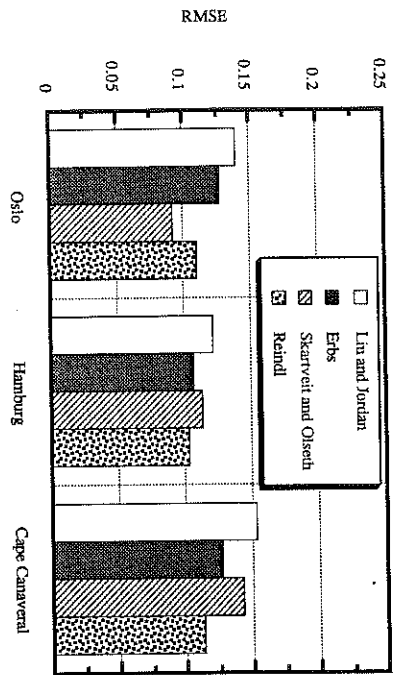


Figure 4.3.1. Annual RMSE values for Oslo, Hamburg, and Cape Canaveral.

4.4 Sky Diffuse Radiation

A new tilted surface model has been developed. The Skarveit and Oiseith model does not account for horizon brightening diffuse radiation. Preliminary calculations of diffuse radiation incident on south facing surfaces indicated that the Skarveit and Oiseith model underpredicted the tilted surface diffuse radiation. The Skarveit and Oiseith model may be improved by addition of a horizon brightening term. In their study of clear sky radiance distributions Temps and Coulson (1977) approximated the horizon brightening effects by applying a correction factor of $[1 + \sin^3(\beta/2)]$ to the isotropic diffuse radiation. The correction factor pertained to clear sky conditions only. Klucher (1979) modified the Temps and Coulson clear sky model by imposing a modulating factor, $F = 1 - (I_p/I)^2$ on the sine term. The Klucher form of the correction factor is $[1 + F \sin^3(\beta/2)]$. The horizon

brightening correction factor first introduced by Temps and Coulson and later modified by Klucher was applied to the isotropic term in the Oiseith and Skarveit model. A similar inclusion of the horizon brightening term was performed by Reinnd (1988) to the Hay and Davis model. The new anisotropic model becomes

$$I_{dr} = I_d \left[r_b R_b + Z_c \cos \beta + (1 - r_b - Z_c) \left(\frac{1 + \cos \beta}{2} (1 + F \sin^3(\beta/2)) \right) \right] \quad (4.4.1)$$

The first term represents the contribution of circumsolar diffuse radiation. The second term expresses the zenith brightening diffuse radiation, and the third term represents the isotropic diffuse radiation corrected to include horizon brightening diffuse radiation.

4.4.1 Model Performance

To establish the superiority of one model over the other it is of course preferable and to some extent necessary to have measurements of the total radiation for the inclined surface under consideration. Due to the lack of hourly measurements, a different approach had to be applied in order to assess the tilted surface model performance. Two independent studies involving several US-stations [Hulstrom (1989) and Perez et al. (1990)] showed that the Perez model was the most accurate of all the algorithms under consideration. Their evaluation covered the isotropic, Temps and Coulson, Hay and Davies, Klucher, and Perez models.

The Perez model was therefore used as a basis for model comparison for Oslo, Trondheim, Madison and Miami. The inputs to the tilted surface models were measured values of global horizontal radiation, and Erbs correlation was used to estimate horizontal diffuse radiation. Table 4.4.1 shows the surface slopes and orientations used in forming the NMBE and NRMSE statistics.

Table 4.4.1 Tilted surface model parameters.

Slope	Azimuth
30°	south
45°	south
60°	south
90°	south, west, north, east

The resulting NMBE and NRMSE statistics for each model for all surface orientations are graphically presented in Figure 4.4.1. The NRMSE results indicate that the anisotropic models (Skarveit and Olseth, Hay and Davies, and new model) show similar performance but the isotropic model exhibits much larger differences. The NMBE results show that the isotropic, Skarveit and Olseth, Hay and Davies, and new model are underpredicting the solar radiation on an overall basis.

In the northern hemisphere, most collecting devices for solar energy systems are oriented south facing. It is useful to observe the model's performance when applied only to south facing surface orientations. The NMBE and NRMSE statistics were calculated using the south facing surface orientations indicated in Table 4.4.1. The results are shown in Figure 4.4.2. On an overall basis, the NRMSE was reduced by about 2% for each model. The NMBE revealed an interesting result. When compared to the results in Figure 4.4.1 (all surface orientations), the NMBE for the all models increased. This indicates that all models overpredict the solar radiation for non-south surface orientations when compared to their performance for south facing surfaces.

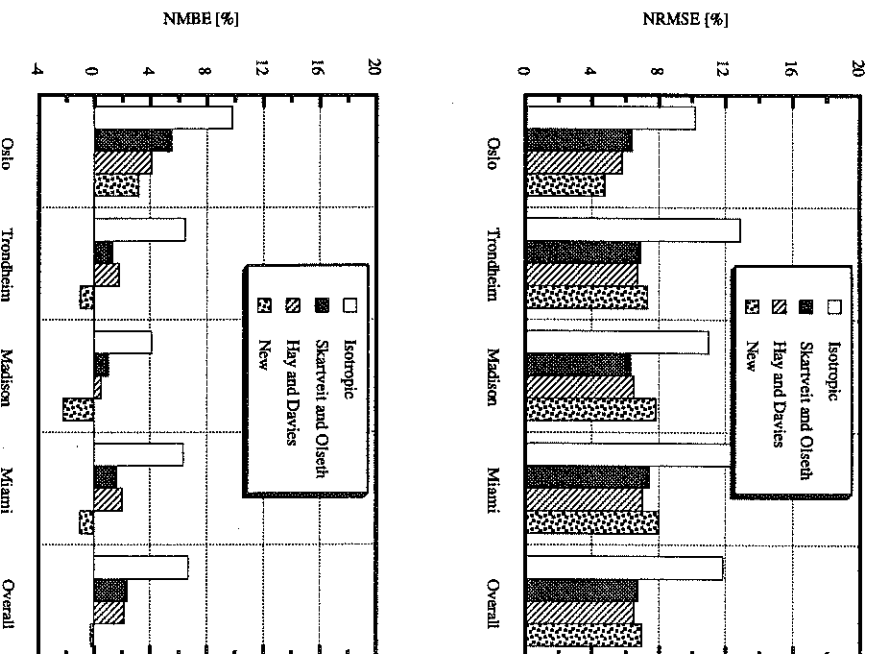


Figure 4.4.1 Normalized RMSE and normalized MBE for all surface orientations.

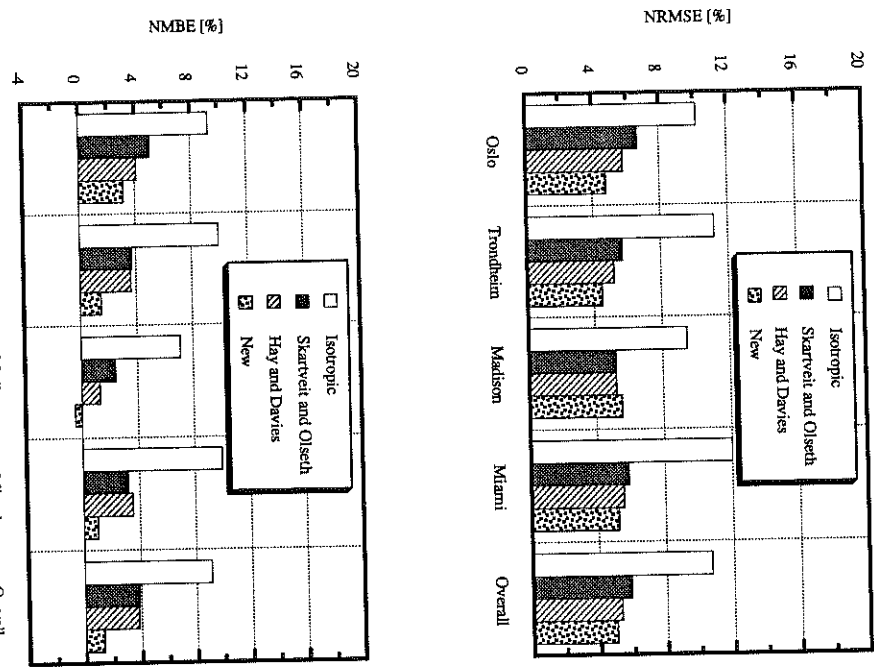


Figure 4.4.2 Normalized RMSE and normalized MBE for south facing surface orientations.

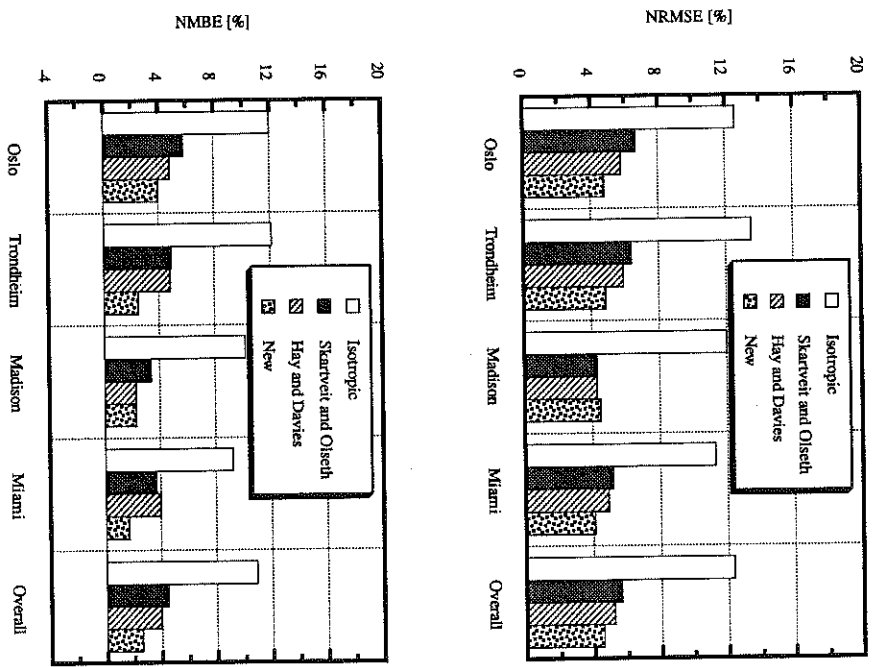


Figure 4.4.3 Normalized RMSE and normalized MBE for south facing surface orientations using Reinold's correlation to estimate horizontal diffuse radiation.

It is clear that the isotropic model showed the poorest performance and should not be used for estimating the hourly diffuse radiation on a tilted surface. The anisotropic models all showed comparable performance. The choice of the "best" model is influenced by the limitations and complexity of the individual model. The Skarveit and Oisech, Hay and Davies and new model are much simpler to use when compared to the Perez model, and would be useful in performing computations with a hand-held calculator. The complexity of the Perez model should not be a problem in computer-aided calculations.

The effects of using different diffuse fraction correlation on the resulting solar radiation predicted by each tilted surface model was explored by using Reinold's model to estimate the diffuse radiation on a horizontal surface. The results of the NRMSE and NMBE statistics for south facing orientations are shown in Figure 4.4.3. Interestingly, as implied by the magnitude of the NRMSE and NMBE statistics, the results are not greatly influenced by the use of a different diffuse fraction correlation to estimate the diffuse fraction on a horizontal surface. Similar results were obtained by using Skarveit and Oisech's diffuse fraction correlation to estimate the diffuse radiation on a horizontal surface.

4.5 Closing Remarks

Modified methods for determining the transmittance-absorptance product ($\tau\alpha$) of a glazing system are required when using anisotropic models. For the anisotropic models the circum-solar diffuse and isotropic diffuse should be treated separately [Nordgaard et al.(1989)]. The $(\tau\alpha)$ -product for circum-solar radiation should be calculated as beam radiation (i.e. effective angle of incidence is the angle of incidence of beam radiation). The effective angle of incidence for isotropic sky diffuse radiation, as reported in Duffie

and Beckman (1980), varies as a function of surface slope from approximately 57-60°. The author recommends lumping the remaining diffuse sky radiation components at an effective angle of 58° for purposes of calculating $(\tau\alpha)$. The effective incidence angles for anisotropic radiation models varies between 54° - 56° on clear skies up to 60° on an overcast day.

The final recommendations are summarized below.

- 1) For estimating global radiation on horizontal surfaces with cloudiness models:
Revised P, Q, and S values - Table 4.2.1
- 2) For estimating horizontal diffuse radiation:
Reinold et al.'s correlation - Equations 2.3.11 - 2.3.13
- 3) For estimating diffuse radiation on tilted surfaces:
New model - Equation 4.4.1
- 4) Effective angle for transmittance-absorptance product:
Circum-solar diffuse radiation - $\theta_e = \theta$
Other diffuse sky radiation components - $\theta_e = 58^\circ$.

Modelling of Flat-Plate Collectors Based on Monolithic Silica Aerogel

5.1 Introduction

It has recently been experimentally shown [Svendsen et al. (1987) and (1989)] that the flat-plate collector efficiency can be significantly improved by filling the air gap between absorber and cover with monolithic silica aerogel (MSA), and evacuating the system to 0.1 bar. The most recent collector design proposed by Svendsen is illustrated in Figure 5.1.1. In this construction the bottom and edge insulation material have been substituted with MSA.

The collector consists of a plane, black painted absorber made from copper tubes with copper foils on each side. The copper foils are supported by means of blocks of suitable material. Both sides and the edges of the absorber are covered by 20 mm thick MSA tiles and 4 mm low iron, tempered glass. A frame of stainless steel placed between the glass is sealed with butyl to make the collector box airtight.

The objective of this chapter is to model MSA collectors and introduce the necessary quantities that enables MSA collectors to be treated as ordinary flat-plate collectors. At the end of this chapter the MSA collector will be compared against flat-plate collectors based on other TTMs, selective coatings, and an evacuated collector.

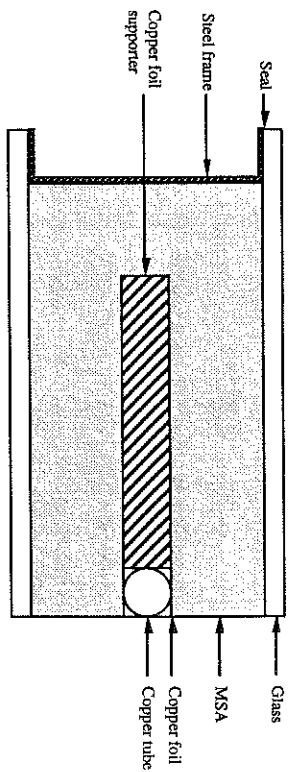


Figure 5.1.1. Cross section of a MSA flat-plate solar collector. Adapted from Svendsen (1989).

5.2 Attenuation of Solar Radiation in MSA

When solar radiation enters the MSA slab, a fraction of the incident energy is transmitted through the material without being attenuated (direct-direct transmittance), and a part is removed by scattering and another by absorption. A portion of the scattered radiation is backscattered and a portion is transmitted through the slab (direct-diffuse transmittance). No correction for surface reflections will be required in the analyses that follows because the index of refraction of MSA is close to unity, between 1.01 and 1.05 depending on density [Henning and Svensson (1981)]. The attenuation in MSA is illustrated in Figure 5.2.1.

The monochromatic direct-direct transmittance is defined by Bouguer's law

$$T_{\text{dir-dir},\lambda} = \exp \left[- \frac{(K_{a,\lambda} + K_{s,\lambda})L}{\cos \theta} \right] \quad (5.2.1)$$

where $K_{a,\lambda}$ = the absorption coefficient [1/m]

$K_{s,\lambda}$ = the scattering coefficient [1/m]

L = the slab thickness [m]

θ = the angle of incidence [°]

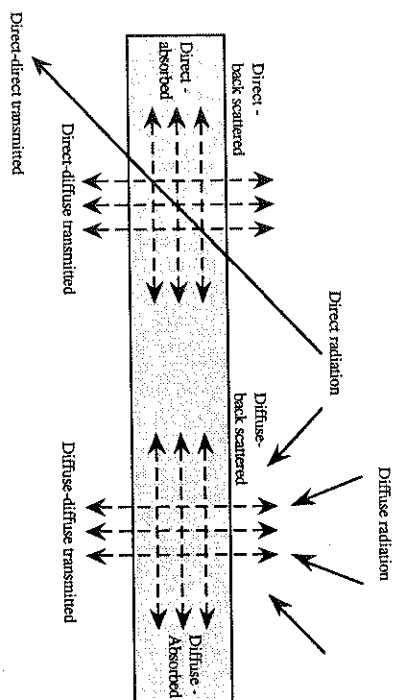


Figure 5.2.1. Distribution of direct, scattered, and absorbed solar radiation in MSA.

The spectral direct-diffuse transmittance, $\tau_{dir-dif,\lambda}$, is given by the multiple scattering within MSA. Analysis of multiple scattering is usually mathematically very complex and require a great deal of computational effort. However, a new and fast method for isotropic multiple scattering within an absorbing and scattering medium is presented in Section 5.2.2.

5.2.1 Optical Transmission Studies in MSA

Figure 5.2.2 shows measured spectral transmittance of a 12 mm thick MSA (TEOS) sample [Tewari et al.(1986)]. A more transparent MSA (TMOS) has been reported by Svendsen (1989). The total transmittance at normal incidence for TMOS has been measured to 0.9 for a 20 mm thick sample, which is 4% higher than an equally thick TEOS sample. However, spectral transmittance values for TMOS has not yet been reported, and the TEOS data shown in Figure 5.2.2 will therefore be used in this study.

Figure 5.2.2 illustrates that the transmittance increases rapidly with wavelength in the visible and generally decreases in the near infrared, exhibiting a number of absorption bands. Silica absorbs only slightly in the visible and near ultraviolet, so most of the attenuation of the radiation results from scattering. The absorption bands near 1.4 and 1.9 μm are also seen in water, and the 2.2 and 2.6 μm bands have been identified as combinations of O-H and Si-O fundamentals [Rubin and Lampert (1983)].

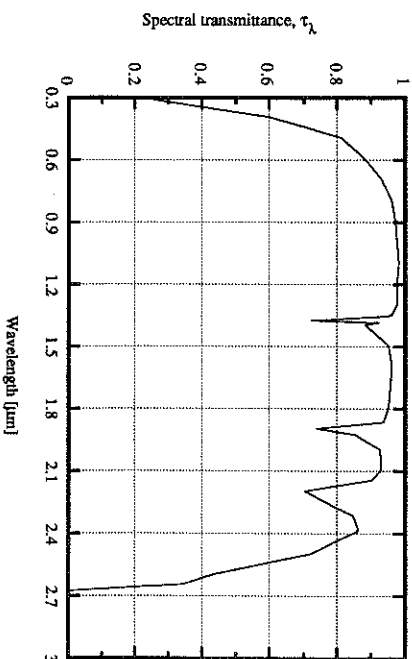


Figure 5.2.2. Transmission spectrum of TEOS-MSA 12 mm thick. Supercritically dried by CO_2 , but not heated to remove all adsorbed H_2O . Data from [Tewari et al.(1986)].

An isolated spherical particle shows Rayleigh scattering if its diameter, D , is much less than λ_0/n , where λ_0 is the vacuum wavelength of incident and scattered light and n is the index of refraction of the particle. The size of the individual silica particles easily satisfies the criterion for Rayleigh scattering in the visible part of the spectrum (0.4 - 0.8 μm).

However, MSA is to densely packed to behave as a collection of independent particles, and several authors [Rubin and Lampert (1983), and Tewari et al. (1986)] have attributed the primary cause of scattering in MSA to inhomogeneities in the average density such as should be described by dependant scattering theories, e.g. Rayleigh-Debye. Nevertheless, the same authors have assumed independent Rayleigh scattering, and derived a characteristic size for the scatteres by fitting the measured transmittance values. In the following the applicability of independent Rayleigh scattering will be tested.

For Rayleigh scattering, the scattered energy in any direction is proportional to the inverse fourth power of the wavelength of the incident radiation. The spectral transmittance for Rayleigh scattering can therefore be written as

$$\tau_{R,\lambda} = \exp\left(-\frac{C}{\lambda^4}\right) \quad (5.2.2)$$

where λ is the wavelength of incident and scattered radiation, and C is an unknown function of the refractive index, the particle size, and volume fraction of MSA. The rising part of the curve in Figure 5.2.2 between 0.3 and 0.8 μm was compared to the inverse fourth-power law of Rayleigh scattering. In Figure 5.2.3 the logarithmic values of the measured transmittance (0.3 - 0.8 μm) has been plotted against $(1/\lambda^4)$. The agreement between the scattering in MSA and Rayleigh scattering is seen to be very good, and a curve fit of the data to Equation 5.2.2 gave a correlation coefficient of 0.999. Thus, even though the particle size distribution is not well known, one knows that the scattering is Rayleigh.

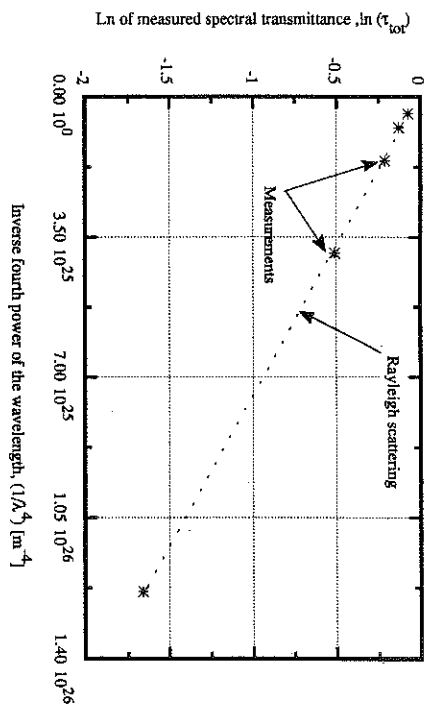


Figure 5.2.3 Comparison of actual scattering in MSA with the $1/\lambda^4$ variation.

The optical properties may be found by solving the equation of transfer for Rayleigh scattering. The spectral extinction coefficients are needed as input to this calculation. According to Siegel and Howell (1982) the equation of transfer in scattering, absorbing, and emitting media can be written as

$$\frac{dI_{\lambda}(s)}{ds} = -K_{a,\lambda} i_{\lambda}(s) + K_{s,\lambda} i_{\lambda} \int_{\omega} T(s) - K_{s,\lambda} h_{\lambda}(s) + \frac{K_{e,\lambda}}{4\pi} \int_{\omega} i_{\lambda}(s) \Phi(\omega_s \rightarrow \omega) d\omega_s \quad (5.2.3)$$

where $K_{a,\lambda}$ = the absorption coefficient [1/m]

$K_{s,\lambda}$ = the scattering coefficient [1/m]

i_{λ} = the directional monochromatic radiation intensity

h_{λ} = the monochromatic intensity of emitted energy of the particles from

Planck's distribution

s = the distance traveled in the medium

T = the particle temperature [°C]

ω = the solid angle

Φ = the phase function. For Rayleigh scattering $\Phi = 3/4(1 + \cos^2\varphi)$ where φ is the angle between the incident and scattered radiation.
 i denotes direction

The first term represents losses by absorption and scattering, and the second term describes the gain by emission. The last term represents the gain by scattering from other directions. Equation 5.2.3 is a so called integro-differential equation, and with an anisotropic phase function its solution is very complicated and time consuming. By introducing the optical thickness, $K_{D,\lambda}$, and the albedo for scattering, Ω_λ ,

$$K_{D,\lambda} = (K_{a,\lambda} + K_{s,\lambda})s \quad \Omega_\lambda = \frac{K_{s,\lambda}}{K_{s,\lambda} + K_{a,\lambda}} \quad (5.2.4)$$

and neglecting the emission term Equation 5.2.3 can be written in the following form,

$$\frac{dI_\lambda(K_{D,\lambda})}{dK_{D,\lambda}} = -i_\lambda(K_{D,\lambda}) + \frac{\Omega_\lambda}{4\pi} \int_{4\pi} i_\lambda(K_{D,\lambda}) \Phi(\omega_i \rightarrow \omega) d\omega_i \quad (5.2.5)$$

However, the importance of anisotropy (phase functions not equal to 1) has been investigated by several authors, e.g. Evans et al. (1965) who calculated the reflectance and transmittance of slabs for different phase functions, albedos, and optical thicknesses. Evans found that the results for isotropic scattering ($\Phi = 1$) and Rayleigh scattering were nearly identical except at large optical scattering. Evans results are illustrated in Figure 5.2.4.

The optical thickness in MSA is largest in the near ultraviolet region. For a 20 mm thick MSA tile, when the albedo for scattering approaches one, the optical thickness at 0.3 μm will be ~ 1.7 . Based on Evans results the scattering in MSA may be assumed isotropic, as long as the tile thickness is less than 50 mm.

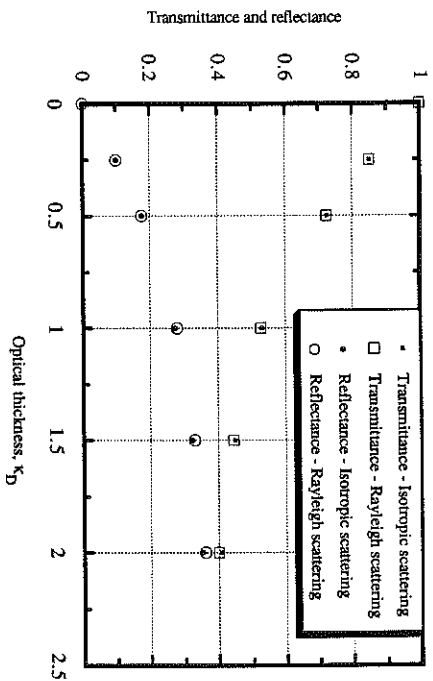


Figure 5.2.4 Calculated transmittance and reflectance. Effect of optical thickness on reflectance and total transmittance for isotropic and Rayleigh scattering. Data from Evans et al. (1965).

5.2.2 Radiative Transfer in an Absorbing-Scattering Medium

This section presents a new method for predicting the radiative transfer in an absorbing and isotropically scattering plane-parallel atmosphere. The technique is based upon the \hat{F} ("F-hat") concept [Beckman (1971)], and it was developed in order to determine the radiative heat transfer at short wavelengths for MSA.

Consider a 1-dimensional plane parallel system of optical thickness K_D divided into n equal elements each of optical thickness Δx , with $n+1$ surfaces as shown in Figure 5.2.5. Solar radiation, is incident on surface 1 and short wavelength radiation, i.e. I, is transmitted through the medium while being attenuated by isotropic scattering and absorption along the path. The temperature within the medium is assumed to be low enough to suppress short wavelength emission.

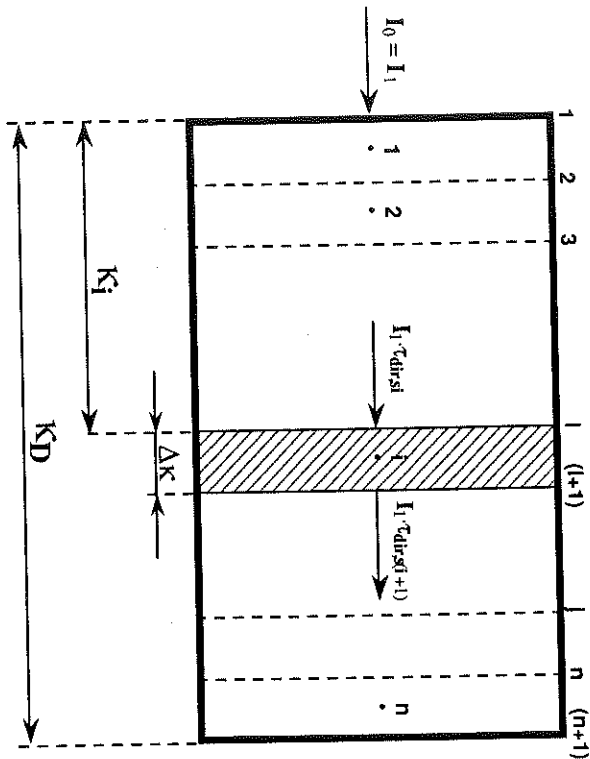


Figure 5.2.5 Geometry of plane-parallel system.

The factor, $F_{vi,sj}$ is defined as the fraction of the energy isotropically leaving element i that directly impinges on surface j , that is, without being scattered or absorbed along the way. The factors $F_{vi,sj}$ can be expressed in terms of the third exponential integral, $E_3(x)$ (see Hottel and Sarofim (1967) for definition of the exponential integral).

$$F_{vi,sj} = 2[E_3(k_j - k_i + 1) - E_3(k_j - k_i)]/4\Delta K \quad \text{for } j \neq i+1, i \quad (5.2.6)$$

$$F_{vi,sj} = [1 - 2E_3(\Delta k)]/4\Delta K \quad \text{for } j = i, i+1 \quad (5.2.7)$$

The factor, $F_{vi,j}$ is defined as the fraction of energy first scattered in element i that is attenuated in element j . The $F_{vi,j}$ factors are calculated by Equations 5.2.8 and 5.2.9.

$$F_{vi,j} = |(F_{vi,si} - F_{vi,s(i+1)})| \quad \text{for } i \neq j \quad (5.2.8)$$

$$F_{vi,j} = 1 - F_{vi,s(i+1)} - F_{vi,si} \quad \text{for } i = j \quad (5.2.9)$$

A related factor, $\hat{F}_{vi,sj}$ is defined as the energy isotropically leaving element i that strikes surface j by all possible paths divided by the energy isotropically leaving element i . The paths include the "direct" component expressed by $F_{vi,sj}$ as well as all possible paths by which radiation first scattered in element i reaches element k , is scattered in k and then strikes surface j . The $\hat{F}_{vi,sj}$ values depend upon the $F_{vi,si}$ factors and albedos for scattering, Ω_i , the ratio of scattered radiation to scattered plus absorbed radiation. For a homogeneous system the Ω_i values are identical. A general expression for $\hat{F}_{vi,sj}$ for a system divided into n elements is given by *

$$\hat{F}_{vi,sj} = F_{vi,sj} + \sum_{k=1}^n (\Omega_k F_{vi,sk} \hat{F}_{vk,sj}) \quad (5.2.10)$$

An expression similar to Equation 5.2.10 can be written for every combination of elements and surfaces. The total set of equations for the \hat{F} factors of n elements and $n+1$ surfaces results in a set of $n \cdot (n+1)$ linear equations with $n \cdot (n+1)$ unknowns. Given the $F_{vi,sj}$ factors and each element's albedo for scattering, the unknown \hat{F} values can be found by solving the following matrix equation

$$\hat{F} = A^{-1} \times F \quad (5.2.11)$$

where \hat{F} is the ensuing $n \cdot (n+1)$ matrix of values

$$\hat{F} = \begin{bmatrix} \hat{F}_{v1,s1} & \hat{F}_{v1,s2} & \dots & \hat{F}_{v1,sn} & \hat{F}_{v1,s(n+1)} \\ \hat{F}_{v2,s1} & \hat{F}_{v2,s2} & \dots & \hat{F}_{v2,sn} & \hat{F}_{v2,s(n+1)} \\ \dots & \dots & \dots & \dots & \dots \\ \hat{F}_{vn,s1} & \hat{F}_{vn,s2} & \dots & \hat{F}_{vn,sn} & \hat{F}_{vn,s(n+1)} \end{bmatrix} \quad (5.2.12)$$

A⁻¹ is the inverse of the scattering matrix, A, defined by

$$A = \begin{bmatrix} 1 - \Omega_1 F_{v1,v1} & -\Omega_2 F_{v1,v2} & \dots & -\Omega_n F_{v1,vn} \\ -\Omega_1 F_{v2,v1} & 1 - \Omega_2 F_{v2,v2} & \dots & -\Omega_n F_{v2,vn} \\ \dots & \dots & \dots & \dots \\ -\Omega_1 F_{vn,v1} & -\Omega_2 F_{vn,v2} & \dots & 1 - \Omega_n F_{vn,vn} \end{bmatrix} \quad (5.2.13)$$

and F is the matrix given by

$$F = \begin{bmatrix} F_{v1,s1} & F_{v1,s2} & \dots & F_{v1,sn} & F_{v1,s(n+1)} \\ F_{v2,s1} & F_{v2,s2} & \dots & F_{v2,sn} & F_{v2,s(n+1)} \\ \dots & \dots & \dots & \dots & \dots \\ F_{vn,s1} & F_{vn,s2} & \dots & F_{vn,sn} & F_{vn,s(n+1)} \end{bmatrix} \quad (5.2.14)$$

After evaluating the \hat{F} factors, the resulting reflectance and transmittance of the slab can be calculated by

$$\rho = \sum_{k=1}^n (\hat{F}_{vk,sl} \Omega_k I_{att,vk}) / I_0 \quad (5.2.15)$$

$$\tau = \tau_{dir-dir} + \sum_{k=1}^n (\hat{F}_{k,s(n+1)} \Omega_k I_{att,vk}) / I_0 \quad (5.2.16)$$

where $I_{att,vi}$ is the attenuated energy in element i, and is equal to the decrease in the primary-beam intensity in element i

$$I_{att,vi} = I_i - I_{i+1} = I_i \cdot [\tau_{dir-dir,si} - \tau_{dir-dir,s(i+1)}] \quad (5.2.17)$$

where $\tau_{dir-dir,si}$ is the direct transmittance given by Equation 5.2.1, and θ is the incidence angle of the primary beam. Equations 5.2.15 and 5.2.16 can also be used to determine the absorption, α , within the slab, by applying the following relationship:

$$\alpha = 1 - \tau - \rho \quad (5.2.18)$$

The number of elements needed to adequately represent the radiative transfer in the 1-dimensional plane-parallel slab has been investigated by comparing the transmittance predicted by the \hat{F} -method with those of the discrete ordinate method, DOM [Siegel and Howell (1982)].

Two elements are required to obtain a maximum relative error of 1%, with respect to the DOM solution, for K_D less than 0.5. At K_D equal to 1, and 2, the required number of elements have increased to 4, and 10, respectively. In Figure 5.2.6 the calculated transmittance and reflectance obtained using the \hat{F} -method are compared to single scatter calculations and DOM transmittance and reflectance values. In this figure K_D is varied from 0 to 5 while Ω_1 and θ are fixed at 0.9 and 0.0, respectively. Similar agreements between the \hat{F} -method and the DOM solution were obtained for all values of Ω_1 and θ .

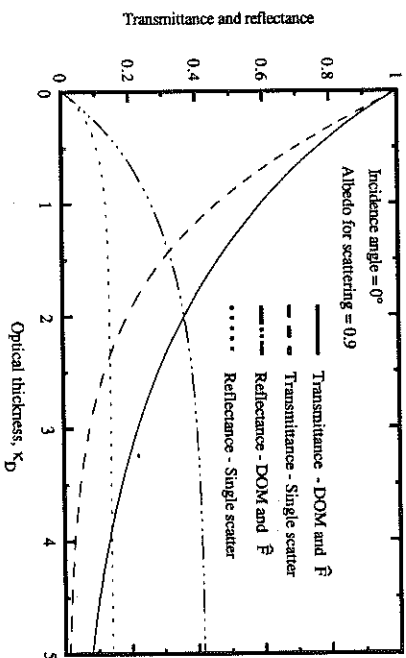


Figure 5.2.6 Transmittance and reflectance values. Comparison of the \hat{F} -method with the DOM. Predictions by the single scatter method [Hofiel and Sarofim (1967)] are also included.

Closing Remarks

So far only gray media have been considered. However, the extension of the \hat{F} -method to non-gray media is easy. The monochromatic angular transmittance, $\tau_{\lambda}(\theta)$, and reflectance, $\rho_{\lambda}(\theta)$, values can be calculated in the usual way, with κ replaced by κ_{λ} and Ω by Ω_{λ} . The total values are then obtained by integration over the solar spectrum (0.3 - 3 μm) for each incidence angle.

A major advantage of the \hat{F} -method compared to similar techniques, for instance the Zone method [Hottel and Sarofim (1967)], is that the \hat{F} 's are independent of the thermal boundary conditions (assuming that the material properties are independent of changes in the boundary conditions). The importance of this advantage is really obvious for angular calculations, where the \hat{F} 's only need to be evaluated once even though the source function, I_{int} , changes.

5.2.3 Spectral Dependence of Transmittance

The measured transmittance values shown in Figure 5.2.2 have been analyzed with the \hat{F} -method presented in Section 5.2.2, and spectral absorption- and scattering coefficients have been evaluated. The following procedure was applied: Knowing silica hardly absorbs between 0.5 and 0.7 μm [Fricke (1986)], the \hat{F} -method was used to predict the scattering coefficients assuming no absorption occurred in this wavelength interval. An effective size for the scatterers was derived by fitting these scattering coefficients to the following expression for independent Rayleigh scattering

$$K_{s,\lambda} = (1 - \epsilon) \frac{4D^3 \epsilon^2 \pi^4}{\lambda^4} \left(\frac{n^2 - 1}{n^2 + 2} \right)^2 \quad (5.2.19)$$

Multiple scattering in optically thick samples will alter the angular distribution of scattered light which the derivation of Equation 5.2.19 was based upon. However, if little

scattered light re-enters the beam Equation 5.2.19 will still give the correct result for the scattering coefficient. The validity of Equation 5.2.19 for MSA was verified in Section 5.2.1 where the scattering was shown to obey the inverse fourth-power law of independent Rayleigh scattering.

The effective particle size derived from curve fitting based on the index of refraction of silica was 7.5 nm. From their micrographs Tewari et al. (1986) obtained a mean particle diameter of 4 nm. This discrepancy may be explained by groups of particles behaving as a single scattering unit.

After predicting the effective particle diameter, Equation 5.2.19 was used to calculate the spectral scattering coefficients, and combined with the measured transmittance values shown in Figure 5.2.2 the \hat{F} -method was used to estimate the spectral absorption coefficients. The resulting extinction coefficients are shown in Figure 5.2.7.

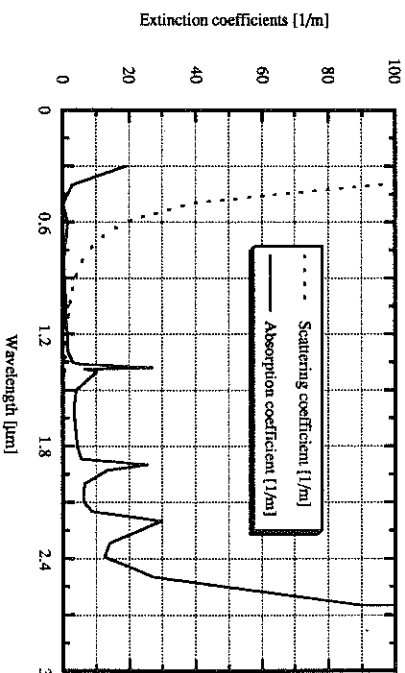


Figure 5.2.7 Spectral scattering and absorption coefficients for MSA.

Now again applying the \hat{F} -method along with the predicted spectral extinction coefficients, the monochromatic dependence on transmittance, reflectance and absorption can be studied for different tile thicknesses and incidence angles. Spectral transmittance and reflectance values for a 20 mm thick MSA tile is shown in Figure 5.2.8 for several incidence angles.

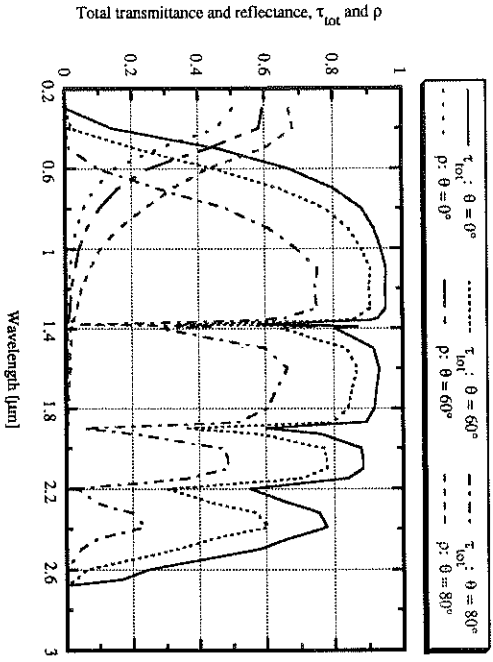


Figure 5.2.8. Calculated spectral transmittance and reflectance at different incidence angles for a 20 mm thick MSA tile. $\theta = 0^\circ, 60^\circ, 80^\circ$.

The total values were obtained by integrating the monochromatic values over the entire spectrum. The integrated (total) transmittance at angle θ then becomes

$$\tau(\theta) = \int_{\text{solar}} \tau_{\lambda}(\theta) i_{\lambda,i}(\theta) d\lambda \quad (5.2.20)$$

$$\rho(\theta) = \int_{\text{solar}} \rho_{\lambda}(\theta) i_{\lambda,i}(\theta) d\lambda$$

where $i_{\lambda,i}(\theta)$ = the incident monochromatic intensity arriving at the cover system from angle θ

$\tau_{\lambda}(\theta)$ = the spectral transmittance values at angle θ calculated by the \hat{F} -method
 A similar expression can be written for the integrated reflectance. Then the absorption is given by Equation 5.2.18.

For purposes of calculating optical properties of materials, which depend on the spectral distribution of solar radiation, it is convenient to have the distribution of terrestrial radiation in tabular form. Wiebel and Henderson (1979) have prepared such tables for several air masses (zenith angles) and atmospheric conditions. Table 5.2.1 shows the terrestrial spectrum divided into twenty equal increments of energy, with a mean wavelength for each increment that divides the increment into two equal parts. This table is for a relatively clear atmosphere and air mass two, and Duffie and Beckman (1980) recommend that it is used as a typical distribution of terrestrial beam radiation.

Table 5.2.1 Spectral distribution of terrestrial beam radiation at air mass 2 and 23 km visibility, in twenty equal increments of energy. From Duffie and Beckman (1980).

Energy band number	Wavelength range [\mu m]	Midpoint wavelength [\mu m]
1	0.300 - 0.434	0.402
2	0.434 - 0.479	0.458
3	0.479 - 0.517	0.498
4	0.517 - 0.557	0.537
5	0.557 - 0.595	0.576
6	0.595 - 0.633	0.614
7	0.633 - 0.670	0.652
8	0.670 - 0.710	0.690
9	0.710 - 0.752	0.730
10	0.752 - 0.799	0.775
11	0.799 - 0.845	0.820
12	0.845 - 0.894	0.869
13	0.894 - 0.975	0.923
14	0.975 - 1.035	1.003
15	1.035 - 1.101	1.064
16	1.101 - 1.212	1.170
17	1.212 - 1.310	1.258
18	1.310 - 1.603	1.532
19	1.603 - 2.049	1.689
20	2.049 - 5.000	2.292

With this approach the transmittance is calculated according to

$$\tau(\theta) = \frac{1}{N} \sum_{j=1}^N \tau_j(\theta) \tag{5.2.21}$$

where N = the number of equal increments

Calculated values of transmittance, reflectance, and absorptance for a 20 mm thick MSA tile is shown in Figure 5.2.9. The effect of scattering on the transmittance is clearly seen. The direct-diffuse transmittance is given as the difference between the total and the direct transmittance curves.

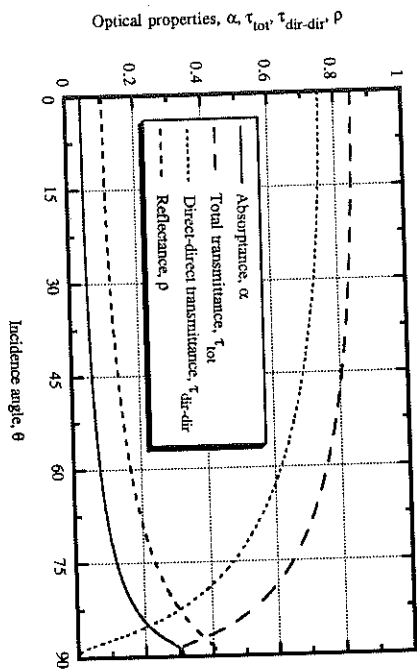


Figure 5.2.9 Calculated transmittance, reflectance, and absorptance values versus incidence angle for a 20 mm thick MSA tile.

Now again using the same procedure, the effects of increasing the MSA thickness may be studied. Figure 5.2.10 shows the effect of MSA thickness on transmittance. MSA by itself, despite scattering losses in the visible and O-H absorption in the infrared, has a higher total transmittance than conventional glass windows of equal thickness.

The transmittance of a 20 mm thick MSA tile equals that of single glass. Increasing MSA thickness to 45 mm reduces τ_{tot} to about 0.72, equal to double glass.

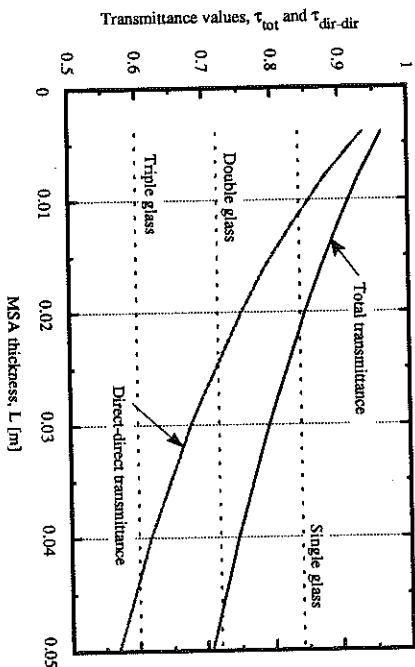


Figure 5.2.10 Calculated total and direct-direct transmittance of MSA versus MSA thickness compared to transmittance of conventional glass windows. All glass is 3 mm clear float glass.

5.2.4 Transmittance for Diffuse Radiation

The preceding analysis only applied to the beam component of solar radiation. Radiation incident on a collector also consist of scattered solar radiation from the sky and possible reflected solar radiation from the ground. The transmittance for diffuse radiation, τ_d , is calculated by

$$\tau_d = \frac{\int_A \tau_b(\theta) \cdot I \cdot \cos \theta \cdot d\omega}{\int_A I \cdot \cos \theta \cdot d\omega} \tag{5.2.22}$$

where τ_b is the transmittance for beam radiation, θ the incidence angle, I the radiation intensity and A the range of solid angle of incident diffuse radiation. In principle, the amount of this radiation that passes through the material can be calculated by integrating the transmitted radiation over all angles. However, the angular distribution of this radiation is generally unknown.

Brandemuhl and Beckman (1980) performed this integration for ordinary glazings by assuming the incident diffuse radiation distribution to be isotropic. The same assumption will be used in this study. They showed that the transmittance for isotropic diffuse ground radiation and isotropic diffuse sky radiation were given by the following equations

$$\tau_{d,ground} = \frac{\int_{\omega_e}^{\omega_{e2}} \int_{\alpha_e^{-1}(\cos \beta_{inc} = \theta)}^{\alpha_e} \tau_b(\theta) \cos \theta \sin \theta \, d\phi \, d\theta}{\int_{\omega_e}^{\omega_{e2}} \int_{\alpha_e^{-1}(\cos \beta_{inc} = \theta)}^{\alpha_e} \cos \theta \sin \theta \, d\phi \, d\theta} \tag{5.2.23}$$

$$\tau_{d,sky} = \frac{\int_0^{\omega_{e2}} \int_{\alpha_e}^{\alpha_e^{-1}(\cos \beta_{inc} = \theta)} \tau_b(\theta) \cos \theta \sin \theta \, d\phi \, d\theta + \int_{\omega_e}^{\omega_{e2}} \int_{\alpha_e^{-1}(\cos \beta_{inc} = \theta)}^{\alpha_e} \tau_b(\theta) \cos \theta \sin \theta \, d\phi \, d\theta}{\int_0^{\omega_{e2}} \int_{\alpha_e}^{\alpha_e^{-1}(\cos \beta_{inc} = \theta)} \cos \theta \sin \theta \, d\phi \, d\theta + \int_{\omega_e}^{\omega_{e2}} \int_{\alpha_e^{-1}(\cos \beta_{inc} = \theta)}^{\alpha_e} \cos \theta \sin \theta \, d\phi \, d\theta} \tag{5.2.24}$$

Equations 5.2.23 and 5.2.24 have been solved for two different MSA thicknesses (4 and 20 mm) using numerical integration techniques (Simpson rule). The results given in Figure 5.2.11 are presented in terms of the effective angle of incident beam radiation, θ_e , such that $\tau_d = \tau_b(\theta_e)$. The θ_e for the two MSA thicknesses were almost identical for all

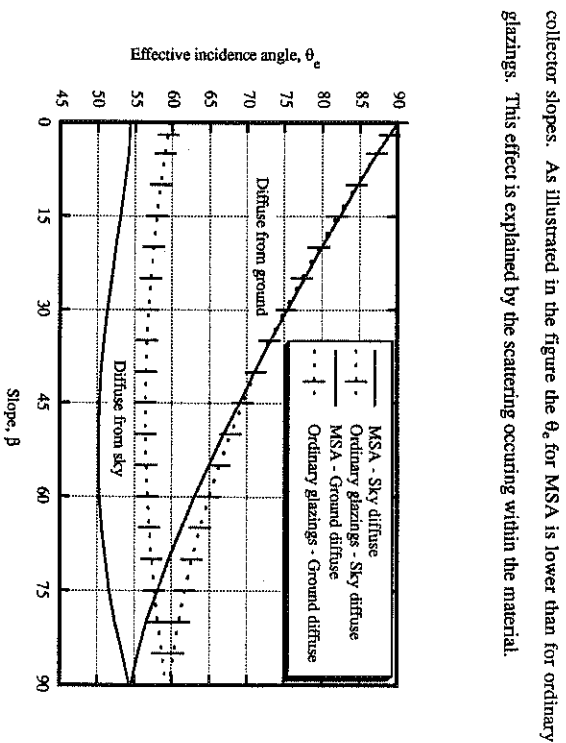


Figure 5.2.11 Effective beam radiation incidence angle for diffuse radiation from sky and ground on tilted MSA tile. The banded region includes the results obtained by Brandemuhl and Beckman (1980) for ordinary glazings.

The results can also be presented using least square curve fits. For diffuse ground radiation on a MSA tile with slope β (in degrees),

$$\theta_e = 90.0 - 0.5460\beta + 0.001631\beta^2 \tag{5.2.25}$$

For diffuse sky radiation on a MSA tile with slope β (in degrees),

$$\theta_e = 55.0 - 0.1913\beta + 0.001984\beta^2 \tag{5.2.26}$$

5.3 Infrared Heat Transfer in MSA

The thermal conduction within MSA is composed of two parts. One is a result of solid conduction throughout the aerogel skeleton, and the other is due to gas conduction within the air pores. The solid conduction is dependent upon MSA density, and the corresponding solid conductivity was found to be about $0.004 \text{ W/m}^2\text{C}$ at a density of 105 kg/m^3 [Capp and Fricke (1986)]. The gas conduction varies both with density, temperature, and internal pore pressure, P_p . As the typical pore size (100 nm) in MSA is smaller than the mean free path of the gas particles, the thermal conductivity of the gas is reduced. This is called the Knudsen effect.

5.3.1 Infrared Properties of MSA

Measurements of the thermal loss coefficient, h_{tot} , of MSA tiles versus internal pore pressure are shown in Figure 5.3.1. There is a small rise in h_{tot} between 0.01 and 0.1 mbar which is caused by a change in contact resistance between MSA and the boundary plates. A second increase is seen at $P_p \sim 0.1 \text{ bar}$. It is caused by the commencement of gas conduction within the large air pores of the MSA tile.

In order to eliminate the gas conduction, the material must be evacuated to a pressure below 0.1 bar. The system thus have to be degassed at elevated temperatures and air leakage has to be prevented by use of glass-metal seals [Jensen (1989)]. For evacuated systems k_p is ~ 0 , resulting in a constant conductivity $\sim 0.004 \text{ W/m}^2\text{C}$. Only evacuated MSA tiles will be considered in this work.

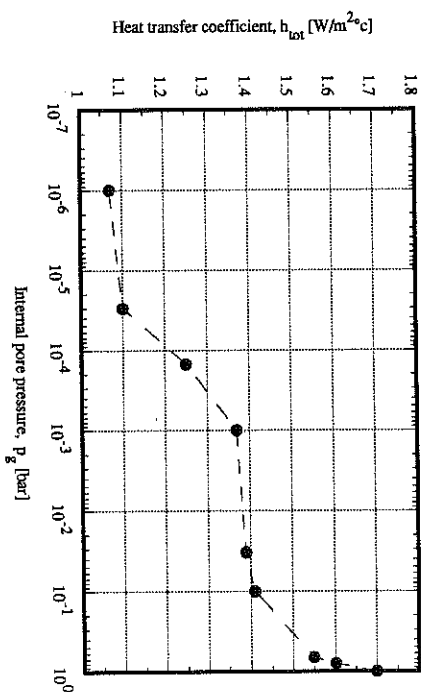


Figure 5.3.1 Thermal loss coefficient versus pore pressure. Adapted from Jensen (1989).

MSA absorbs and reemits radiation, but shows no scattering in the infrared because the structural inhomogeneities have dimensions in the order of 100 nm and below, which is much smaller than any infrared wavelength. The spectral absorption coefficient is shown in Figure 5.3.2.

The absorption in MSA is strong above $8 \mu\text{m}$, and especially weak between 3 and $5 \mu\text{m}$. In this wavelength region, the radiative transport will not be a local phenomenon anymore, and direct radiative communication between the boundaries may occur. Consequently, the radiative transport strongly varies with MSA thickness and the emissivities of the boundaries. In this case, the coupling between the radiation field and the heat flux caused by conduction has to be considered.

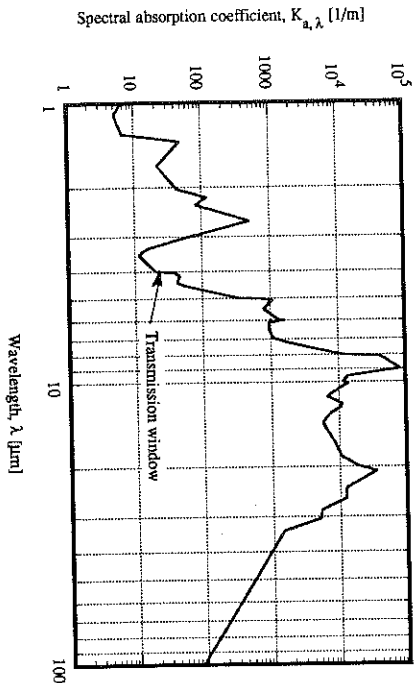


Figure 5.3.2 Absorption coefficient for MSA. Data adapted from Fricke (1986).

At low temperatures (window applications ~ 290K) the thermal IR-spectrum peaking around 10 μm is effectively attenuated, and the radiative transport through MSA is small. For increasing temperatures the transmission window between 3 and 5 μm becomes more significant as the peak of the thermal IR-spectrum moves toward the solar spectrum.

The resulting heat flux is determined by the temperatures and the emissivities of the boundary surfaces, the amount of conduction compared to radiative transfer, as well as the wavelength-dependent optical thickness. Approximate methods for the total heat flux in MSA have been developed by Scheuerrfing et al. (1986). These methods are based on the assumptions of small temperature differences between the boundary surfaces and that the boundary emissivities being equal. These assumptions are valid for window applications. However, for collector systems based on MSA these assumptions are no longer valid, and the predictions based on the approximate method will lead to incorrect results.

To obtain an exact solution for the combined conduction-radiation energy transfer in an absorbing-emitting and isotropic scattering medium, the general energy equation must be formulated. This is then solved subject to the boundary conditions to obtain the temperature distribution in the medium, and the heat flux can then be found. Siegel and Howell (1982) showed that integrating the radiative equation of transfer, Equation 5.2.3, over all solid angles yields the following equation for the conservation of radiative energy in a non-gray and isotropically scattering medium

$$\nabla \cdot q_r = 4 \int_{\lambda=0}^{\infty} K_{n,\lambda} E_{b\lambda} d\lambda - \int_{\lambda=0}^{\infty} \int_{\omega=0}^{4\pi} K_{n,\lambda} i_{\lambda}(\omega) d\omega d\lambda \quad (5.3.1)$$

where $E_{b\lambda}$ is Planck's spectral distribution of emissive power. Equation 5.3.1 states that the divergence of the radiative heat flux vector, $\nabla \cdot q_r$ is equal to the difference between the energy emitted and the energy absorbed. In addition there will be a net energy gain per unit volume by heat conduction equal to $k\nabla^2 T$. Equating the net gain by conduction to the net loss by radiation gives the energy equation for steady state simultaneous conduction and radiation

$$k\nabla^2 T - 4 \int_{\lambda=0}^{\infty} K_{n,\lambda} E_{b\lambda} d\lambda + \int_{\lambda=0}^{\infty} \int_{\omega=0}^{4\pi} K_{n,\lambda} i_{\lambda}(\omega) d\omega d\lambda = 0 \quad (5.3.2)$$

where k is the thermal conductivity. Since the radiation term in Equation 5.3.2 depend not only on the local temperature but on the entire surrounding radiation field, the energy equation is an integro-differential equation for the temperature distribution in the medium. The conduction term depend on a different power of the temperature than the radiation terms and the energy equation is thus nonlinear.

In the following a new method for solving Equation 5.3.2 for a 1-dimensional plane parallel system will be presented.

5.3.2 Combined Conduction and Radiation in an Absorbing-Emitting and Scattering Medium by the \bar{F} -Technique

Consider a conducting-radiating medium between two infinite parallel plates. The plates were assumed to be isothermal, diffuse reflectors, and emitters, and to have constant spectral radiative properties (gray surfaces). Plate 1 is at temperature T_1 , plate 2 is at T_2 , and the plates are a distance L apart. The plate areas are denoted A_1 and A_2 , respectively. The medium between the plates was assumed to have a constant thermal conductivity, a refractive index of one, and to be a homogeneous material in local thermodynamic equilibrium which can absorb, emit as well as scatter radiation. Scattering was assumed to be isotropic. Both gray and non-gray media will be considered.

The \bar{F} -technique begins by subdividing the material into n volume elements: $\Delta V_1, \Delta V_2, \dots, \Delta V_n$ as illustrated by Figure 5.3.3. The method is approximate in the sense that the non-isothermal medium is replaced by a number of finite isothermal subregions. In principle the division can be made as fine as necessary to yield any desired accuracy.

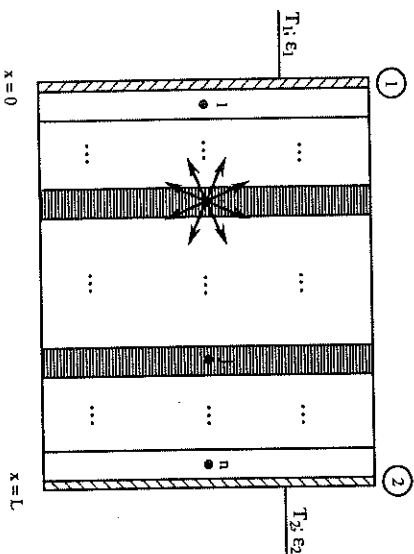


Figure 5.3.3 Schematic diagram of the physical system.

First consider the diffuse radiation leaving surface i which impinges on surface j . Some of the radiation leaving i will go directly to j , and some will reach j after one or more reflections and/or scatterings. The total exchange factor between surface i and j , \bar{F}_{s_i, s_j} , will be defined as the energy isotropically leaving surface i that strikes surface j by all possible paths divided by the energy isotropically leaving surface i . Now consider the diffuse radiation leaving surface i which is attenuated in volume element j . Some of the radiation leaving i will be directly attenuated in j , and some will be attenuated in j after one or more reflections and/or scatterings. The total exchange factor between surface i and volume j , \bar{F}_{s_i, v_j} , will be defined as the energy isotropically leaving surface i that is attenuated in volume element j in all possible ways divided by the energy isotropically leaving surface i .

Similarly, some of the radiation leaving volume element i will go directly to surface j , and some will reach j after one or more reflections and/or scatterings. The total exchange factor between volume element i and surface j , \bar{F}_{v_i, s_j} , will be defined as the energy isotropically leaving volume element i that strikes surface j by all possible paths divided by the energy isotropically leaving volume element i . Finally, some of the diffuse radiation leaving volume element i which is attenuated in volume element j will be directly attenuated in j , and some will be attenuated in j after one or more reflections and/or scatterings. The total exchange factor between volume i and j , \bar{F}_{v_i, v_j} , will be defined as the energy isotropically leaving volume element i that is attenuated in volume element j in all possible ways divided by the energy isotropically leaving volume element i .

The total exchange factors can be expressed in terms of the direct exchange factors, F_s , diffuse reflectances, ρ 's, albedos for scattering, Ω 's, and other \bar{F} 's in the following manner

$$\bar{F}_{s_i, s_j} = F_{s_i, s_j} + \sum_{k=1}^2 (\rho_k \bar{F}_{s_i, s_k} \bar{F}_{s_k, s_j}) + \sum_{k=1}^n (F_{s_i, v_k} \Omega_k \bar{F}_{v_k, s_j}) \quad (5.3.3)$$

$$\hat{F}_{j_i,vi} = F_{j_i,vi} + \sum_{k=1}^2 (F_{j_i,sk} \rho_k \hat{F}_{sk,vi}) + \sum_{k=1}^n (F_{j_i,vk} \Omega_k \hat{F}_{vk,vi}) \quad (5.3.4)$$

$$\hat{F}_{i,js} = F_{i,js} + \sum_{k=1}^2 (F_{i,sk} \rho_k \hat{F}_{sk,js}) + \sum_{k=1}^n (F_{i,vk} \Omega_k \hat{F}_{vk,js}) \quad (5.3.5)$$

$$\hat{F}_{j_i,vi} = F_{j_i,vi} + \sum_{k=1}^2 (F_{j_i,sk} \rho_k \hat{F}_{sk,vi}) + \sum_{k=1}^n (F_{j_i,vk} \Omega_k \hat{F}_{vk,vi}) \quad (5.3.6)$$

The values of the direct exchange factors can be expressed in terms of the third exponential integral as described in Section 5.2.2. It is also worth mentioning that Equation 5.2.8 and 5.3.5 are identical except for the third term in Equation 5.3.6 which accounts for reflections from the boundary plates. This term is ignored in Equation 5.3.6 due to the fact that the surface reflections in MSA can be neglected, and that no boundary plates are present in the system modeled in Section 5.2.2 (see Figure 5.2.5).

Equation 5.3.3 to Equation 5.3.6 must be solved simultaneously, and the solution technique described in Section 5.2.2 may be applied. Of course the equations can be solved by means other than matrix inversion.

Certain relationships between the \hat{F} 's will be introduced in order to reduce the computational effort. These properties are the summation rule and the reciprocity rule and are very similar to the summation and reciprocity rules for view factors. The summation rule can be developed by recognizing that the energy leaving a surface or a volume element must ultimately be absorbed by the surfaces and the volume elements in the system. The energy absorbed by surface j is $\epsilon_j \hat{F}_{ij}$ where the absorptance α_j has been replaced by the emittance ϵ_j since the surfaces are gray, and $(1-\Omega_j)F_{ij}$ denotes the energy absorbed by volume element j . Since all the energy must be absorbed, the sum over all surfaces and volume elements must be equal to unity.

$$\sum_{k=1}^2 (\epsilon_k \hat{F}_{i,sk}) + \sum_{k=1}^n ((1-\Omega_k) \hat{F}_{i,vk}) = 1 \quad \text{for } i = 1, 2 \quad (5.3.7)$$

$$\sum_{k=1}^2 (\epsilon_k \hat{F}_{i,sk}) + \sum_{k=1}^n ((1-\Omega_k) \hat{F}_{i,vk}) = 1 \quad \text{for } i = 1, 2, \dots, n \quad (5.3.8)$$

On a monochromatic basis*, it can easily be shown that the total exchange factors obey the laws of reciprocity:

$$A_k \hat{F}_{sk,si} = A_i \hat{F}_{si,sk} \quad \text{for } i, k = 1, 2 \quad (5.3.9)$$

$$A_i \hat{F}_{i,vk} = 4K_{T,k} \Delta V_k \hat{F}_{vk,si} \quad \text{for } i = 1, 2 \text{ and } k = 1, 2, \dots, n \quad (5.3.10)$$

$$\Delta V_i \hat{F}_{i,vk} = \Delta V_k \hat{F}_{vk,vi} \quad \text{for } i, k = 1, 2, \dots, n \quad (5.3.11)$$

where K_T is the total extinction coefficient (absorption and scattering) and A and ΔV denotes surface areas and volume of volume elements, respectively. The total exchange factors have validity independently of what other heat transfer mechanisms are present, and may be included in the total energy balances.

By means of the total exchange factors the inner integral in the absorption term in Equation 5.3.2 can be replaced by summation terms, and an energy balance can be written for each volume element. The energy balance for volume element i of the material is given by Equation 5.3.12 for a gray medium and Equation 5.3.13 for a non-gray medium.

$$k V_i^2 T_{vi} \Delta V_i - 4 K_{k,i} \Delta V_i \sigma T_{vi}^4 + (1 - \Omega_k) \sum_{k=1}^2 \epsilon_k A_k \sigma T_{sk}^4 \hat{F}_{sk,vi} + (1 - \Omega_k) \sum_{k=1}^n 4 K_{k,k} \Delta V_k \sigma T_{vk}^4 \hat{F}_{vk,vi} = 0 \quad (5.3.12)$$

and

* A subscript to separate monochromatic and gray values has up to now been dropped. Whenever the meaning is not clear, λ will be introduced to denote monochromatic values.

$$k V^2 T_{vi}^2 \Delta V_i - 4 \Delta V_i \sigma T_{vi}^4 \int_{\lambda=0}^{\infty} K_{a,\lambda} f_{\lambda T} d\lambda + \sum_{k=1}^n \epsilon_k A_k \sigma T_{sk}^4 \int_{\lambda=0}^{\infty} \hat{F}_{(sk,vi),\lambda} (1 - \Omega_{i,\lambda}) d\lambda + \sum_{k=1}^n 4 \Delta V_k \sigma T_{vk}^4 \int_{\lambda=0}^{\infty} K_{a,k,\lambda} f_{\lambda T} \hat{F}_{(vk,vi),\lambda} (1 - \Omega_{i,\lambda}) d\lambda = 0 \quad (5.3.13a)$$

with

$$f_{\lambda T} = \frac{C_1}{\sigma T^4 \lambda^5 \left[\exp \left(\frac{C_2}{\lambda T} \right) - 1 \right]} \quad (5.3.13b)$$

where

- A_k = area of surface k [m^2]
- C_1 = Planck's first radiation constant: $3.7405 \cdot 10^{-16}$ W m^2
- C_2 = Planck's second radiation constant: 0.0143879 W K
- $f_{\lambda T}$ = weight function of Planck's spectral distribution of emissive power
- $\hat{F}_{(vk,vi)}$ = total exchange factor between volume element k and volume element i
- $\hat{F}_{(sk,vi)}$ = total exchange factor between surface k and volume element i
- k = thermal conductivity [W/m K]
- $K_{a,k}$ = absorption coefficient in volume k [1/m]
- n = number of volume elements
- T = temperature [K]
- ϵ_k = emissivity of surface k
- ΔV_k = volume of volume element k [m^3]
- λ = wavelength [m]
- σ = Stefan-Boltzmann constant and is equal to $5.6697 \cdot 10^{-8}$ W/m 2 K 4
- Ω_i = albedo for scattering in volume element i
- λ denotes monochromatic values
- sk denotes surface k
- vk denotes volume element k

The first term in Equation 5.3.12 and Equation 5.3.13a represents the conduction contribution to volume element i . The second term describes the total amount of energy emitted from volume element i , and the third and fourth term represent the amount of

energy absorbed in volume element i , being originally emitted from the surfaces and volume elements in the enclosure, respectively.

The temperature distribution within the medium was found by expressing the conduction term in finite-difference form, and solving the n nonlinear equations by Newton-Raphson techniques. The conduction terms will contain temperatures to the first power, while the radiation terms will have temperatures to the fourth power

$$\begin{aligned} (a_{11} T_1 + a_{11} T_1^4) + \dots + (a_{1j} T_j + a_{1j} T_j^4) + \dots + (a_{1n} T_n + a_{1n} T_n^4) - b_1 &= 0 \\ (a_{21} T_1 + a_{21} T_1^4) + \dots + (a_{2j} T_j + a_{2j} T_j^4) + \dots + (a_{2n} T_n + a_{2n} T_n^4) - b_2 &= 0 \\ (a_{n1} T_1 + a_{n1} T_1^4) + \dots + (a_{nj} T_j + a_{nj} T_j^4) + \dots + (a_{nn} T_n + a_{nn} T_n^4) - b_n &= 0 \end{aligned} \quad (5.3.14)$$

The j th temperature is T_j and the coefficients for the linear and non-linear contributions of this temperature are a_{ij} and a_{ij}^4 , respectively.

In the Newton-Raphson procedure, an approximate value for each temperature is assumed. Let T_{j0} be this approximation for the j th temperature. Then a correction factor c_j will be computed so that $T_j = T_{j0} + c_j$. This corrected temperature is used to compute a new c_j , and the process is continued until the c_j becomes smaller than a specified value. The c_j are found from the following set of linear equations:

$$\begin{aligned} f_{11} c_1 + \dots + f_{1j} c_j + \dots + f_{1n} c_n + f_1 &= 0 \\ \vdots & \vdots \\ f_{j1} c_1 + \dots + f_{jj} c_j + \dots + f_{jn} c_n + f_j &= 0 \\ \vdots & \vdots \\ f_{n1} c_1 + \dots + f_{nj} c_j + \dots + f_{nn} c_n + f_n &= 0 \end{aligned} \quad (5.3.15)$$

The coefficients f_j are given by

$$f_j = \sum_{i=1}^n (a_{ij} T_{j0} + a_{ij}^4 T_{j0}^4) - b_i \quad (5.3.16)$$

and the f_{ij} are

$$f_{ij} = a_{ij} + 4 a_{ij}' T_{j0}^3 \quad (5.3.17)$$

When the medium is non-gray, the basic concepts are the same, although the inclusion of property variations does add some complexity to the functional form of the equations. The total exchange factors had to be solved on a monochromatic basis, and the integrals in Equation 5.3.12 had to be evaluated in each iteration. Simpson's rule was applied to compute the integrals.

Figure 5.3.4 shows different temperature distributions for a gray medium calculated by the \hat{F} -method for different values of the conduction-radiation parameter, $N = KK_g/4\sigma T^3$. For $N \rightarrow \infty$ conduction dominates and the solution reduces to the linear profile for conduction through a plane layer. When $N = 0$, the conduction term drops out and the temperature profile has a discontinuity (temperature slip) at each wall which is characteristic for the case of pure radiation. When conduction is present, there is no temperature slip.

Once the temperature distribution has been evaluated, the final step in the solution procedure is to calculate the heat transfer across the medium from plate 1 to plate 2. The total heat flux, q_{tot} , conductive plus radiative, at surface $x = 0$ can be expressed by the conduction term at surface 1 plus the difference between the radiation emitted by surface 1 and the radiation absorbed by surface 1. That is,

$$q_{tot} = - \left(k \frac{dT}{dx} \right)_{x=0} + \epsilon_1 A_1 \sigma T_{s1}^4 - \epsilon_1 \sum_{k=1}^N 4 K_{a,k} \Delta V_k \sigma T_{vk}^4 \hat{F}_{vk,s1} + \epsilon_1 \sum_{k=1}^2 \epsilon_k A_k \sigma T_{sk}^4 \hat{F}_{sk,s1} \quad (5.3.18)$$

for a gray medium, and

$$q_{tot} = - \left(k \frac{dT}{dx} \right)_{x=0} + \epsilon_1 A_1 \sigma T_{s1}^4 - \epsilon_1 \sum_{k=1}^2 \epsilon_k A_k \sigma T_{sk}^4 \int_{\lambda=0}^{\infty} \hat{F}_{(k,s1),\lambda} d\lambda - 4 \epsilon_1 \sum_{k=1}^N \Delta V_k \sigma T_{vk}^4 \int_{\lambda=0}^{\infty} K_{a,\lambda} f_{\lambda T} \hat{F}_{(v,s1),\lambda} d\lambda \quad (5.3.19)$$

for a non-gray medium.

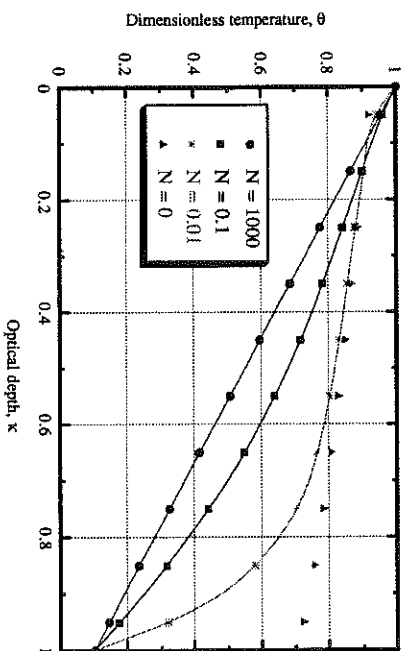


Figure 5.3.4 Dimensionless temperature distribution in a gray medium between infinite parallel black plates with simultaneous conduction and radiation. Plate temperature ratio $\theta_2 = 0.1$; optical thickness $\kappa_0 = 1.0$; albedo for scattering $\Omega = 0.0$.

Comparison of the results of the present method is made with the results of Viskanta (1965). Viskanta's results can be exactly reproduced by the \hat{F} -method as long as the grid spacing is made fine enough. The radiative flux reached Viskanta's solution within 1% in all cases with a uniform subdivision of 30. However, the conductive term required a subdivision of 5 times as fine to obtain the same accuracy, and the computer time was unacceptable high. The necessity for fine grid spacing is due to the calculation of the temperature gradient at $x = 0$. To overcome this obstacle and deploy computer power

more effectively non-uniform grid spacing was introduced near plate 1. A very fine subdivision was employed to the four volume elements closest up to plate 1, and a more coarse and uniform division was used for the rest of the geometry. In this way the number of grids necessary to obtain an accurate solution was reduced from 150 to 30 for a typical calculation.

As the absorption coefficient in MSA is strongly wavelength dependent Equation 5.3.13 with $\Omega = 0$ was employed to calculate the temperature distribution within the medium. The calculated heat flux for a 20 mm thick and evacuated MSA tile is compared to experimental data published by Scheuerflug et al. (1986) in Figure 5.3.5. The comparison was done in terms of the so called apparent thermal conductivity, k_{app} , under variation of average radiative temperature, T_R , for the medium. These two parameters are defined by the following relationships

$$k_{app} = \frac{q_{tot} L}{T_1 - T_2} \quad (5.3.20)$$

and

$$T_R = \left[\frac{1}{4} (T_1^2 + T_2^2) (T_1 + T_2) \right]^{1/3} \quad (5.3.21)$$

The predictions obtained with the \bar{F} -method agree very well with the conductivity measurements of MSA, and the agreement is much better than the simplified calculation procedure proposed by Caps and Frische (1986).

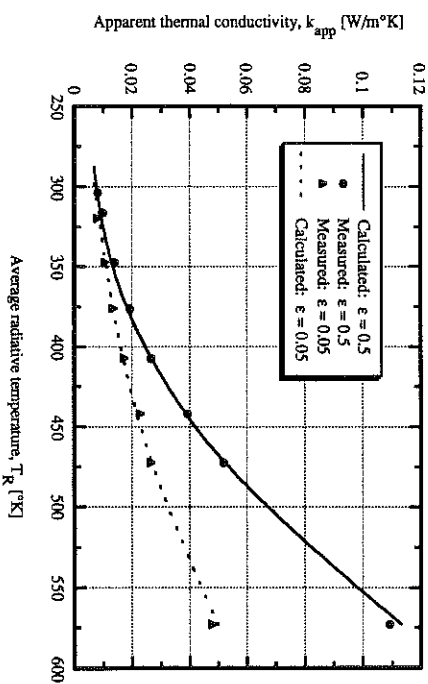


Figure 5.3.5 Apparent thermal conductivity of MSA under variation of average radiative temperature. Comparison \bar{F} -method and measurements at two different boundary emissivities ($\epsilon = 0.05$ and $\epsilon = 0.5$).

5.4 Transmittance-Absorptance Product for MSA Collectors

Except for absorber-parallel covers, most TIMs require some protection against weathering, rain, dust etc. An additional glass or film as an outside cover must therefore be included, which is the case for MSA. For other TIMs an additional film inside the outermost cover may be useful to suppress convection. Granular aerogel on the other hand require two window panes or stable plastic films as a container. For clear angle-preserving covers such as glass panes or honeycombs, (too-)products have been evaluated by several authors (e.g. Edwards (1977) and Symons (1984)), but the inclusion of scattering layers or irregularly reflecting layers complicates the calculation. In the following section an approximate method which allows the inclusion of scattering layers

is being derived. The new method is based on the embedding technique presented by Edwards (1977).

5.4.1 A New Method for Calculating the Solar Absorption by Each Element in an Absorber-Coverglass Array

To employ the embedding technique one imagines a stack of n elements including an absorber plate and $n-1$ coverglasses, and one formulates the effect of adding one or more elements to the array. The assumptions in the following are restrictive, but may allow the inclusion of scattering layers with sufficient accuracy in most cases. The diffuse reflections from the absorber will be assumed isotropic. Transmitted or reflected fluxes from a single layer will be split up in to components. A direct, angle-preserving flux for the incidence angle under consideration, and a component deflected by scattering or reflections, which will be treated as isotropic. This model is similar to the isotropic solar radiation model, which divides the radiation into a direct part and an isotropic diffuse sky component. Figure 5.4.1 shows the angular distribution of the backscattered (reflected) radiation from a slab with isotropic scattering, and it is obvious that the distribution is not isotropic.

In order to assess the errors introduced by assuming an isotropic distribution, three different values of the integrated reflectance and transmittance were employed. 1) values based on the largest angular intensity; 2) values based on the smallest angular intensity; and 3) values based on the integrated intensities. In all cases an isotropic distribution was assumed. The analysis showed that the difference in estimated $(\tau\alpha)_p$ -product for the MSA collector in Figure 5.1.1 was less than 4% for the different approaches, approach 3) being between 1) and 2). The author feels that the proposed method which is based on 3) is acceptable. Calculations in scattering layer transport have shown, that this approximation

may be used even for extremely anisotropic distributions, if it is replaced by an effective isotropic one [McKellar and Box (1981)].

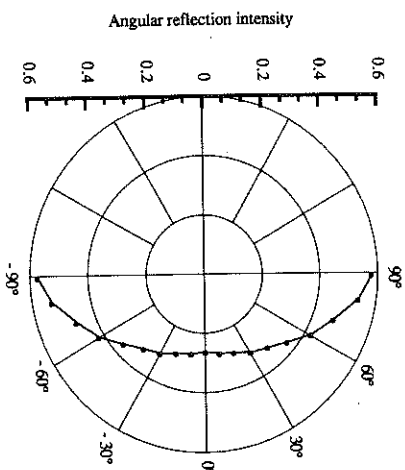


Figure 5.4.1 Angular distribution of diffuse reflections from a plane-parallel atmosphere with isotropic scattering of finite optical thickness and an albedo of 0.9.

The transmittance of the i th cover is therefore divided into a direct-direct component, τ_i^d , and a direct-diffuse component, τ_i^s . Similarly, are the reflectances of the i th cover denoted ρ_i^b and ρ_i^s , respectively, for the inside surface and ρ_i^a and ρ_i^s for the outside surface of the element. The transmittance of the i th element are equal on both faces due to the reciprocity principle. The absorbances of each face of element i , α_i and α_i are given by

$$\alpha_i = 1 - \rho_i^b - \rho_i^s - \tau_i^b - \tau_i^s \quad (5.4.1)$$

$$\alpha_i = 1 - \rho_i^a - \rho_i^s - \tau_i^a - \tau_i^s \quad (5.4.2)$$

The evaluation of diffuse properties are described in Section 5.2.5. τ_i^d , ρ_i^d and ρ_i^r denotes the transmittance and reflectances for diffuse fluxes incident on the i th element. The diffuse absorptances of element i can be then be expressed as

$$q_i^d = 1 - \rho_i^d - \tau_i^d \quad (5.4.3)$$

$$q_i^r = 1 - \rho_i^r - \tau_i^r \quad (5.4.4)$$

Allowance is thus made for optical coatings such as antireflection films and/or thin oxide IR-reflecting films being different on each face of each coverglass element. The incoming flux, q_{n+1} , outside the system is direct and normalized to unity. The other fluxes are made up of a direct and a diffuse component, q_{n+1}^b and q_{n+1}^d , respectively. This is illustrated in Figure 5.4.2.

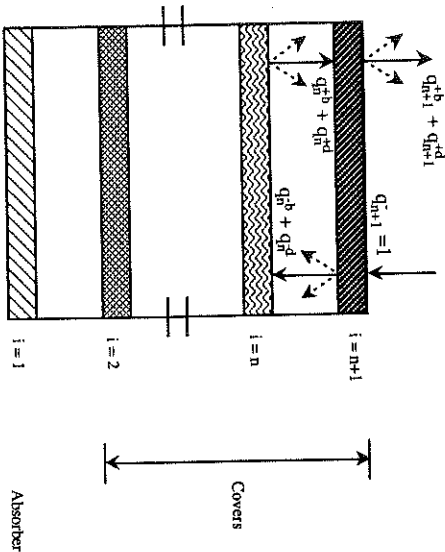


Figure 5.4.2 Embedding a stack of n covers.

Since q_{n+1} is normalized to unity, the outgoing fluxes from the system, q_{n+1}^b and q_{n+1}^d , are given by the following relationships

$$q_{n+1}^b = R_{n+1}^b \quad (5.4.5)$$

$$q_{n+1}^d = R_{n+1}^{sd} \quad (5.4.6)$$

where R_{n+1}^b and R_{n+1}^{sd} are the top-of-the- $n+1$ -stack reflectances due to reflection of the direct incident flux and scattering, respectively. The incoming fluxes for the n th cover element are given by (see Figure 5.4.2).

$$q_n^b = r_{n+1}^b + \rho_{n+1}^b q_n^b \quad (5.4.7)$$

$$q_n^d = r_{n+1}^d + \rho_{n+1}^d q_n^b + \rho_{n+1}^d q_n^d \quad (5.4.8)$$

Similarly, the outgoing fluxes can be expressed by the following expressions

$$q_n^b = R_n^b q_n^b \quad (5.4.9)$$

$$q_n^d = R_n^s q_n^b + R_n^d q_n^d \quad (5.4.10)$$

where R_n^d is the top-of-the- n -stack reflectance due to reflections of diffuse fluxes incident on the surface.

Combining Equation 5.4.7 and 5.4.9 and Equation 5.4.8 and 5.4.10 give the following relations for the incoming fluxes

$$q_n^b = \frac{r_{n+1}^b}{(1 - \rho_{n+1}^b R_n^b)} \quad (5.4.11)$$

$$q_n^d = \frac{r_{n+1}^d}{(1 - \rho_{n+1}^d R_n^d)} + q_n^b \left[\frac{\rho_{n+1}^s R_n^b + \rho_{n+1}^d R_n^d}{(1 - \rho_{n+1}^d R_n^d)} \right] \quad (5.4.12)$$

For convenience the top of the stack transmittances are defined as

$$t_{n+1}^b = \frac{q_n^b}{q_{n+1}^b} = q_n^b \quad (5.4.13)$$

$$q_{n+1}^s = \frac{q_n^d}{q_{n+1}} = q_n^d \quad (5.4.14)$$

The outgoing fluxes above the new element are

$$q_{n+1}^{+b} = \rho_{n+1}^b + \tau_{n+1}^b \cdot q_n^{+b} \quad (5.4.15)$$

$$q_{n+1}^{+d} = \rho_{n+1}^s + \tau_{n+1}^s \cdot q_n^{+b} + \tau_{n+1}^d \cdot q_n^{+d} \quad (5.4.16)$$

Substituting Equation 5.4.5 and 5.4.11 into Equation 5.4.15, and Equation 5.4.6 and 5.4.12 into Equation 5.4.16 give the desired relations for the overall reflectances of the stack embedded by one more cover

$$R_{n+1}^b = \rho_{n+1}^b + \tau_{n+1}^b \cdot R_n^b \cdot \tau_{n+1}^b \quad (5.4.17)$$

$$R_{n+1}^s = \rho_{n+1}^s + \tau_{n+1}^s \cdot R_n^b \cdot \tau_{n+1}^b + \tau_{n+1}^d \cdot [R_n^s \cdot \tau_{n+1}^b + R_n^d \cdot \tau_{n+1}^d] \quad (5.4.18)$$

A top-of-the-stack absorptance is introduced as

$$a_{n+1} = \alpha_{n+1}^b \cdot q_n^{+b} + \alpha_{n+1}^s \cdot q_n^{+s} + \alpha_{n+1}^d \cdot q_n^{+d} + \alpha_{n+1}^d \cdot q_{n+1}^d \quad (5.4.19)$$

From Equation 5.4.9 to 5.4.18, Equation 5.4.19 can be rewritten as

$$a_{n+1} = \alpha_{n+1}^b \cdot R_n^b \cdot \tau_{n+1}^b + \alpha_{n+1}^s \cdot (R_n^s \cdot \tau_{n+1}^b + R_n^d \cdot \tau_{n+1}^d) \quad (5.4.20)$$

For an N-element stack subjected to normalized solar radiation, one can find the fraction $A_{N,N}$ of the radiation absorbed by the outermost cover from the value a_N . For each successive element below the outer one the downgoing flux is

$$q^{+d} = \tau_{i+1}^b \cdot q_{i+1}^{+b} + \tau_{i+1}^s \cdot q_{i+1}^{+s} + \tau_{i+1}^d \cdot q_{i+1}^{+d} \quad (5.4.21)$$

beginning with $i = N$. The within-stack absorptance $A_{i,N}$ is then given by the following relation

$$A_{i,N} = a_i \cdot \tau_{i+1}^b \cdot q_{i+1}^{+b} + a_i^d \cdot [\tau_{i+1}^s \cdot q_{i+1}^{+s} + \tau_{i+1}^d \cdot q_{i+1}^{+d}] \quad (5.4.22)$$

The conservation of energy gives

$$R_N^b + R_N^s + A_{1,N} + A_{2,N} + \dots + A_{N,N} = 1 \quad (5.4.23)$$

This relation may be used to check the calculation.

The procedure of calculating the (cc)-product starts with calculating the single layer transmittances and reflectances. The embedding calculation then starts with the bare absorber for which

$$R_1^b = [1 - \alpha(\theta)] \left(1 - \frac{P_{diff}}{P_{tot}} \right) \quad (5.4.24)$$

$$R_1^s = [1 - \alpha(\theta)] \cdot \frac{P_{diff}}{P_{tot}} \quad (5.4.25)$$

$$a_1 = \alpha_{abs}(\theta) \quad (5.4.26)$$

Then the first cover, element 2, is added, and b_2^b , τ_2^b , R_2^b , R_2^s , and a_2 are found from the above equations. Then the second cover is added and so on until the outermost Nth element is included. (For an architectural application, the effective reflectance of the room behind the multiple-glazed window is used for R_1 .)

By repeated use of Equations 5.4.21 and 5.4.22 the solar absorption by each element within the collector could be evaluated. Figure 5.4.3 shows the within-stack absorptances versus incidence angle for the MSA collector. At normal incidence 72% of the solar radiation is absorbed by the absorber plate, 3.8% is absorbed by the MSA tile, and 4.2% is absorbed by the glass cover. The rest 20% is reflected away.

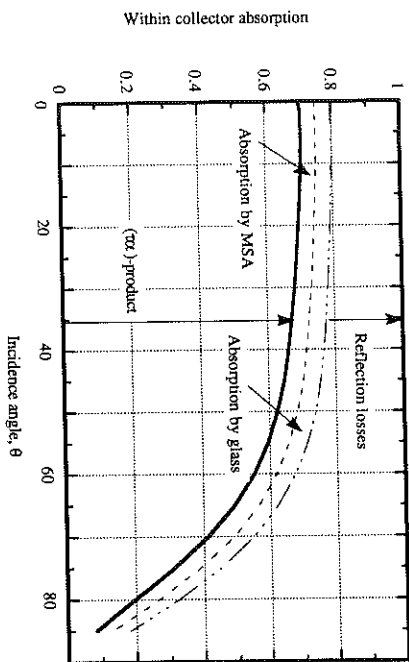


Figure 5.4.3 Within-stack absorptances versus incidence angle for the MSA collector

5.4.2 Incidence Angle Modifier for MSA Collectors

The value of the $(\tau\alpha)$ -product is dependent on the collector configuration and varies with the angle of incidence as well as with the relative values of diffuse and beam radiation. To model this dependence an incidence angle modifier can be introduced into Equation 2.2.1. Souka and Sarwat (1966) suggested that the incidence angle modifier could be written

$$K_{\tau\alpha} = \frac{(\tau\alpha)}{(\tau\alpha)_0} \tag{5.4.27}$$

Standard test methods [ASHRAE (1977)] include experimental estimation of this effect by assuming the entire radiation to be beam, and to use the following expression for the angular dependence of $K_{\tau\alpha}$

$$K_{\tau\alpha} = 1 + b_0 \left(\frac{1}{\cos \theta} - 1 \right) \tag{5.4.28}$$

where b_0 is a constant, an incidence angle modifier coefficient. The calculated incidence angle modifier is shown in Figure 5.4.4 for the MSA collector as a function of $[(1/\cos \theta) - 1]$. It is seen that $K_{\tau\alpha}$ is linear all the way out to values of the abscissa of 2, corresponding to an incidence angle of 75° . The value of b_0 was determined to -0.216. It should be noted that Equation 5.4.28 gives misleading results for ordinary glazings at incidence angles larger than 60° .

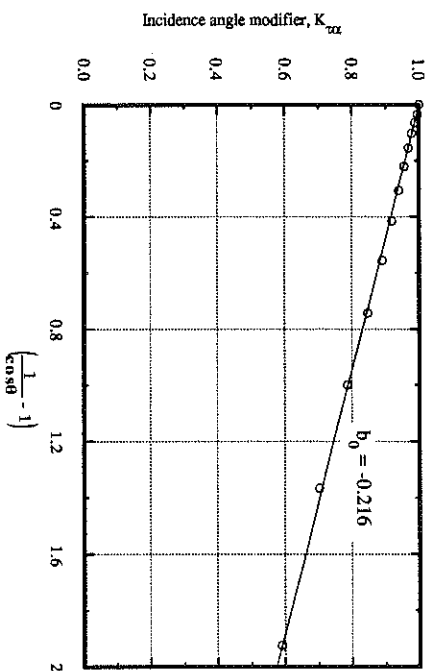


Figure 5.4.4 Incidence angle modifier coefficient as a function of $(1/\cos \theta - 1)$.

However, Equation 5.4.28 presumes that all incident radiation strikes the collector at the same incidence angle, which is not true because of the presence of diffuse and ground-reflected radiation. By assuming isotropic diffuse radiation, the absorbed solar radiation, S , can be expressed as

$$S = (\tau\alpha)_0 \left[I_b R_b K_{\tau\alpha, b} + I_d \frac{(1 + \cos \beta)}{2} K_{\tau\alpha, d} + P_g \frac{(1 - \cos \beta)}{2} K_{\tau\alpha, g} \right] \tag{5.4.29}$$

The subscripts b,d, and g represent beam, diffuse, and ground-reflected. For a given collector tilt, the same procedure as described in Section 5.2.5 was used to calculate effective beam incidence angles for the $(\tau\alpha)$ -product of diffuse sky and ground reflected radiation. The input to this calculation was the incidence angle dependent $(\tau\alpha)$ -product predicted by the modified embedding technique. This analysis revealed that the effective incidence angles evaluated for the transmittance in MSA also was valid for the $(\tau\alpha)$ -product in MSA collectors. Equation 5.4.29 can be written in terms of a total incidence angle modifier as follows

$$S = I_T K_{\tau\alpha}(\tau\alpha)_m \quad (5.4.30)$$

where the total incidence angle is given by

$$K_{\tau\alpha} = \frac{I_b}{I_T} R_b \left[1 + b_0 \left(\frac{1 - \cos \theta}{\cos \theta} - 1 \right) \right] + \frac{I_d}{I_T} \left(\frac{1 + \cos \theta}{2} \right) \left[1 + b_g \left(\frac{1 - \cos \theta_{a,d}}{\cos \theta_{a,d}} - 1 \right) \right] + \frac{I_g}{I_T} \left(\frac{1 - \cos \beta}{2} \right) \left[1 + b_g \left(\frac{1 - \cos \theta_{a,g}}{\cos \theta_{a,g}} - 1 \right) \right] \quad (5.4.31)$$

5.5 Useful Energy Gain from MSA Collectors

5.5.1 Collector Overall Heat Loss Coefficient

In order to use the Hottel-Whillier collector equation an overall heat loss coefficient, U_L , must be evaluated for the MSA collector. The basic idea behind introducing U_L is to represent the total thermal losses from the collector in terms of one characteristic parameter. This is illustrated with the equivalent thermal network in Figure 5.5.1

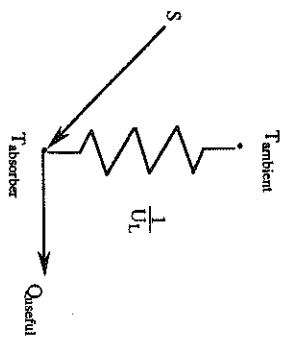


Figure 5.5.1 Equivalent thermal network for flat-plate collectors.

If it is assumed that all losses to the environment occur to the same ambient temperature, then the collector overall loss coefficient is the sum of the top, bottom, and edge loss coefficients.

$$U_L = U_T + U_b + U_e \quad (5.5.1)$$

To model the heat transfer in a MSA collector, a number of assumptions was introduced.

These assumptions are as follows:

- 1) The solar energy transfer can be calculated independent of the infrared radiation interexchange (semi-gray assumptions).
- 2) The physical system can be considered as a number of nodes with uniform properties and uniform incident solar radiation.
- 3) There is one-dimensional heat flow through the system.
- 4) The glass cover is gray and opaque to long-wavelength radiation
- 5) The sky can be considered as a blackbody for infrared radiation at an equivalent sky temperature.
- 6) Performance is steady state.

For each node of a combined heat-transfer problem, a general energy balance will include solar radiation, long-wavelength radiation, conduction, convection and internal energy generation. In solar energy systems the heat generation term is generally zero. The solar

radiation term is given by the embedding technique in Section 5.4.1, while long wavelength plus conduction terms are described in Section 5.3.2.

This study revealed that the temperature drop through the glass cover was negligible, and that one node was sufficient to represent the temperature distribution within the glass plate. However, the MSA tile had to be divided into 30 volume elements for reasons explained in Section 5.3.2. Furthermore, a harmonic mean value of the interface conductivity, k_{int} , between the outermost MSA node and the glass node has been evaluated according to the technique recommended by Patankar (1980).

$$k_{int} = \delta x \left(\frac{\delta x_{vn}}{k_{MSA}} + \frac{\delta x_g}{k_g} \right)^{-1} \quad (5.5.2)$$

where the distances, δx , δx_{vn} and δx_g are shown in Figure 5.5.2.

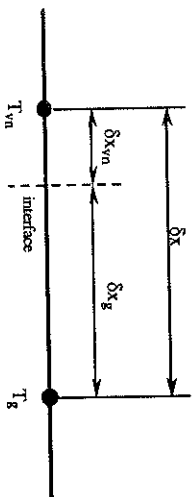


Figure 5.5.2 Distances associated with the interface between glass and aerogel.

The energy balance for the glass node can then be written as

$$\begin{aligned} \alpha_{g,soil} I_r + h_w A_g (T_a - T_g) + \epsilon_g A_g \sigma (T_{sky}^4 - T_g^4) + \left[\frac{\delta x_{vn}}{k_{MSA}} + \frac{\delta x_g}{k_g} \right]^{-1} (T_{vn} - T_g) + \\ \epsilon_g \sum_{k=1}^n 4AV_k \sigma T_k^4 \int_{\lambda=0}^{\infty} K_{k,\lambda} f_{\lambda T} \hat{F}_{(vk,sg),\lambda} d\lambda + \epsilon_g \sum_{k=1}^2 \epsilon_k A_k \sigma T_{sk}^4 \int_{\lambda=0}^{\infty} \hat{F}_{(sk,sg),\lambda} d\lambda - \\ \epsilon_g A_g \sigma T_g^4 = 0 \end{aligned} \quad (5.5.3)$$

The first term takes the absorbed solar radiation into account, and the second and third term represent the losses to the surroundings due to convection and sky radiation, respectively. In the fourth term the conduction contribution to the glass cover has been expressed in finite difference form. Term five and six describe the amount of long-wavelength radiation absorbed by the glass cover, while the last term represents the long-wavelength radiation emitted by the glass cover.

Three different forms of the nodal energy balance occur during the subdivision of the MSA tile:

Outermost MSA node ($i = n$):

$$\begin{aligned} \alpha_{vn,soil} I_r + \left[\frac{\delta x_{vn}}{k_{MSA}} + \frac{\delta x_g}{k_g} \right]^{-1} (T_g - T_{vn}) + \frac{k_{MSA} \Delta x (T_{vn(i-1)} - T_{vn})}{\Delta x} + \\ \sum_{k=1}^n 4AV_k \sigma T_k^4 \int_{\lambda=0}^{\infty} K_{k,\lambda} f_{\lambda T} \hat{F}_{(vk,vn),\lambda} d\lambda + \sum_{k=1}^2 \epsilon_k A_k \sigma T_{sk}^4 \int_{\lambda=0}^{\infty} \hat{F}_{(sk,vn),\lambda} d\lambda - \\ 4AV_n \sigma T_{vn}^4 \int_{\lambda=0}^{\infty} K_{n,\lambda} f_{\lambda T} d\lambda = 0 \end{aligned} \quad (5.5.4)$$

Ordinary MSA node ($1 < i < n$):

$$\begin{aligned} \alpha_{vi,soil} I_r + \frac{k_{MSA} (T_{v(i-1)} - 2T_{vi} + T_{v(i+1)})}{\Delta x} + \\ \sum_{k=1}^n 4AV_k \sigma T_k^4 \int_{\lambda=0}^{\infty} K_{k,\lambda} f_{\lambda T} \hat{F}_{(vk,vi),\lambda} d\lambda + \sum_{k=1}^2 \epsilon_k A_k \sigma T_{sk}^4 \int_{\lambda=0}^{\infty} \hat{F}_{(sk,vi),\lambda} d\lambda - \\ 4AV_i \sigma T_{vi}^4 \int_{\lambda=0}^{\infty} K_{i,\lambda} f_{\lambda T} d\lambda = 0 \end{aligned} \quad (5.5.5)$$

Innermost MSA node ($i = 1$):

$$\alpha_{v1, \text{sol}} I_T + \frac{k_{\text{MSA}}}{\Delta x} (2T_{\text{abs}} - 3T_{v1} + T_{v2}) + \sum_{k=1}^n 4\Delta V_k \sigma T_{vk}^4 \int_{\lambda=0}^{\infty} K_{k,\lambda} f_{\lambda T} \bar{F}_{(k,v1),\lambda} d\lambda + \sum_{k=1}^2 \epsilon_k \Delta x_k \sigma T_{sk}^4 \int_{\lambda=0}^{\infty} \bar{F}_{(k,v1),\lambda} d\lambda - 4\Delta V_1 \sigma T_{v1}^4 \int_{\lambda=0}^{\infty} K_{n1,\lambda} f_{\lambda T} d\lambda = 0 \quad (5.5.6)$$

Figure 5.5.3 illustrates the nodal scheme adjacent to the absorber plate.

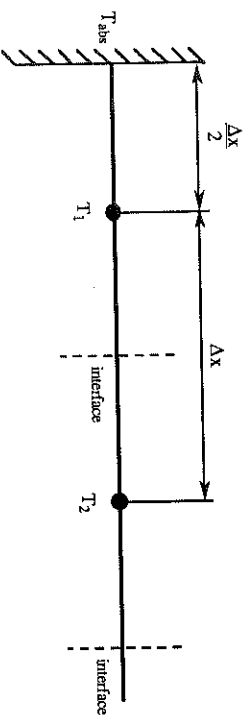


Figure 5.5.3 Nodes near the boundary.

Again using an iterative Newton-Raphson technique, values of the $n+1$ unknown temperatures were found. Based on these temperatures an apparent thermal conductivity was evaluated for the MSA tile. The calculation procedure was described in Section 5.3.2. The resistance from the absorber to the glass cover, R_1 , due to combined conduction and radiation in MSA can be expressed in terms of the apparent thermal conductivity and the tile thickness.

$$R_1 = \frac{L}{k_{\text{app}}} \quad (5.5.7)$$

Similarly, R_2 is the resistance from the glass cover to the surroundings, and is given by

$$R_2 = \frac{1}{hw + \epsilon_g \sigma T_g^4 - T_{\text{sky}}^4} \quad (5.5.8)$$

For this MSA collector, the top loss coefficient from the absorber plate to the ambient is

$$U_t = \frac{1}{R_1 + R_2} \quad (5.5.9)$$

The top loss coefficient was then evaluated for different absorber plate temperatures, absorber plate emittances, wind heat transfer coefficients, and ambient and sky temperatures.

The use of a blackbody radiation sky temperature not equal to the air temperature did not significantly effect U_t . Less than 1% increase in U_t was observed when the sky temperature was reduced from 10 to 0°C. The same percentage change (decrease) was found at an absorber plate temperature of 150°C when the absorber plate emittance was changed from 0.9 to 0.1. The change in U_t decreased with decreasing absorber plate temperatures. The negligible loss reduction obtained by selective coatings was expected due to the low apparent thermal conductivity in MSA (see Figure 5.3.5). An increase in U_t in the magnitude of 1% was observed when the wind heat transfer coefficient was increased from 5 to 20 W/m²°C. This change is much smaller than for ordinary collectors, and is also explained by the insulation properties of MSA.

When a similar analysis is performed for collectors with ordinary glazings, it is assumed that the absorbed solar radiation by covers will not affect the losses from the collector. This effect is accounted for by introducing an effective transmittance-absorptance product [Duffie and Beckman (1980)]. Even though the term concerning absorbed solar radiation is included in Equations 5.5.3 - 5.5.6 it will be ignored in the following calculations. By doing this, and evaluate an effective transmittance-absorptance product for the MSA collector, the simplicity of the theory for ordinary flat-plate collectors will be maintained.

The calculation of the top loss coefficient for the MSA collector is a very tedious process. To simplify the evaluation of collector performance, Figure 5.5.4 has been prepared. The figure shows the top loss coefficient for the MSA collector in Figure 5.1.1 for ambient temperatures of 25, 10, and -10°C for a range of absorber plate temperatures. The effect of MSA thickness is also included in the figure. In this case the ambient temperature was kept at 10°C. The calculations were performed using a wind heat transfer coefficient of 10 W/m²°C.

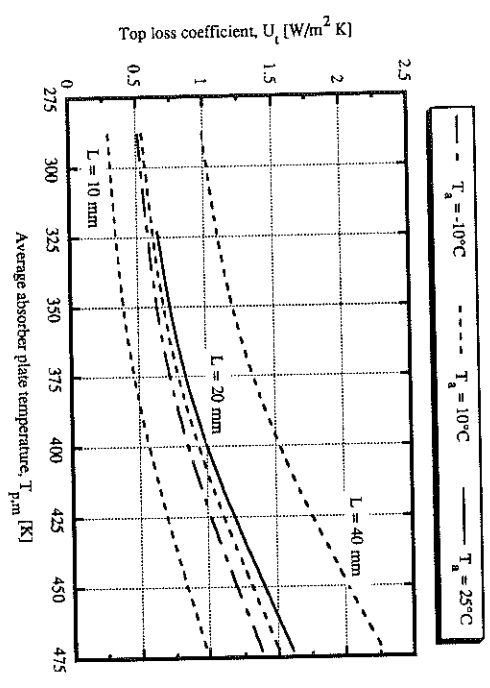


Figure 5.5.4 Top loss coefficient versus average absorber plate temperatures at different ambient temperatures. The effect of MSA thickness is also illustrated.

The above results show that U_t is strongly dependent upon the absorber plate temperature and the MSA thickness. The ambient temperature also seems to play an important role, while the other parameters have minor influence on U_t (maximum 2%). This is clearly seen from the magnitudes of R_1 and R_2 ($R_1 \gg R_2$).

To use Figure 5.5.4 to find U_t , it is necessary to know the mean absorber plate temperature, $T_{p,m}$. A method for estimating $T_{p,m}$ is given in the next subsection. The heat loss through the bottom of the collector is represented by the resistance to heat flow through the back insulation, R_3 , and convection and radiation resistance to the environment, R_4 . For ordinary back insulation it is usually possible to ignore R_4 ($R_3 \gg R_4$). Thus, the back loss coefficient can be approximated by [Duffie and Beckman (1980)]

$$U_b = k/D \tag{5.5.10}$$

where k and D are the insulation thermal conductivity and thickness, respectively. The MSA collector shown in Figure 5.1.1 is symmetric about the absorber, and U_b is therefore given by the same equations as U_t .

The edge loss coefficient, U_e was estimated by assuming one-dimensional sideways heat flow around the perimeter of the collector system. Duffie and Beckman (1980) expressed U_e in terms of the edge loss coefficient area product $(UA)_{edge}$ and the collector area A_c

$$U_e = \frac{(UA)_{edge}}{A_c} \tag{5.5.11}$$

The collector overall loss coefficient can then be evaluated from Equation 5.5.1. Table gives calculated values of U_t , U_b , and U_e for the MSA collector shown in Figure 5.1.1 for absorber plate temperatures of 323, 353 and 413°C.

Table 5.5.1 Calculated loss coefficients.

Absorber plate temperature [°K]	323	353	413		
U_t [W/m ² K]	0.609	0.703	1.000		
U_b [W/m ² K]	0.531	0.531	0.531	0.609	0.703
U_e [W/m ² K]	0.120	0.138	0.197		
U_L [W/m ² K]	1.260	1.372	1.728	1.338	1.544
				2.197	

These values were calculated using a wind heat transfer coefficient of $10 \text{ W/m}^2\text{K}$, and a MSA thickness of 20 mm. The collector dimensions were $1.22\text{m} \times 1.22\text{m} \times 60 \text{ mm}$.

5.5.2 Collector Heat Removal Factor and Mean Plate Temperature

In order to use Equation 2.2.1 to estimate the useful energy gain from a collector, Q_u , the heat removal factor, F_r , has to be evaluated. F_r accounts for the absorber plate temperature distribution and allows the collector performance to be expressed in terms of the fluid inlet temperature. Duffie and Beckman (1980) showed that F_r could be expressed as

$$F_r = \frac{\dot{m} C_p}{A_c U_L} \left[1 - \exp(-A_c U_L F / \dot{m} C_p) \right] \quad (5.5.12)$$

where A_c = the collector area [m^2]

C_p = specific heat of collector fluid [$\text{J/kg}^\circ\text{C}$]

F = collector efficiency factor

\dot{m} = collector fluid flow rate [kg/s]

U_L = the collector overall heat loss coefficient [$\text{W/m}^2\text{C}$]

At a particular location, F represents the ratio of the actual useful energy gain to the useful energy gain that would result if the collector absorbing surface had been at the local fluid temperature. The collector efficiency factor is given by

$$F = \frac{1}{W \left[\frac{1}{U_L [D + (W - D) F]} + \frac{1}{C_b} + \frac{1}{\pi D_i h_{f,i}} \right]} \quad (5.5.13)$$

where C_b = the bond conductance [$\text{W/m}^2\text{C}$]

D = the tube diameter [m]

D_i = the inside tube diameter [m]

F = the standard fin efficiency for straight fins with rectangular profile

$h_{f,i}$ = heat transfer coefficient between the fluid and the tube wall [$\text{W/m}^2\text{C}$]

U_L = the collector overall heat loss coefficient [$\text{W/m}^2\text{C}$]

W = the distance between two tubes

The fin efficiency can be calculated from the knowledge of the absorber plate thickness, δ , the bond thermal conductivity, k , W , D and U_L

$$F = \frac{\tanh \left[\frac{m(W-D)}{2} \right]}{m \frac{(W-D)}{2}} \quad (5.5.14)$$

where $m^2 = U_L / k\delta$.

To evaluate collector performance, it is necessary to know U_L and $h_{f,i}$. Both parameters are functions of temperature. The mean fluid temperature, $T_{f,m}$, is the proper temperature to evaluate fluid properties needed to predict $h_{f,i}$. Klein et al. (1974) showed that $T_{f,m}$ could be expressed as

$$T_{f,m} = T_{f,i} + \frac{Q_u/A_c}{U_L F_r} \left(1 - \frac{F_r}{F} \right) \quad (5.5.15)$$

The mean absorber plate temperature can be used to calculate the useful energy gain of a collector, and is given by

$$T_{p,m} = T_{f,i} + \frac{Q_u/A_c}{U_L F_r} (1 - F_r) \quad (5.5.16)$$

Equation 5.5.16 can be solved in an iterative manner with the expression for U_L . First an estimate of $T_{p,m}$ is made from which U_L is estimated. With approximate values of F_r , F , and Q_u , a new mean absorber plate temperature is obtained from Equation 5.5.16 and used to find a new value of the top loss coefficient. The new value of U_L is used to refine F_r , and F , and the process is repeated until a satisfactory accuracy is obtained.

5.5.3 Effective Transmittance-Absorptance Product

To maintain the simplicity of Hottel-Whillier collector equation, and account for the reduced losses due to absorption of solar radiation by the covers, Duffie and Beckman introduced an effective transmittance-absorptance product, $(\tau\alpha)_e$. The same approach will be followed for the MSA collector in this study.

All of the solar radiation that is absorbed by a cover system is not lost, since this absorbed energy tends to increase the cover temperatures and consequently reduce the losses from the absorber plate. Duffie and Beckman assumed that the small amount of absorption in the cover and consequent increased cover temperature does not change the values of the conduction, convection, and radiation resistances. Furthermore, they showed that the reduction in collector losses due to absorption in the cover, D , was given by the following relation for a one cover collector

$$D = I_r A_g \frac{U_L}{U_{g-a}} \quad (5.5.17)$$

A similar analysis for the MSA collector gave the following expression for D

$$D = I_r \left[A_g \frac{U_L}{U_{g-a}} + A_{ag} \frac{U_L}{U_{ag-a}} \right] \quad (5.5.18)$$

where A_g = the within glass cover absorptance

A_{ag} = the within MSA absorptance

I_r = the incident solar radiation [W/m^2]

U_L = the top loss coefficient [W/m^2C]

U_{g-a} = the loss coefficient from the glass cover to the surroundings =

$$1/R_2 [W/m^2C]$$

U_{ag-a} = the loss coefficient from the MSA glazing to the surroundings = U_L [W/m^2C]

D can also be considered as an additional input in the collector equation. The useful gain of the MSA collector is then

$$q_u = I_r \left\{ S + I_r \left[A_g \frac{U_L}{U_{g-a}} + A_{ag} \right] - U_L (T_f - T_a) \right\} \quad (5.5.19)$$

where $U_{g-a} = U_L$ has been introduced.

In order to maintain the simplicity of the Hottel-Whillier collector equation, the effective transmittance-absorptance product, $(\tau\alpha)_e$ must be defined for each of the three components of I_r as follows

$$(\tau\alpha)_e = (\tau\alpha) + A_g \frac{U_L}{U_{g-a}} + A_{ag} \quad (5.5.20)$$

where A_g and A_{ag} are found by means of the embedding technique. Figure 5.5.5 illustrates the difference between $(\tau\alpha)_e$ and $(\tau\alpha)$ versus incidence angle for an absorber plate temperature of $50^\circ C$.

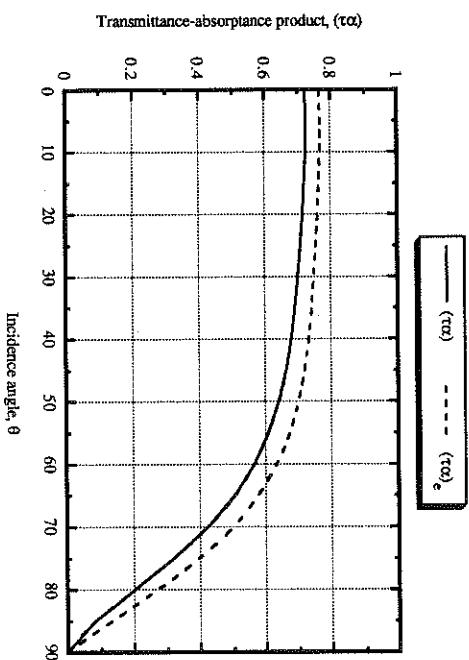


Figure 5.5.5 $(\tau\alpha)$ and $(\tau\alpha)_e$ versus incidence angle.

5.5.4 MSA Collector Performance

Equation 2.2.1 can be written in terms of an "instantaneous" efficiency as

$$\eta_i = \frac{Q_a}{A_c G_T} = F_R K_{\tau\alpha} (\tau\alpha)_e - F_R U_L \frac{(T_f - T_a)}{G_T} \quad (5.5.21)$$

The efficiency of the MSA collector shown in Figure 5.1.1 has been measured at the Thermal Insulation Laboratory in Denmark (Svendsen (1989)). The calculation procedure developed in this chapter has been compared with the Danish measurements under similar conditions. As shown in Figure 5.5.6 there is good agreement between the calculated and measured efficiency.

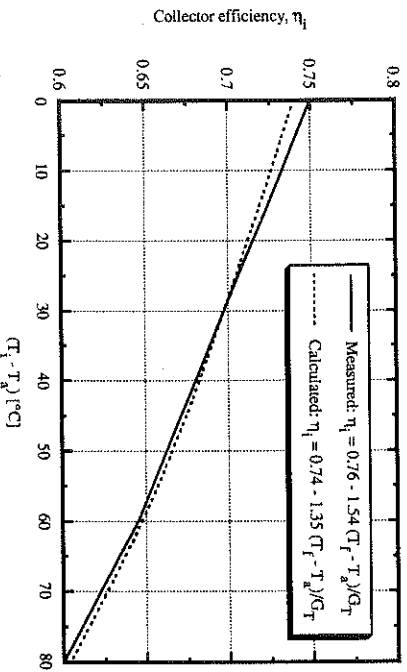


Figure 5.5.6 Comparison calculated versus measured efficiency curves.

The model underpredicts the heat loss coefficient with about 10% compared to the measurements. This was expected due to the deviations from the ideal preconditioning of MSA used in the collector as stated by Svendsen (1989). The predicted optical efficiency

is also lower than the measurements. This is related to the spectral extinction data used as input to the model. Due to lack of spectral measurements of the MSA (TMOS) used in the Danish collector, these data had to be developed from another type of MSA which is about 4% less transparent.

5.6 Comparison with Other Collector Designs

5.6.1 Collector Efficiencies

Instantaneous collector efficiencies are shown in Figure 5.6.1 for three different collector designs: (1) one cover with selective absorber plate ($\epsilon_g = 0.065$); (2) evacuated flat-plate collector (HVL 20); (3) MSA collector. For (1) and (3) $F_R(\tau\alpha)_e$ was 0.81 and 0.74, respectively, and U_L was calculated by using the method presented in Subsections 5.5.1 and 5.5.2. The data for (2) was given by the manufacturer [Kellner (1989)]. In all cases, the incident radiation on the collector was 800 W/m^2 .

It is clearly seen that considerable improvements of the efficiency can be obtained by using MSA collectors for high temperature applications. It is worth noticing that the efficiency is even better than the evacuated flat-plate collectors for temperature differences larger than about $65 \text{ }^\circ\text{C}$. Even if the thermal performance of one collector exceeds another collector over the actual temperature range for the application, cost of the two systems must be considered before a final judgment is possible.

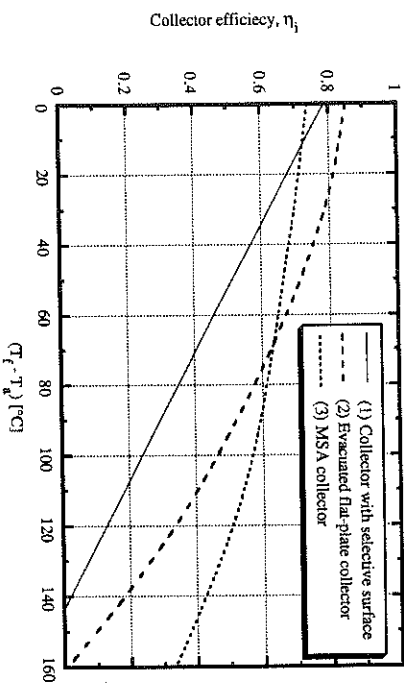


Figure 5.6.1 Collector efficiency as a function of the difference between collector fluid inlet temperature and ambient temperature.

5.6.2 Annual Performance

A single glazed flat-plate collector with selective coating characterized by $F_R(\tau\alpha)_e = 0.81$ and $F_R U_L = 4.2 \text{ W/m}^2\text{C}$ is used as a reference. When this collector is improved with the materials in Tables 2.4.1 and 2.4.2 or substituted with an equally sized MSA collector, the collector parameters and annual performances of Table 5.6.1 is obtained. The annual performances were obtained with TRNSYS for a process heating application at a minimum operating temperature of 75°C.

Table 5.6.1 Simulated yearly heat production at a minimum operating temperature of 75°C with collectors improved with different TIMs.

Collector type	$F_R(\tau\alpha)$	$F_R U_L$	Q_d [kWh/m ² year]
Selective coating (sc)	0.80	4.20	265
1-terfon film + sc	0.77	3.33	306
2-terfon films + sc	0.74	3.05	305
Corrugated-terfon film + sc	0.78	3.20	327
Arel-honeycomb. + sc	0.68	2.00	340
MSA	0.74	1.43	431

In Sweden large flat-plate collector areas are constructed for connection to district heating networks. These collectors are therefore required to operate at temperatures between 60 and 100°C. Up to now collectors with a single teflon film plus selective coatings has been the most feasible for this purpose [Karlsson (1988)]. The corrugated teflon film and the honeycomb increased the annual gain by 7 and 11%, respectively, but will not be used because of high installation costs. The MSA collector increased the yearly gain as much as 41%. In addition, selective coatings will be excessive which will reduce the costs. Today, MSA collectors are not yet commercial available and far to expensive. However, when MSA is mass produced and the MSA collector is fully developed it is expected that the collector will make a breakthrough possible for solar heating systems for medium and high temperature applications.

CHAPTER 6

System Simulation - Case Studies

6.1 Introduction

System simulation means observing a synthetic system that imitates the performance of a real system. There are two basic kinds of data that can be obtained from simulations. First, integrated performance over extended periods can be determined. Second, information on process dynamics is available.

In the following two sections a solar heating system and a solar air conditioning system have been simulated. The study was performed mainly to observe how thermal performance of solar heating and cooling systems are affected by flat-plate collectors based on monolithic silica aerogel (MSA), and partly to assess the feasibility of the systems under Norwegian climatic conditions.

6.2 A Heating System Simulation Study

6.2.1 System Description

Figure 6.2.1 is a schematic of a standard liquid based solar heating system. A collector heat exchanger is shown between the collector and storage tank, allowing the use of antifreeze solutions in the collector. Relief valves are shown for dumping excess energy

should the collector run at excessive temperatures. A load heat exchanger is shown to transfer energy from the tank to the heated spaces. Means of extracting energy for service hot water are also included. Auxiliary energy for heating is added so as to "top off" that available from the solar energy system.

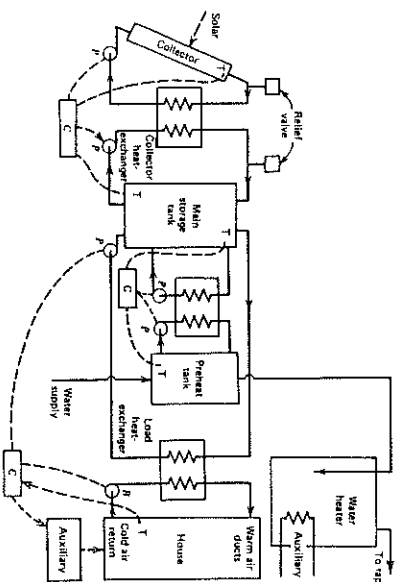


Figure 6.2.1 Detailed schematic of a liquid based solar heating system. P, pump; C, controller; T, temperature sensor; B, blower. Adapted from Duffie and Beckman (1980).

The load heat exchanger must be adequately designed to avoid excessive temperature drop and corresponding increase in tank and collector temperatures. The parameter describing this exchanger is $\epsilon_1 C_{min}/(UA)_h$, where ϵ_1 is the effectiveness of the heat exchanger, C_{min} is the lower of the two fluid capacitance rates in the heat exchanger, and $(UA)_h$ is the building overall energy loss coefficient area product.

6.2.2 System Simulation

System simulations were conducted for the solar heating system shown in Figure 6.2.1. The simulations were performed with TRNSYS [Klein et al. (1988)] using meteorological data for Oslo, Norway (59.9°N). The system is to provide space heating and hot water for a well insulated residence of 200 m² floor area. Internal heat generation, infiltration, ventilation and capacitance of the building are considered [(U/A)_b = 250 W/°C and (M_{Cp})_b = 40 MJ/°C]. The hot water demand is 300 liters/day, assumed distributed at 50°C through the day according to a normalized profile of hot water use for domestic application given in Duffie and Beckman (1980). The total load profile is shown in Figure 6.2.3

Two different collector designs were used in the simulation study: (1) MSA collector (illustrated in Figure 5.2.1), and (2) single glazed collector with selective absorber coating and a sheet of Teflon plastic between the glass and absorber plate to minimize convection losses [F_R ($\tau\alpha$) = 0.77 and $F_R U_L$ = 3.33 W/°C m²]. The liquid flowrate on both sides of the collector heat exchanger is 0.015 kg/m² s. Collector areas in the range of 10 to 80 m² were used in the simulations. The collector slope is 58° and surface azimuth angle is zero.

The heat exchanger effectiveness is 0.7 and the specific heat of the antifreeze solution is 3800 J/°C kg (ethylene glycol). The storage tank is sized so that its capacity is at a fixed ratio to the collector area, at 75 kg/m². The loss coefficient of the storage tank is 0.40 W/°C m², and losses from the storage are to a 20°C environment. To show the effects of storage tank size, simulations were done at 50, 100, and 200% of the nominal size, for collector areas of 10, 30, and 60 m². The heating system is controlled as shown in Figure 6.2.1 to keep the building near 20°C. The volume of the preheat tank is 0.4 m³, and its loss coefficient is 0.5 W/°C m².

Figure 6.2.2 shows the annual solar fraction for the two collector types as a function of collector area, for normal storage volume to collector area ratio (75 liters/m²), and also points for larger and smaller storage capacities for the 10, 30 and 60 m² collector areas.

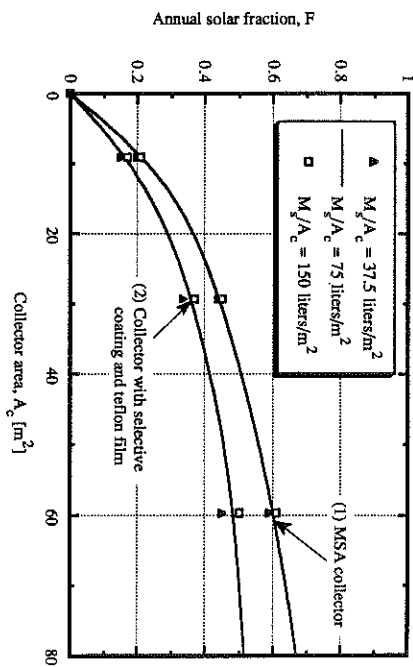


Figure 6.2.2 Annual solar fraction for two collector designs as a function of collector area at different storage volume to collector area ratio. (1) MSA collector; (2) Collector with selective coating and Teflon film.

These are typical curves for space heating, in that the slope is significantly higher for small collector areas than for large collector areas. The larger collectors are oversized a greater part of the year than are the small collectors. The MSA collector increased annual solar outputs by about 25 to 30% compared to the other collector included in this study. The effects of change of storage size are small for the collector areas considered.

Figure 6.2.3 indicates the monthly load profile and the monthly solar contributions for the two collector types at $A_c = 10$ and 30 m^2 for the normal storage volume to collector area ratio.

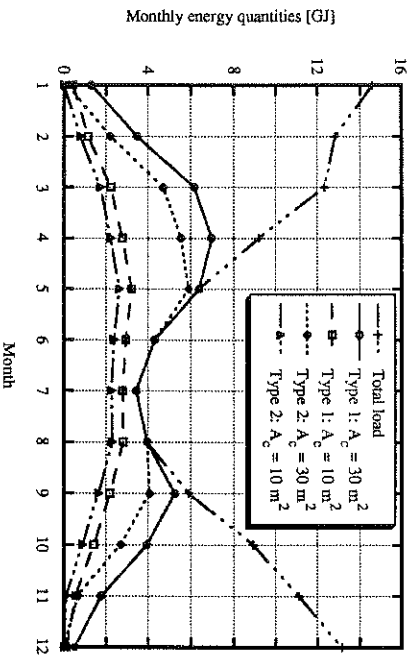


Figure 6.2.3 Monthly load profile and monthly solar contribution for two collector types at $A_c = 10$ and 30 m^2 . (1) MSA collector; (2) Collector with selective coating and Teflon film.

Generally, the MSA collector improves monthly system performance. The largest systems will carry the summer loads, while the smallest has a solar fraction of about 60 and 70 % in the summer months, depending on the collector type. Due to the very low radiation intensity in the winter months, the solar contributions are almost zero at this time of year. During spring and fall the solar contributions are higher, between 20 and 50 % depending on month and collector type.

As the heating season is longer in the northern part of Norway, it is suggested that active solar heating should be more feasible in this part of the country than in southern Norway. A similar analysis for Tromsø (69.7° N) verified this statement, and showed that the solar output was 10 % higher than in the Oslo simulation.

In order to assess the most optimal design (i.e., collector area) for the Oslo climate, an economical analysis was performed. MSA collectors are not commercially available, and were not included in the economical analysis. The very nature of most of the parameters involved, however, renders such economic analysis to a large extent of uncertainty because of the difficulty to predict the future from past and present trends.

The economic parameters assumed are: term of analysis is 20 years; discount rate is 9 %/year; general inflation rate is 7 %/year; auxiliary energy costs is 0.45 NOK/kWh; total collector area dependent costs is 1800 NOK/ m^2 ; total cost of equipment which is independent of collector area is 15000 NOK. Applying these economic assumptions together with the calculated thermal performance of the system, Figure 6.2.4 was produced. It is seen that the optimum collector area is around 23 m^2 . The corresponding annual solar fraction is 31%.

The results shown in Figure 6.2.4 is for a specific set of economic assumptions. Therefore sensitivity analysis should effectively be done for every economic parameter, since most of them are projected estimates and may turn out to be inaccurate. However, it is important to stress that, while designing solar thermal systems in view of all the uncertainties associated with the system and economic parameters, it is redundant from a practical viewpoint to strive for a very accurate determination of the annual solar fraction of the solar system.

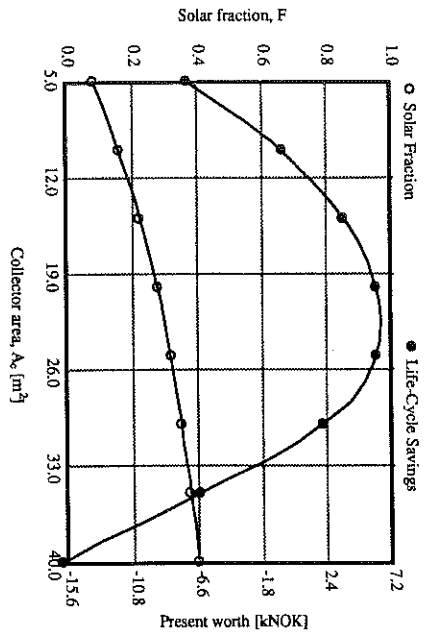


Figure 6.2.4 Life cycle solar savings for the Oslo simulation. The solar fractions are also included.

6.3 A Simulation Study of Solar Air Conditioning

Solar air conditioning represents a potentially significant application of solar energy in most sunny regions of the world. Solar air conditioning is one of the most fitting application of solar energy since the demand for cooling occurs mostly at the time when solar energy is available. For both daily and seasonal variations these two factors are in phase. The combination of solar cooling and heating should improve the economics compared to heating alone [Duffie and Beckman (1980)].

Solar air conditioning was originally developed for hot climate zones, where the amount of electrical energy required for providing air conditioning can be significant. However, commercial buildings in high-latitude cool climates may have a significant cooling load due to solar radiation and internal heat generation. In this study only solar absorption air conditioning will be considered.

6.3.1 System Description

Figure 6.3.1 shows the configuration of the combined solar heating and Li-Br-H₂O absorption air conditioning system investigated in this study. A mixture of Li-Br and H₂O is heated in the generator G using solar energy. The pressure rises and the Li-Br loses most of the water in the form of steam. The water vapor then travels at constant pressure to the condenser C where the pressure becomes low. Heat is extracted from the condenser by passing cold water heat exchange through it. The remaining water vapor in the condenser is now totally changed to water which is fairly cool and now the pressure is allowed to drop further to let this cool water evaporate in the evaporator E and thus extract the heat of evaporation from circulating cold water exchange thus chilling it. The refrigerant becomes partially vapor with higher pressure and flows due to gravity, from the generator on the high pressure side to the low pressure side into the absorber passing through heat exchanger HX where it gives most of its heat to the mixture which is flowing to the generator. The concentrated Li-Br mixes with the water in the absorber and flows to the generator to repeat the cycle.

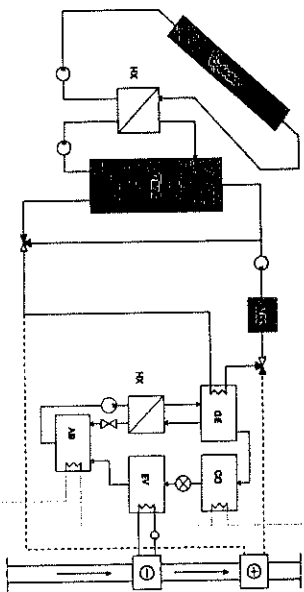


Figure 6.3.1 Schematic of a combined solar heating and air conditioning system using a Li-Br-H₂O absorption cycle.

At present the COP (ratio of cooling capacity to thermal input) of commercial absorption systems is relatively low (about 0.7) and the cost of the equipment (collectors and chiller) is very high, and thus these systems cannot compete economically with conventional air conditioners.

6.3.2 System Simulation

The commercial building analyzed in this work needs auxiliary heating from October to the beginning of May. In the summertime, the abundant sunshine causes mainly only a cooling load. Simulations were performed for the combined solar heating and air conditioning system shown in Figure 6.3.1 using meteorological data for Hamar, Norway (61 °N). The results are based on detailed performance predictions with TRNSYS [Klein et al. (1988)].

The office building simulated has a floor area of 750 m² and consists of 3 zones. Zone 2 is semi-climatized in shape of a glazed space placed in between the fully climatized zones. The relevant parameters for the office building as well as the simulated solar energy system are shown in Table 6.3.1.

The energy balance of the office building were obtained by an accurate building energy analysis program DEBAC (Harsen and Bøtressen, 1985). The resulting load profiles are shown in Figure 6.3.2. The desired room temperature range is 20 to 23 °C. The minimum useful source temperature for space heating and cooling are 30 and 80 °C respectively. The simulation study involves two collector types: (1) MSA collector (illustrated in Figure 5.2.1), and (2) single glazed collector with selective absorber coating and a sheet of Teflon plastic between the glass and absorber plate to minimize convection losses [$F_R(\tau\omega) = 0.77$ and $F_R U_L = 3.33 \text{ W/C m}^2$].

Table 6.3.1 Simulation parameter values.

Office building	Time of operation		
	Zone 1	Zone 2	Zone 3
Ventilation [m ³ /hr]	Mon. - Fri. 07-19 1580	1350	2150
(Inlet temperature = 15 °C)	Sat. - Sun.	0	0
Heat generation [W]	Mon. - Fri. 07-19 8300	7700	7600
(equipment, lighting, and persons)	Sat. - Sun.	3000	3000
Transmission losses [W/C]	187	351	177
Infiltration losses [W/C]	36	105	45
<i>Solar system</i>			
Solar collector flow rate m/A _c	0.015 kg/m ² s		
Storage tank size collector area ratio	100 kg/m ²		
M _g /A _c	Optimal = 58 °		
Solar collector slope β	Optimal = 58 °		
<i>Air conditioning system</i>			
Type	Atkila model WF-36		
Absorption chiller capacity P	8 kW		
Start up time constant τ _s	480 s		
Cool down time constant τ _{cd}	3780 s		
Condenser inlet temperature T _c	20 °C		

Figure 6.3.3 shows the variation of the fractions of the monthly energy needs (for heating and cooling) met by this system for the two collector types at A_c = 50 and 100 m². In this climate, the annual solar fraction reaches 33% and 54% for the two collector types at a collector area of 100 m² in the particular year used in this simulation.

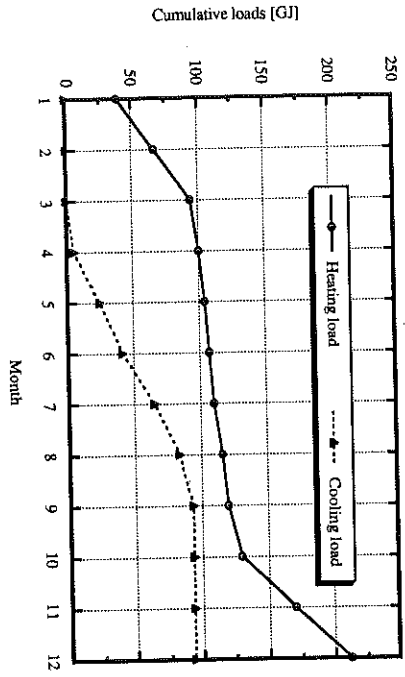


Figure 6.3.2 Cumulative loads for the Hammar simulations.

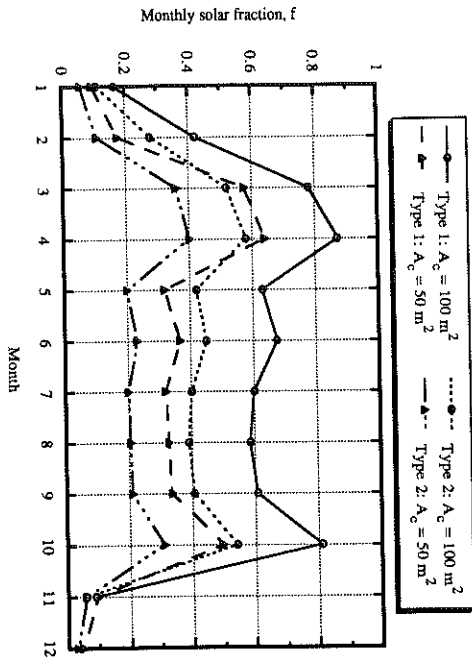


Figure 6.3.3 Monthly fractions of loads met by solar energy for the two collector types at $A_c = 50$ and 100 m^2 . (1) MSA collector; (2) Collector with selective coating and Teflon film.

The inability of the system to meet summer cooling loads is evident. However, the MSA collector greatly improves system performance. At a collector area of 100 m^2 the annual solar output was increased by 65 GJ or about 60 % as much as the other collector type.

When the MSA collector is fully developed, it is expected that it will make a breakthrough possible for solar heating systems for medium and high temperature application. Future uses of solar absorption machines will not only depend on cost-effective high temperature collectors but a corresponding development of advanced cycles will be required. Double effect machines (the refrigerant is boiled off in a two stage process partly using solar energy and partly using the heat of condensation of the vapor) can achieve a COP in the range of 1.25 to 1.5.

CHAPTER 7

Future Research Suggestions

The solar radiation and infrared heat transfer in monolithic silica aerogel (MSA) has been successfully modelled. As pointed out earlier on in this thesis measurements concerning the spectral transmittance values in the solar part of the spectrum for MSA are lacking. Accurate data are difficult to obtain due to scattering. Nevertheless, measurements and characterization of MSA together with further verification of the mathematical models are vital for future development of less expensive and more transparent samples.

Flat-plate collectors can be greatly improved by using MSA as a part of the cover glazing. With a 4 mm thick glass plate and a 20 mm thick MSA tile, the losses from the cover glazing can be significantly reduced, resulting in a doubling of the collector efficiency at typical operating conditions. However, Svendsen (1989) has reported some problems concerning the construction of MSA collectors. Future studies should therefore focus on designing and testing prototypes to achieve more durable and reliable MSA collectors.

Transient collector response has been theoretically investigated. Transient effects are often negligible. However, situations where transient effects reduce the collector performance has been identified. Future experimental studies should investigate to what extent the transient collector operation reduces the long-term average performance.

The storage tank stratification significantly increases the solar thermal system performance, but appears to have only a small effect on the collector performance. The cause for the increase of the solar system performance due to storage tank stratification is

the load withdrawal from the top of the tank. Mixing of the hot fluid in the top of the storage tank with the cold fluid in the bottom of the tank can reduce the performance of a solar thermal system. Storage tank designs that reduce the effect of mixing should be investigated.

Hourly solar radiation models were presented and evaluated. These models need hourly values of horizontal global radiation as input, and a forcing function for the synthetic generation of solar radiation would be very time saving and therefore desired. Future research in this area should focus on development of reliable synthetic radiation models.

References

- J. I. Ajona and J. M. Gordon, An analytic model for the long-term performance of solar airheating systems. *Solar Energy* 38, 45-53 (1987).
- ASHRAE Standard 93-77, Methods of Testing to Determine the Thermal Performance of Solar Collectors. *ASHRAE*, New York (1977).
- ASHRAE Handbook-HVAC Systems and Applications. *ASHRAE* 47.1-47.28, Atlanta (1987).
- W. A. Beckman, Solution of Heat Transfer Problems on a Digital Computer. *Solar Energy* 13, 293-300 (1971).
- W. A. Beckman, Duct and Pipe losses in solar energy systems. *Solar Energy* 21, 531-532 (1978).
- R. E. Bird and R. L. Hulstrom, *Direct Insolation Models*. SER/TR-335-344, Golden, CO (1981).
- M. J. Brandemuehl and W. A. Beckman, Transmission of Diffuse Radiation Through CPC and Flat-Plate Collector Glazings. *Solar Energy* 24, 511 (1980).
- J. E. Braun, S. A. Klein and K. A. Pearson, An improved design method for solar water heating systems. *Solar Energy* 31, 597-604 (1982).
- R. Cays and J. Fricke, Infrared radiative heat transfer in highly transparent silica aerogel. *Solar Energy* 16, 361-364 (1986).
- M. Collares-Pereira and A. Rabl, Derivation of method for predicting long-term average energy delivery of solar collectors, and Simple procedure for predicting long-term average performance of nonconcentrating and concentrating solar collectors. *Solar Energy* 23, 223-254 (1979).
- G. F. Cotton, ARL Models of Global Solar Radiation. *SOLMET 2: Hourly Solar Radiation- Surface Meteorological Observations*. TD-9724, F. T. Quinlan (Ed.), Asheville, NC (1979).
- J. A. Duffie and W. A. Beckman, *Solar Engineering of Thermal Processes*. Wiley-Interscience Publication, New York (1980).
- D. K. Edwards, I. Canton, Prediction of heat transfer by natural convection in closed cylinders heated from below. *Int. J. Heat Mass Transfer* 12, 23-30 (1969).
- D. K. Edwards, Solar absorption by each element in an absorber-coverglass array. *Solar Energy* 19, 401-402 (1977).
- D. G. Ertis, S. A. Klein and J. A. Duffie, Estimation of the diffuse fraction for hourly, daily and monthly-average global radiation. *Solar Energy* 28, 293-302 (1982).
- L. B. Evans, C. M. Chu and S. W. Churchill, The effect of anisotropic scattering on radiant transport. *ASME Journal of Heat Transfer*, 381-387 (1965).
- D. Feuermann, J. M. Gordon and Y. Zarmi, A typical meteorological day (TMD) approach for predicting the long-term performance of solar energy systems. *Solar Energy* 35, 63-69 (1985).
- G. E. Forsythe, M. A. Malcolm and C. B. Moler, *Computer Methods for Mathematical Computations*, Prentice-Hall, Englewood Cliffs, N. J. (1977)
- J. Fricke (Ed.), *Aerogels, Springer Proceedings in Physics* 6, Springer-Verlag (1986).
- V. A. Graham, K. G. T. Hollands and T. E. Unny, A time series model for Kt with application to global synthetic weather generation. *Solar Energy* 40, 83-92 (1988).

- J. M. Gordon and Y. Zarmi, An analytic model for the long-term performance of solar thermal systems with well mixed storage. *Solar Energy* 35, 55-61 (1985).
- J. E. Hay and J. A. Davies, Calculation of the solar radiation incident on an inclined surface. *Proceedings First Canadian Solar Radiation Data workshop*, 55-72 (1980).
- K. G. T. Hollands, Honeycomb devices in flat-plate solar collectors. *Solar Energy* 9, 159-164 (1965).
- C. J. Hoogendoorn, Natural convection suppression in solar collectors. Natural Convection, S. Kakac (Ed.), 940-960, Hemisphere Publishing Corporation (1985).
- H.C. Hotel and B. B. Woertz, Performance of flat-plate solar heat collectors. *Trans. ASME* 64, 91-103 (1942).
- H. C. Hotel and A. Whillier, Evaluation of flat-plate collector performance. *Trans. of the Conference on the Use of Solar Energy, The Scientific Basis II*, Part I, Section A 77-104 (1955).
- H. C. Hotel, and A. F. Sarofim, *Radiative Transfer*. McGraw-Hill, New York (1967).
- J. R. Howell, R. B. Bannrot and G. C. Vliet, *Solar-Thermal Energy Systems: Analysis and Design*. McGraw-Hill, New York (1982).
- R. L. Hulstrom (Ed.), *Solar Resources*. The MIT Press, Cambridge, Ma (1989).
- M. Iqbal, *An Introduction to Solar Radiation*. Academic Press, New York (1983).
- K. I. Jensen, *Transparent Cover with Evacuated Silica Aerogel*, Thermal Insulation Laboratory, Technical University of Denmark (1989).
- L. F. Jesch and J. E. Braun, Variable volume storage and stratified storage for improved water heater performance. *Solar Energy* 29 (1984).
- J. Jimenez-Fernandez, A useful recipe for the solar collectors response time. *Solar Energy* 34, 427-428 (1985).

- C. L. Gardner and C. A. Nadeau, Estimating south slope irradiance in the arctic - a comparison of experimental and modeled values. *Solar Energy* 41, 227-240 (1988).
- T. Harsen and B. Børesen, *DEBAC - Program for beregning av klima, effekt, energi og driftforhold i bygninger*. STF15 A85050, SINTEF, Norway (1985)
- S. Henning and L. Svensson, Production of Silica aerogel. *Physica Scripta* 23, 697-702 (1981).
- B. Karlsson, Potential improvements for high temperature flat-plate collectors. *North Sun 1988*, Borlänge Sweden (1988).
- B. Karlsson, Transparent insulation for high temperature flat-plate collectors. *North Sun 1988*, Borlänge Sweden (1988).
- B. Kellner, Erste deutsche Grossserien-Fertigung von Hochleistungs-Kollektoren. *Sonnenergie & Wärmepumpe* 14, Heft 3 (1989).
- K. Kimura and D. G. Stephenson, Solar Radiation on Cloudy Days. *ASHRAE Transactions* 75, 227-234 (1969).
- S. A. Klein, J. A. Duffie and W. A. Beckman, Transient considerations of flat-plate collectors. *Journal of Engineering for Power* 96A, 109 (1974).
- S. A. Klein, W. A. Beckman and J. A. Duffie, *Heating Design by the f-chart Method*. Wiley-Interscience Publication, New York (1977).
- S. A. Klein, Calculation of flat-plate collector utilizability. *Solar Energy* 21, 393-402 (1978).
- S. A. Klein, J. A. Duffie and W. A. Beckman, Transient considerations of flat-plate collectors. *Journal of Engineering for Power* 96A, 109 (1979).
- S. A. Klein, Scientific versus correlation methods. *10th ISES Solar World Congress*, Paper 8.W4.02, Hamburg (1987).

- S. A. Klein et al., *TRANSYS - A Transient Simulation Program*. University of Wisconsin - Madison, Engineering Experiment Station Report 38-12, version 12.2 (1988).
- T. M. Klucher, Evaluation of models to predict insolation on tilted surfaces. *Solar Energy* 23, 111-114 (1979).
- K. Kollsaaker, F. Frydenlund og G. Bratsberg, *FRES - Fleksibel Romklima- og Energisimulator*. STF15 A90025, SINTEF, Norway (1990)
- K. Y. Kondrayev, *Radiation in the Atmosphere*. Academic Press, New York (1969).
- J. F. Kreider, C. J. Hoogendoorn, and F. Kreith, *SOLAR DESIGN Components, systems, Economics*. Hemisphere Publishing Corporation, New York (1989).
- B. Y. H. Liu and R. C. Jordan, The interrelationship and characteristic distribution of direct, diffuse and total solar radiation. *Solar Energy* 4, 1-19 (1960).
- B. Y. H. Liu and R. C. Jordan, A rational procedure for predicting the long-term average performance of flat-plate solar energy collectors. *Solar Energy* 7, 53-70 (1963).
- B. H. J. McKellar and M. A. Box, The Scaling Group of the Radiative Transfer Equation. *Journal of the Atmospheric Sciences* 38, 1063-1068 (1981).
- L. J. B. McArthur and J. E. Hay, A technique for mapping the distribution of diffuse solar radiation over the sky hemisphere. *Journal Applied Meteorol.* 20, 421-429 (1981).
- B. A. Meyer, J. W. Mitchell and M. M. El-Wakil, Natural convection heat transfer in moderate aspect ratio enclosures. *ASME Journal heat transfer* 101, 655-659 (1979).
- A. Nordgaard, R. G. Haland and e. Rødahl, predicted Thermal Performance of an Active Solar Heating System in Norway by Different Methods of calculating the Slope Irradiance. *11th ISES Solar World Congress*, Kobe (1989).
- J. F. Orgill and K. G. T. Hollands, Correlation equation for hourly diffuse radiation on a horizontal surface. *Solar Energy* 19, 357 (1977).

- S. V. Patankar, *Numerical Heat Transfer and Fluid Flow*. Hemisphere Publishing Corporation (1980).
- R. Perez, R. Seals, P. Ineichen, R. Stewart, and D. Menicucci, A new simplified version of the Perez diffuse irradiance model for tilted surfaces. *Solar Energy* 39, 221-231 (1987).
- R. Perez, R. Seals, A. Zelenka and P. Ineichen, Climatic evaluation of models that predict hourly direct irradiance from hourly global irradiance: Prospects for performance improvements. *Solar Energy* 44, 99-108 (1990).
- W. F. Phillips and R. N. Dave, Effects of stratification on the performance of liquid based solar heating systems. *Solar Energy* 29 111-120 (1982).
- W. Platzer, Solar transmission of transparent insulation material. *Solar Energy Materials* 16, 275-287 (1987).
- W. Platzer, Utilization of Heat Gains from Transparently Insulated Collector-Storage Walls. *10th ISES Solar World Congress*, Hamburg (1987).
- T. A. Reddy, J. M. Gordon and J.P.D DeSilva, Mira: A one-repetitive day method for predicting the long-term performance of solar energy systems. *Solar Energy* 39, 123-133 (1987).
- T. A. Reddy, *The design and Sizing of Active Solar Thermal Systems*. Oxford Science Publications, Oxford (1987)
- D. T. Reindl, *Estimating diffuse radiation on horizontal surfaces and total radiation on tilted surface*. MS Thesis, University of Wisconsin-Madison, Madison, WI (1988).
- N. Robinson (Ed.), *Solar Radiation*. American Elsevier, New York (1966).
- M. Rubin and C. M. Lampert, Transparent silica Aerogels for Window Insulation. *Solar energy Materials* 7, 393-400 (1983).

- P. Scheufling, R. Caps, D. Bütner and J. Fricke, Apparent thermal conductivity of evacuated SiO₂-aerogel tiles under variation of radiative boundary conditions. *Int. J. Heat Mass Transfer* 28, 2299-2306 (1985).
- Siegel, R., and Howell, J. R., *Thermal Radiation Heat Transfer*. McGraw-Hill, New York (1981).
- A. Skarveit, *Energy exchange at the earth's surface with emphasis on an alpine tundra ecosystem*. Report 1976:1 From The High Mountain Ecology Research Station, Finse, Norway (1976). (1976).
- A. Skarveit and J. A. Oiseh, Modelling slope irradiance at high latitudes. *Solar Energy* 36, 271-274 (1986).
- A. Skarveit and J. A. Oiseh, A model for the diffuse fraction of hourly global radiation. *Solar Energy* 38, 271-274 (1987).
- Solar Energy Research Institute (SERI), *Insolation Assessment Studies Progress Report: FY 1982/83*. SERI/PR-215-2214, Golden, CO: SERI (1984).
- H. Soltau, The Thermal Performance of Uncovered Collectors. *10th ISES Solar World Congress*, Paper No. 2.5.14, Hamburg (1987).
- A. F. Souka and H. H. Safwat, Optimum orientations for the double exposure flat-plate collector and its reflectors. *Solar Energy* 10 170 (1966).
- H. Stuehcke and P. G. McCormick, Collector Utilizability for Instantaneous Solar Radiation. *10th ISES Solar World Congress*, Paper No. 2.2.22, Hamburg (1987).
- S. Svendsen and K. I. Jensen, Flat-plate solar collector with monolithic silica aerogel. *10th ISES Solar World Congress 1987*, Paper No. 2.2.3, Hamburg (1987).
- S. Svendsen, Solar collector based on monolithic silica aerogel. *11th ISES Solar World Congress 1989*, Kobe (1989).
- J. G. Symons and M. K. Peck, An overview of the CSIRO project on advanced flat-plate solar collectors. *Proc. Sol. World Forum*, 748-752, Perth (1983).

- J. G. Symons, Calculation of the transmittance-absorptance product for flat-plate collectors with convection suppression devices. *Solar Energy* 38, 637-640 (1984).
- R. C. Temps and K. I. Coulson, Solar radiation incident upon slopes of different orientations. *Solar Energy* 19, 179 (1977).
- P. H. Tewari, A. J. Hunt, J. G. Lieber and K. Loffus, Microstructural Properties of transparent Silica Aerogels, Aerogels, *Springer Proceedings in Physics* 6, J. Fricke (Ed.), Springer-Verlag (1986).
- W. B. Velkamp, Thermal stratification in heat storage. *Proceedings of an international TNO-Symposium - Thermal storage of solar energy*, 47-60, Martinus Nijhoff Publishers, The Haag (1980).
- R. Viskanta, Heat transfer by conduction and radiation in absorbing and scattering materials. *ASME Journal of Heat Transfer*, 143-150 (1965).
- A. Whillier, *Solar energy collection and its utilization for house heating*. Ph.D thesis, MIT, Cambridge, Ma. (1953).
- J. A. Wiebelt and J. B. Henderson, Selected ordinates for total solar radiation property evaluation from spectral data. *Transactions ASME Journal of Heat Transfer* 101, 101 (1979).
- N. E. Wijesundera, Comparison of transient heat transfer models for flat-plate collectors. *Solar Energy* 21, 517-521 (1978).
- V. Witwer and W. Stahl, Heat loss Mechanisms in Transparent Insulation with Honeycomb Structures. *Proc. SPIE Conference 428*, San Diego (1983).
- World Commission on Environment and Development, *Our common future*. Oxford University Press, Oxford (1987).
- M. D. Wuestling et al., Promising control alternatives for solar water heating systems. *Trans. ASME J. Solar Energy Engng* 107, 215 (1985).

Nomenclature

A _c	collector area [m ²]
A _i	areas for heat loss of the inlet duct [m ²]
A _o	areas for heat loss of the outlet duct [m ²]
α/c	weighted circumsolar solid angle
α/c	incidence angle modifier coefficient
C ₁ , C ₂	Planck's first and second radiation constants
C _p	specific heat of medium in the storage tank [J/kg°C]
CCF	cloud cover factor
D	particle diameter, tube diameter [m]
E _d (x)	third exponential integral
E _{sb}	Planck's spectral distribution of emissive power
F	annual solar fraction, standard fin efficiency
F _r	collector heat removal factor
F'	collector efficiency factor, reduced brightness coefficients
F _{ij}	direct exchange factor
\hat{F}_{ij}	total exchange factor
f	monthly solar fraction
G _e	solar constant = 1367 W/m ²
G _{on}	extraterrestrial radiation normal to the sun's beam [W/m ²]
G _r	instantaneous radiation on the collector surface [W/m ²]
\bar{G}_r	monthly average daily radiation incident on the collector surface [J/m ²]
h _w	wind heat transfer coefficient [W/m ² °C]
I	total heat transfer coefficient [W/m ² °C]
I _b	hourly total radiation on a horizontal surface [W/m ²]
I _{bn}	hourly beam radiation on a horizontal surface [W/m ²]
I _{bn}	hourly beam radiation at normal incidence [W/m ²]
I _{bT}	hourly beam radiation on a tilted surface [W/m ²]
I _d	hourly clear sky radiation on a horizontal surface [W/m ²]
I _{dT}	hourly diffuse radiation on a horizontal surface [W/m ²]
I _{dT}	hourly diffuse radiation on a tilted surface [W/m ²]
I _{g,T}	hourly ground reflected radiation on a tilted surface [W/m ²]
I _o	hourly extraterrestrial radiation on a horizontal surface [W/m ²]

I _{on}	hourly extraterrestrial radiation at normal incidence [W/m ²]
I _r	hourly radiation on the collector surface [W/m ²]
I _{r,c}	hourly critical radiation level on a tilted surface [W/m ²]
i _a	directional monochromatic radiation intensity
i _b	monochromatic intensity of emitted energy of the particles from Planck's distribution
K _{a,λ}	monochromatic absorption coefficient [1/m]
K _{s,λ}	monochromatic scattering coefficient [1/m]
K _{t,λ}	monochromatic total extinction coefficient [1/m]
K _{τα}	incidence angle modifier
k	thermal conductivity [W/°C m]
k _{app}	apparent thermal conductivity [W/°C m]
k _a	hourly cleanliness index
L	monthly load for space heating, hot water [J], slab thickness [m]
m	mass of medium in the storage tank [kg]
ln(C)	heat capacity [kJ/°C]
(m C _p)	fluid capacitance rate [kJ/°C s]
N	conduction radiation parameter, number of days in the month
n	day number, index of refraction
P _p	pore pressure [bar]
Q _a	actual useful collector energy gain [W]
Q _i	the instantaneous heat load [W]
q _r	radiative heat flux [W/m ²]
R	heat transfer resistance
R _b	geometric factor for beam radiation
S	absorbed solar radiation [W/m ²]
s	pathlength [m]
T _i	the fluid inlet temperature [°C]
T _a	ambient air temperature [°C]
T _{a'}	temperature of the ambient air around the storage tank [°C]
\bar{T}_a	monthly average ambient temperature [°C]
T _c	cover temperature [°C]
T _{fm}	mean fluid temperature [°C]
T _p	absorber plate temperature [°C]
T _r	average radiative temperature [°C]
T _{ref}	empirically derived reference temperature (100 °C)
T _s	uniform storage tank temperature [°C]
T _{sky}	sky temperature [°C]
t	time [s]

U	internal energy [W/m ³]
U _L	collector overall heat loss coefficient [W/m ² °C]
U _d	loss coefficient from the duct [W/m ² °C]
(U/A) _s	storage tank loss coefficient-area product [W/°C]
V	volume [m ³]
W	mechanical work [W/m ²], distance between two collector tubes [m]
X _c	hourly critical radiation ratio
Z _e	factor describing diffuse radiation from zenith

Greek Symbols

α	absorptance, solar altitude angle, void fraction of air
β	surface slope
Δ	sky brightness parameter
Δτ	number of seconds in the month
ε	heat exchanger effectiveness, emittance, sky clearness parameter, truncation error
η	efficiency
κ	optical depth
K _D	optical thickness
θ	angle of incidence
θ _z	zenith angle
λ	wavelength [μm]
ρ	reflectance
ρ _g	ground reflectance
σ	Stefan-Boltzmann constant
(τα)	transmittance-absorptance product
τ _a	anisotropy index
τ	transmittance, collector time constant [minutes]
φ	hourly utilizability
φ	phase function
ω	hour angle, solid angle
Ω	albedo for scattering

Subscripts

a	ambient air
b	beam, bottom
c	collector side of the heat exchanger, cover
d	diffuse
e	effective, edge
f	fluid
i	inside
p	absorber plate
s	surface
sol	solar part of the spectrum
t	top
v	volume

Solar Radiation Principles

Several parameters have been mentioned in the main body of the thesis without the necessary formulas or background being given to evaluate them. They are included here for completeness. Unless specifically cited, the definitions and equations presented have been taken from Duffie and Beckman (1980).

A.1. Definitions and Formulas

Chapter 2 introduced solar radiation correlations. The hourly clearness index, k_T was needed to estimate the hourly diffuse fraction. The hourly clearness index is given by,

$$k_T = \frac{I}{I_0} \quad (A.1)$$

where I is the hourly radiation on a horizontal surface, and I_0 is the hourly extraterrestrial radiation on a horizontal surface. The integrated hourly extraterrestrial radiation on a horizontal surface is computed by the following relationship,

$$I_0 = \frac{12 \times 3600}{\pi} G_{sc} \left[1 + 0.033 \cos \left(\frac{360n}{365} \right) \right] \times \left[\cos(\phi) \cos(\delta) (\sin(\omega_1) - \sin(\omega_2)) + \frac{2\pi(\omega_2 - \omega_1)}{360} \sin(\phi) \sin(\delta) \right] \quad (A.2)$$

where G_{sc} is the solar constant (a value of 1367 W/m^2 has been used in this research), n is the day of the year, ϕ is the site latitude. The declination, δ , is the angular position of the sun at solar noon with respect to the equator plane, and is given by Lysstad (1980):

$$\delta = 23.45 \cos \left(\frac{360}{365} (172 - n) \right) \quad (A.3)$$

ω_1, ω_2 are hour angles (that is, the angular displacement of the sun east or west of the local meridian due to rotation of the earth on its axis at $15^\circ/\text{hr}$, ω_2 is larger, morning negative, afternoon positive).

The time specified by the hour angle is the solar time. The solar time differs from the local standard time for two reasons. First, there is a constant correction for the difference in longitude between the local meridian, L_{loc} , and the meridian on which the local standard time is based, L_{std} . The second reason is due to changes in the rotational and orbital angular speed of the earth, and can be expressed as

$$E = 9.87 \sin \left(2 \cdot \frac{360}{364} (n - 81) \right) - 7.53 \cos \left(\frac{360}{364} (n - 81) \right) - 1.5 \sin \left(\frac{360}{364} (n - 81) \right) \quad (A.4)$$

Solar time is related to standard time by

$$\text{Solar time} = \text{Standard time} + 4(L_{loc} - L_{std}) + E \quad (A.5)$$

where L_{loc} is given in degrees west.

The angle of incidence, θ_i , is required for tilted surface calculations, and is given as follows:

$$\begin{aligned} \cos \theta_i &= \sin b \sin \phi \cos \beta - \sin b \cos \phi \sin \beta \cos \gamma \\ &+ \cos b \cos \phi \cos \beta \cos \omega \\ &+ \cos b \sin \phi \sin \beta \cos \gamma \cos \omega \\ &+ \cos b \sin \beta \sin \gamma \sin \omega \end{aligned} \quad (A.6)$$

where β is the surface slope, γ is the surface azimuth angle, with zero due south, east negative, and west positive. For this study, the angle of incidence was evaluated at the midpoint of the time interval by using the hour angle, calculated at the midpoint of the time interval.

When the surface slope is zero, the angle of incidence is the zenith angle of the sun, θ_z . Equation A.6 becomes

$$\cos \theta_z = \cos b \cos \phi \cos \omega + \sin b \sin \phi \quad (A.7)$$

The zenith angle is related to the solar altitude angle, α , by the following expression:

$$\alpha = 90^\circ - \theta_z \quad (A.8)$$

Errata:

Page # Correction

- 9, line 1 ... Equation 2.2.5 ...
- 9, line 4 ... = (m C_p) (T_i, m)
- 9, line 10 ... is the effective fluid capacitance rate ...
- 9, line 11 $\phi = \frac{1}{N} \sum_{i=1}^N \frac{I_T}{(I_T - I_{T,c})^2}$
- 14, Equation 2.2.15 ... + 0.0018X² + ...
- 18, Equation 2.3.1 $G_{on} = G_{sc} \left(1 + 0.033 \cos \frac{365}{2\pi m} \right)$
- 50, line 1 Equation 2.2.9 shows ...
- 53, Equation 3.4.2 - (UA)_s T_a' should be + (UA)_s T_a'
- 66, Equation 4.2.2 CCF = P + S OPQ - R OPQ²
- 87, Equation 5.2.10 Subscript e should be v.
- 88, Equation 5.2.13 Subscript e should be v.
- 99, Figure 5.3.1 Text should be "Internal pore pressure, P_p [bar]"
- 104, line 6 Equation 5.2.10 and 5.3.5 are ... in Equation 5.3.5 ...
- 104, line 7 ... in Equation 5.2.10 ...
- 108, Equation 5.3.18 $q_{tot} = - \left(k \frac{dT}{dx} \right)_{x=0} + \epsilon_1 A_1 \sigma T_{s1}^4 - \epsilon_1 \sum_{k=1}^2 \epsilon_k A_k \sigma T_{sk}^4 F_{sk,s1} - \epsilon_1 \sum_{k=1}^n \epsilon_k A_k \Delta V_k \sigma T_{vk}^4 F_{vk,s1}$
- 114, line 1 ... Section 5.2.4 ...
- 115, Equation 5.4.6 $q^{d_{n+1}} = R_s^{n+1}$
- 115, line 3 ... and R_sⁿ⁺¹
- 120, line 2 ... Section 5.2.4 ...
- 122, Equation 5.5.3 The last term should be excluded.
- 123, line 5 The paragraph should end as "absorbed by the glass cover".
- 125, Equation 5.5.8 $R_2 = \frac{h_w + \epsilon_g \sigma (T_g^4 - T_{sky}^4) (T_g - T_{sky})}{1}$
- 126, Figure 5.5.4 Text "L = 40 mm" and "L = 10 mm" should be interchanged.
- 127, line 16 ... Table 5.5.1 ...
- 134, Figure 5.6.1 Text should be "(T₁-T₂) [°C]."